Structural Studies and Pharmacological Targeting of Protein Kinases in Obesity and Heart Disease

by

Tyler S. Beyett

A dissertation submitted in partial fulfillment
of the requirements for the degree of
Doctor of Philosophy
(Chemical Biology)
in the University of Michigan
2018

Doctoral Committee:

Professor Anna K. Mapp, Co-chair
Professor John J.G. Tesmer, Co-chair
Professor Tomasz Cierpicki
Professor Scott D. Larsen

Tyler S. Beyett

tbeyett@umich.edu

ORCID iD: 0000-0001-5509-7004

Acknowledgements

Table of Contents

List of Figures

List of Tables

List of Abbreviations

7TM: 7-transmembrane receptor
AMPK: AMP-activated protein kinase
ANS: 8-Anilino-1-naphthalenesulfonic acid
AR: adrenergic receptor
AST: active site tether
ASU: asymmetric unit
BAT: brown adipose tissue
cAMP: cyclic adenosine monophosphate
CaM: calmodulin
CCG: Center for Chemical Genomics, University of Michigan
CREB: cAMP response element-binding protein
DMSO: dimethyl sulfoxide
DSF: differential scanning fluorometry
DTT: dithiothreitol
EC_{50}: half maximal effective concentration
ESI^+: positive electrospray ionization
EM: electron microscopy
FPLC: fast protein liquid chromatography
GEF: guanine nucleotide exchange factor
GPCR: G protein-coupled receptor
GRK: GPCR kinase
IC_{50}: half maximal inhibition concentration
IκB: inhibitor of NF-κB
IKK: IκB kinase
IL-6: interleukin-6
IPTG: isopropyl β-D-1-thiogalactopyranoside
ITC: isothermal titration calorimetry
K_m: Michaelis constant
LIC: ligation-independent cloning
MALS: multiangle light scattering
MAPK: mitogen-activated protein kinase
MEF2: myocyte enhancer factor-2
MBP: maltose-binding protein
MR: molecular replacement

MS: mass spectrometry

MyBP: myelin basic protein

NF-κB: nuclear factor kappa-light-chain-enhancer of activated B cells

NLS: nuclear localization sequence

NMR: nuclear magnetic resonance

PDE: phosphodiesterase

PEG: polyethylene glycol

PH: pleckstrin homology domain

PIP_2: phosphatidylinositol 4,5-bisphosphate

PK: pharmacokinetic

PKA: protein kinas A

PKC: protein kinase C

P-loop: phosphate-binding loop

PMSF: phenylmethanesulfonyl fluoride

qPCR: real-time quantitative polymerase chain reaction

QTOF-MS/MS: quadrupole time-of-flight tandem mass spectrometry

R_g: radius of gyration

RH: regulator of G protein signaling homology domain

Rho: rhodopsin

TBK1: TRAF-associated NF-κB (TANK)-binding kinase 1

TEV: tobacco etch virus

T_m: melting/thermal denaturation temperature

TNFα: tumor necrosis factor alpha

SAR: structure-activity relationship

SAXS: Small-angle X-ray scattering

SBDD: structure-based drug design

SDS-PAGE: sodium dodecyl sulfate-polyacrylamide gel electrophoresis

SEC: size-exclusion/gel filtration chromatography

UCP-1: uncoupling protein 1 (thermogenin)

ULD: ubiquitin-like domain

V_{max}: maximum reaction velocity

WAT: white adipose tissue

WT: wild-type

Abstract

Adrenergic receptors (AR) are G protein-coupled receptors (GPCRs) responsible for regulating physiological processes including the fight-or-flight response, muscle contraction, blood flow, and energy release. Numerous protein kinases play key roles in AR signaling cascades such as GPCR kinases (GRKs) and inflammatory kinases whose aberrant activity contributes to cardiovascular disease, hypertension, type 2 diabetes, and obesity. Thus, a detailed molecular understanding of the structure, function, and regulation of these kinases will therefore facilitate the development of novel therapeutic interventions.

Obesity results in chronic inflammation of adipocytes through increased expression of inflammatory kinases, namely, IKKε and TBK1, which indirectly attenuate β_3 adrenergic receptor signaling to decrease energy expenditure and disrupt glucose homeostasis. Together, excessive activity of IKKε and TBK1 exacerbates the obese phenotype and leads to the development of type 2 diabetes. The drug amlexanox is a modest potency inhibitor of both kinases that produces weight loss and improves insulin sensitivity when administered to obese mice. Herein, I report the co-crystal structure of TBK1 in complex with amlexanox and a comprehensive profiling of the structure-activity relationships (SAR) of amlexanox analogs. Through the determination of seven co-crystal structures of TBK1 in complex with amlexanox and amlexanox analogs inhibitors, we uncovered mechanisms for improving potency, cellular efficacy, and selectivity against IKKε and TBK1. Future efforts on targeting IKKε and TBK1

should carefully consider pharmacokinetics, as we observe a stark disconnect between in vitro potency and efficacy in cells and animals. Taken together, amlexanox undoubtedly represents a pharmacophore amenable to therapeutic development whose analogs may have clinical value in the treatment of diabetes and obesity.

Heart contractility is carefully regulated through the activation of the α_1 adrenergic receptor and subsequent desensitization by GRKs. Excessive activation of α_1AR, such as during cardiac arrest, leads to abnormally high levels of intracellular Ca^{2+} and activation of calmodulin ($Ca^{2+} \cdot CaM$) which inhibits GRK5 and promotes nuclear translocation of the kinase, leading to maladaptive ventricular hypertrophy. I determined the architecture of the $Ca^{2+} \cdot CaM$–GRK5 complex through small X-ray scattering and electron microscopy, which show that $Ca^{2+} \cdot CaM$ inhibits GRK5 via bitopic bridging to two different regions of GRK5. The natural product calmodulin inhibitor malbrancheamide, which I showed binds exclusively to the C-terminal lobe of $Ca^{2+} \cdot CaM$ in a co-crystal structure, was used to probe the $Ca^{2+} \cdot CaM$–GRK5 interaction. I establish malbrancheamide as a tool for probing the regulatory effects of half the $Ca^{2+} \cdot CaM$ interaction. The bitopic nature of $Ca^{2+} \cdot CaM$ binding to GRK5 produces different modes of regulation which may therefore be exploited for therapeutic development. In particular, disrupting the C-terminal interaction may retain GRK5 at the cell membrane and block cardiac hypertrophy. Together, my work suggests that natural products may serve as useful probes for studying $Ca^{2+} \cdot CaM$ protein-protein interactions. Future efforts should consider the utility of screening natural product compound libraries to identify additional molecules that may be of use in studying maladaptive cardiac pathologies.

Chapter 1: Introduction

1.1. Adrenergic receptor signaling

1.1.1. Structure and function of G protein-coupled receptors. G protein-coupled

receptors (GPCRs) constitute the largest family of cell surface receptors in humans (>800 members) and play a critical role in the regulation of many physiological processes through the activation of the G proteins $G\alpha$ and $G\beta\gamma$ (Pierce *et al.*, 2002; Fredriksson *et al.*, 2003; Tesmer, 2016). Different GPCRs couple to one or more of the four primary classes of $G\alpha$ (Hepler and Gilman, 1992). The primary role of $G\alpha_s$ is the activation of adenylyl cyclase which generates cAMP. Elevated levels of cAMP lead to activation of protein kinase A (PKA), which phosphorylates a variety of targets. Conversely, $G\alpha_{i/o}$ inhibits cAMP production. $G\alpha_q$ activates phospholipase C which hydrolyzes phospholipids to produce phosphatidylinositol 4,5-bisphosphate (PIP$_2$) and diacyl glycerol, the later of which activates protein kinase C (PKC) and additional

Figure 1.1: Structural comparison of activated β_2AR in complex with nucleotide free $G\alpha_s$ and $G\beta\gamma$ (PDB 3SN6) and inactive β_2AR (PDB 5JQH). Nanobodies and T4 lysozyme groups are omitted for clarity. The straight arrow indicates a clash between TM6 in the inactive state and the helical domain of $G\alpha_s$. Activation of the receptor leads to a dramatic movement of TM6 (curved arrow and spheres) and lengthening of TM5, that make the core of the receptor more accessible for insertion of the α5 helix of $G\alpha_s$.

downstream signaling events including release of stored intracellular Ca^{2+}. $G\alpha_t$ (transducin), which is exclusively expressed in the retina, is activated by the GPCR rhodopsin and rapidly reduces the levels of cGMP through the activation of phosphodiesterases (PDEs) giving rise to vision. $G\beta$ and $G\gamma$ function as a constitutive heterodimer ($G\beta\gamma$) and are associated with $G\alpha$ subunits prior to activation by GPCRs. Free $G\beta\gamma$ heterodimers regulate the function of dozens of proteins including activation of some GPCR kinases (GRKs), PLCβ, and ion channels.

GPCRs are activated by a variety of ligands including small molecule hormones, peptides, and photons of light (Tesmer, 2016). Upon activation, GPCRs undergo a series of conformational changes, most notably outward movement of transmembrane helix 6 (TM6, **Figure 1.1**), that leads to the binding of and the exchange of GDP for GTP on $G\alpha$, thereby activating the α subunit of the heterotrimer and leading to dissociation of the $G\beta\gamma$ subunits. Thus, GPCRs act as transmembrane guanine nucleotide exchange factors.

1.1.2. Adrenergic receptors in cardiomyocytes and the control of contractility. The adrenergic receptor (AR) subfamily of GPCRs are activated by the catecholamine hormones epinephrine (adrenalin) and norepinephrine (noradrenaline) and regulate the fight-or-flight response, smooth muscle contraction or relaxation, and energy mobilization through coupling to different $G\alpha$ isoforms (Rockman *et al.*, 2002). α_1- and α_2AR couple to $G\alpha_q$ and $G\alpha_i$, respectively, whereas all three βARs primarily couple to G_s. Together, the combined stimulation of α- and βARs is critical for cardiovascular function which relies on the careful activation of ARs in the myocardium. Stimulation of α_1ARs by norepinephrine leads to Ca^{2+} release from the sarcoplasmic reticulum thereby triggering muscle contraction. Simultaneously, βARs, which are

2

generally less potently activated by norepinephrine, will signal for an increase in heart rate and stroke volume.

1.1.3. Adrenergic receptors in adipocytes and the control of energy homeostasis.

Adrenergic receptors also play a key role in the maintenance of proper energy balance in adipocytes (Cannon and Nedergaard, 2004). Activation of the β_3AR in brown adipocytes by norepinephrine from the hypothalamus leads to increased cAMP levels through $G\alpha_s$ and activation of PKA. PKA phosphorylates the transcription factor cAMP response element-binding protein (CREB) that leads to increased gene expression. Among the target genes is *Ucp1* which encodes uncoupling protein 1 (UCP1, also known as thermogenin). UCP1 is a proton pore that resides in the inner mitochondrial membrane and acts to dissipate the proton gradient formed by oxidative phosphorylation by the electron transport chain. Thus, the uncoupling of oxidation and phosphorylation results in greater energy expenditure through increased β-oxidation of fatty acids while generating heat as a byproduct. This process, known as non-shivering thermogenesis, is a major component of basal metabolism and the maintenance of body temperature (Cannon and Nedergaard, 2004).

1.2. Regulation of adrenergic receptor signaling cascades by kinases

1.2.1. Structure and function of kinases. Adrenergic receptor signaling relies heavily on protein kinases for the regulation and propagation of signals throughout the cell. The human kinome is composed of >500 kinases whose function is to transfer the g phosphate from ATP to substrates (Manning *et al.*, 2002). Kinases are divided into two primary groups, Ser/Thr and Tyr kinases, based on the residue(s) phosphorylated by the enzyme. A third group of kinases, termed

pseudokinases, frequently bind ATP but lack catalytic residues or are too catalytically slow for their activity to have biological significance. Despite lacking activity, pseudokinase domains often work in tandem with an active kinase domain where they play critical roles in facilitating protein-protein interactions, allostery, and substrate recruitment (Zeqiraj and van Aalten, 2010).

The canonical kinase domain is approximately 250-300 residues in length and forms two lobes (**Figure 1.2**) (Huse and Kuriyan, 2002; Taylor and Kornev, 2011). The N-terminal "small" lobe is predominantly composed of β sheets and contains a glycine-rich hairpin with the consensus sequence of GxGxxG that forms the ATP phosphate-binding loop (P-loop) and is similar to the canonical Walker A motif (**Figure 1.2 A,D**) (Saraste *et al.*, 1990; Walker *et al.*, 1982). The C-terminal "large" lobe is mostly helical and contains the so-called kinase activation loop and Asp-Phe-Gly (DFG) motif (**Figure 1.2 D**). Most kinases require phosphorylation of one or more residues in their activation loop for efficient catalysis. The DFG motif contains residues critical for the coordination of Mg^{2+}. Connecting the small and large lobes of kinases is a flexible hinge region (**Figure 1.2 B,C**) that allows for opening and closing of the kinase domain when binding ATP or substrates (Madhusudan *et al.*, 2002; Huse and Kuriyan, 2002; Taylor and Kornev, 2011; Yao *et al.*, 2017). Located in the hinge region is the so-called "gatekeeper" residue, which is often a bulky hydrophobic residue in Ser/Thr kinases but a Thr in Tyr kinases (first defined as corresponding to Thr338 in c-Src) (Taylor and Kornev, 2011; Dar and Shokat, 2011). This residue both regulates binding of ATP as well as the formation of a hydrophobic spine that stabilizes the active conformation of the kinase (Taylor and Kornev, 2011; Roskoski, 2016). Also necessary for the formation of a catalytically-competent active conformation is the positioning of the DFG motif and small lobe αC helix inward toward the ATP binding site
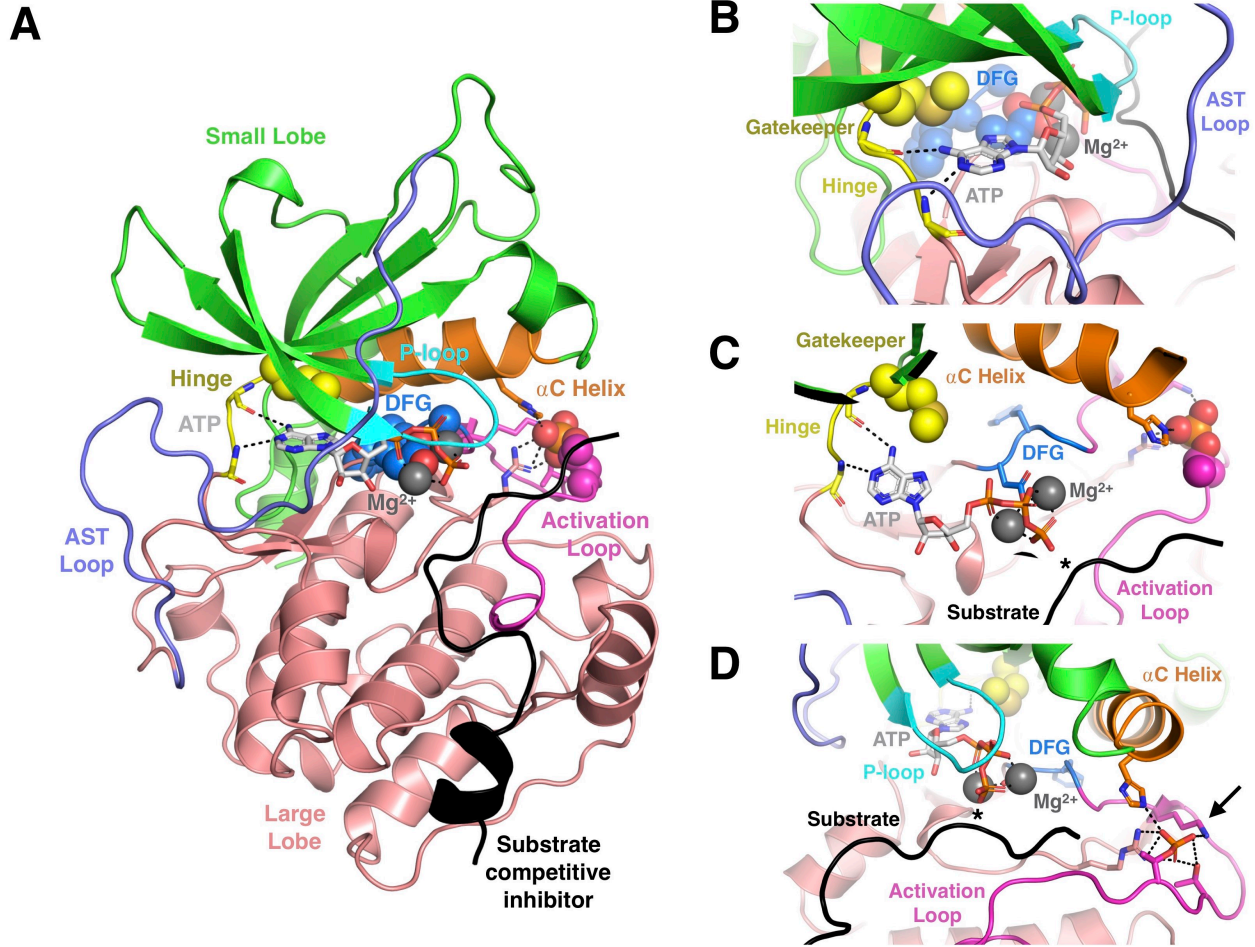
Figure 1.2: Structure of the canonical kinase domain. **A)** Protein kinase A (PDB 1ATP), the first crystal structure of a protein kinase, in complex with Mn^{2+} (labeled as the more biologically relevant Mg^{2+}), ATP, and the substrate-competitive peptide inhibitor PKI. The gatekeeper residue Met120 is shown in yellow spheres, the DFG residues in blue spheres, Mg^{2+} in dark gray, and phosphorylated Thr197 in the activation loop in magenta spheres. The active site tether (AST) loop is a conserved structural feature of AGC family kinases of which PKA is a founding member. **B)** Side view of adenine-hinge interactions. The P-loop covers the phosphate groups. The gatekeeper (yellow spheres) and AST loop must be properly aligned for efficient catalysis. **C)** Top-down view of the active site (P-loop omitted). The Asp residue of the DFG motif aids in the coordination of Mg^{2+} ions and phosphates. The substrate phosphorylation site is marked with an *, though no phosphorylatable residues exist in PKI. **D)** View of the activation loop and αC helix. Phosphorylation of Thr197 (marked with an arrow) in the activation loop establishes a network of interactions with neighboring activation loop and αC helix residues which aids in proper positioning of the DFG motif and αC helix for catalysis. The substrate phosphorylation site is marked with an *.

(Treiber and Shah, 2013; Hari *et al.*, 2013; Arencibia *et al.*, 2013) which is aided by activation loop phosphorylation (**Figure 1.2 D**). Given their importance in regulating kinase activation and catalysis, the activation loop, P-loop, and gatekeeper residue are frequent sites of mutation in disease.

1.2.2. GPCR kinases and receptor desensitization. Particularly important kinases in the regulation of adrenergic receptors are the GPCR kinases (GRKs). GRKs are Ser/Thr kinases that phosphorylate the third intracellular loop and/or C-terminus of active GPCRs to initiate primary receptor desensitization (**Figure 1.3 A**) (Homan and Tesmer, 2014; Komolov and Benovic, 2018). Arrestin proteins preferentially bind phosphorylated, activated receptors thereby sterically occluding the binding of heterotrimeric G proteins and arresting downstream signaling (Kohout and Lefkowitz, 2003; Reiter and Lefkowitz, 2006; Gurevich and Gurevich, 2006; Premont and Gainetdinov, 2007; Kang *et al.*, 2015). Arrestins also associate with clathrin-coated pits resulting in receptor internalization thereby reducing the number of receptors at the cell surface available to bind ligands (Reiter and Lefkowitz, 2006; Hanyaloglu and von Zastrow, 2008). Endocytosed receptors are either recycled back to the membrane to resume signaling or fuse with the lysosome for degradation. Interestingly, whereas arrestin-bound GPCRs are largely unable to couple to G proteins (Tsvetanova *et al.*, 2015), arrested receptors can continue signaling through alternative pathways because arrestin serves as a scaffold for the recruitment of mitogen-activated protein kinases (MAPK) and other proteins (Lefkowitz and Shenoy, 2005; Jiyuan Sun and X Lin, 2008; Irannejad and von Zastrow, 2014).

GRKs contain a kinase domain most closely related to those of the AGC (protein kinase A, G, and C) family of kinases. The domain is inserted into a regulator of G protein signaling
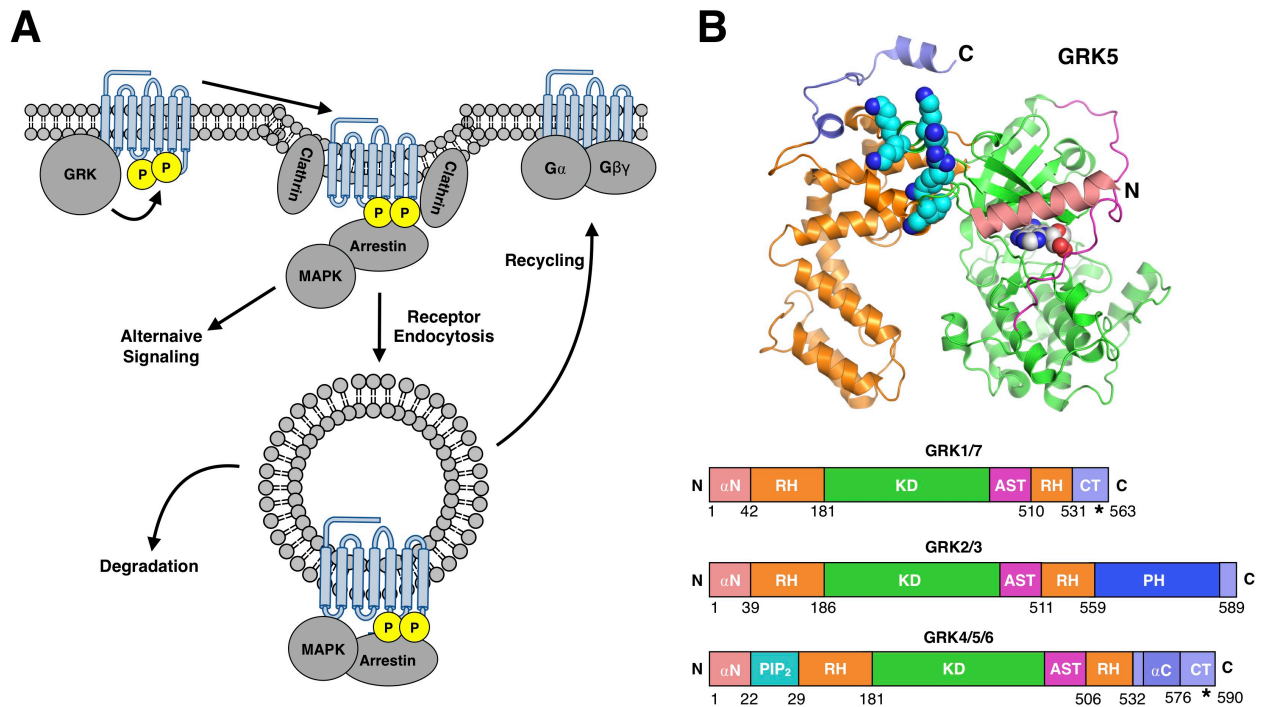
Figure 1.3: GPCR desensitization canonically involves GRKs and arrestin. **A)** Schematic of GPCR desensitization and internalization. After phosphorylation of the third intracellular loop and C-tail by GRKs, arrestin binds the GPCR and serves as a scaffold for MAPKs or interacts with clathrin to facilitate receptor endocytosis. The internalized receptor can continue to signal through MAPKs, be recycled back to the plasma membrane, or undergo degradation. **B)** Composite GRK5/6 (PDB 4WNK and 3NYN) structure and domain layout of the three subfamilies of GRKs. The αN helix, PIP$_2$ binding patch, αC helix, and C-tail (CT) are taken from GRK6 and modeled onto GRK5. *****Denotes lipidation site(s) in GRK1, 4, 6, and 7.

homology (RH) domain (**Figure 1.3 B**) (Lodowski *et al.*, 2003; Komolov and Benovic, 2018).

They are grouped into three subfamilies each with distinct C-terminal membrane localization

mechanisms to facilitate efficient receptor phosphorylation. Because there are >800 GPCRs and

only seven GRKs, GRKs are fairly promiscuous and consequently phosphorylate numerous non-

receptor substrates (Gurevich *et al.*, 2012). The visual GRK subfamily, which includes GRK1

and 7, are irreversibly prenylated in their C-terminus (Inglese *et al.*, 1992). The GRK2 subfamily

includes GRK2 and 3 and binds prenylated Gβγ subunits via their C-terminal pleckstrin

homology (PH) domain (Tesmer *et al.*, 2005). The GRK4 subfamily encompasses GRK4, 5, and

6. GRK4 and 6 are reversibly palmitoylated in their C-terminus (Stoffel *et al.*, 1994; Premont *et al.*, 1996; Loudon and Benovic, 1997; Stoffel *et al.*, 1998; Moepps *et al.*, 1999; Jiang *et al.*, 2007). All three GRK4 subfamily members contain a membrane-binding C-terminal amphipathic helix that also aids in orienting the GRK at the membrane interface (Thiyagarajan *et al.*, 2004; P Yang *et al.*, 2013). In addition to these mechanisms, GRKs interact with anionic phospholipids which promote membrane association and kinase activation (Homan, Glukhova, *et al.*, 2013). GRK4 subfamily members strongly intact with phospholipids through a basic patch at its N-terminus (residues 22-29) with preference for PIP_2 (Kunapuli *et al.*, 1994; Pitcher *et al.*, 1996). GRK5, which lacks C-terminal palmitoylation sites, relies primarily on its C-terminal amphipathic (αC) helix and interactions with phospholipids for membrane association (Thiyagarajan *et al.*, 2004; Ding *et al.*, 2014)

   1.2.3. AMP and p38 kinases in energy homeostasis. AMP-activated protein kinase (AMPK) and p38 MAPK are key regulators of lipid metabolism and thermogenesis in β_3AR-regulated energy homeostasis in brown adipose tissue (BAT) (Cannon and Nedergaard, 2004; BB Zhang *et al.*, 2009; Saltiel, 2012). AMPK is a heterotrimeric protein kinase composed of α, β, and γ monomers that monitors the intracellular AMP:ATP ratio, which is an indicator of cellular energy levels (Oakhill *et al.*, 2009; Lin and Hardie, 2018). When energy is deprived, the γ subunit cooperatively binds AMP rather than ATP, which induces an active conformation of the kinase leading to the phosphorylation of numerous targets, including enzymes involved in primary metabolism, with the net effects of reduced fatty acid synthesis and increased β-oxidation of fatty acids, glucose uptake, glycogen synthesis, and mitochondrial biogenesis (Saltiel, 2012; Hardie *et al.*, 2016). p38 MAPK is activated by increased levels of cAMP and

phosphorylates a variety of substrates, some which overlap with AMPK, to further regulate energy homeostasis (Yong *et al.*, 2009). One downstream effect of p38 MAPK activation in adipocytes is the production of interleukin-6 (IL-6), which is secreted from adipocytes and promotes glucose uptake in hepatocytes (Reilly *et al.*, 2015). Thus, p38 MAPK acts as a bridge between activation of β_3AR in fat cells and insulin response in the liver.

1.3. Pathological signaling involving kinases in adrenergic receptor cascades

1.3.1. Cardiac failure and hypertrophy mediated by GRK5. Cardiovascular disease is the leading cause of death in developed countries and includes myocardial infarction, more commonly known as a heart attack. Myocardial infarction is caused by reduction or blockage of blood supply to a portion of the myocardium leading to cell death and reduced cardiac output. In an attempt to restore cardiac output during a heart attack, the parasympathetic nervous system releases a bolus of catecholamine hormones which activate adrenergic receptors, principally αARs, which couple to G_q and elevate intracellular Ca^{2+} levels to stimulate muscle contraction (Métayé *et al.*, 2005; Salazar *et al.*, 2007; Sato *et al.*, 2015). However, excessive activation of adrenergic receptors leads to rapid, maladaptive desensitization by GRKs that attenuates cardiomyocyte contraction and prevents restoration of cardiac output. Thus, inhibition of GRKs, namely GRK2 and GRK5, represents a route to improving cardiac function during periods of cardiac stress (Waldschmidt *et al.*, 2016).

A negative feedback mechanism to counteract receptor desensitization during a heart attack has evolved (**Figure 1.4**). Increased intracellular levels of Ca^{2+} in response to αAR stimulation activates the small calcium sensing protein calmodulin (CaM). CaM is a key

9
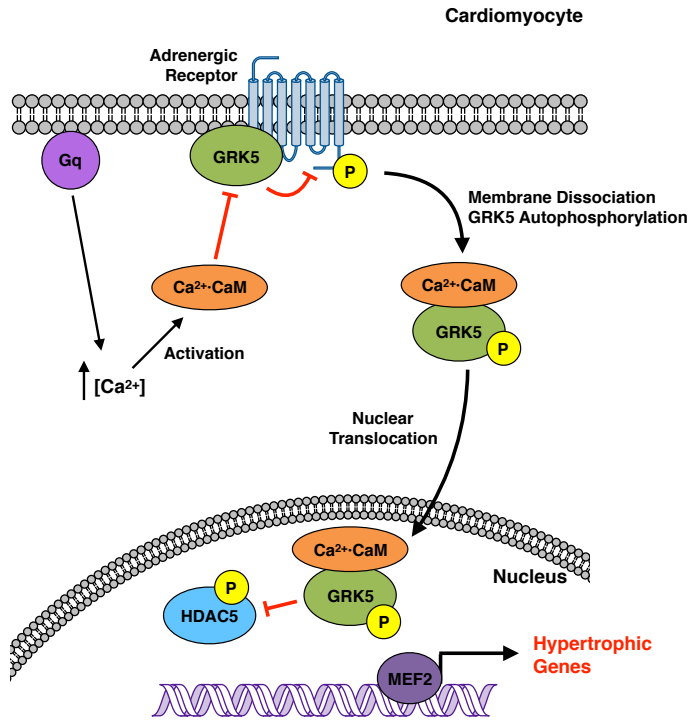
Figure 1.4: Nuclear translocation of GRK5 is Ca^{2+}·CaM-dependent. Nuclear GRK5 phosphorylates a variety of substrates including HDAC5 to derepress gene transcription and promote cardiac hypertrophy.

regulator of dozens of proteins and is highly abundant, comprising >0.1% protein by mass in humans, and highly conserved between mammals and plants (Kursula, 2014). CaM contains two pairs of calcium-binding EF-hands separated by a flexible helix. The formation of the Ca^{2+}·CaM complex leads to conformational changes that result in the formation of two hydrophobic pockets that are responsible for interactions with target proteins (Tidow and Nissen, 2013).

Ca^{2+}·CaM binds to and inhibits all GRKs, but most potently GRK5, the GRK primarily responsible for the desensitization of αARs in cardiomyocytes.

Whereas moderate inhibition of GRK5 is beneficial, excessive activation of Ca^{2+}·CaM leads to detrimental effects on cardiac function (**Figure 1.4**). The Ca^{2+}·CaM–GRK5 complex dissociates from the plasma membrane and translocates to the nucleus (Gold *et al.*, 2013), due to the presence of a strong nuclear localization sequence (NLS) in GRK5 (Johnson *et al.*, 2004), where GRK5 phosphorylates a variety of substrates including histone deacetylase 5 (HDAC5) (Martini *et al.*, 2008). Phosphorylation of HDAC5 leads to binding of 14-3-3 proteins which shuttle HDAC5 out of the nucleus resulting in derepression of numerous genes with profound

physiological effects. Most notably, decreased nuclear levels of HDAC5 in cardiomyocytes lead to the induction of genes through the transcription factor myocyte enhancer factor-2 (MEF2) (Gold *et al.*, 2013; Hullmann *et al.*, 2014) which in turn result in hypertrophic cardiomyopathy/ ventricular hypertrophy. This maladaptive process leads to enlargement or thickening of the ventricular walls and reduced cardiac output, counteracting the initial benefits of GRK inhibition and leading to an increased chance of additional episodes of cardiac arrest (Frey and Olson, 2003; Y Zhang *et al.*, 2011; Gold *et al.*, 2013). Mutation of the GRK5 NLS or introduction of Ca^{2+}-binding deficient CaM in mice prevented post-infarct cardiac hypertrophy by suppressing pathological gene activation (Johnson *et al.*, 2004). Therefore, blocking the translocation of Ca^{2+}·CaM–GRK5 to the nucleus represents a potential therapeutic strategy for suppressing ventricular hypertrophy.

   1.3.2. Obesity and diabetes mediated by TBK1 and IKKε. Obesity is a leading risk factor for the development of cardiovascular disease. Globally, more than 2 billion people are clinically overweight or obese including nearly half of adults in the United States (Swinburn *et al.*, 2011). Furthermore, obesity is the leading risk factor for the development of insulin resistance, or type 2 diabetes mellitus, which affects more than 10% of Americans with an additional 25% classified as prediabetic. A hallmark of obesity is chronic, low-grade inflammation in a variety of tissues (Mowers *et al.*, 2013). Most FDA-approved therapies for obesity focus on reducing caloric intake or altering the neurological reward system associated with eating (Saltiel, 2016). However, recognition that inflammation is involved in the progression of obesity has led to an interest in studying the link between inflammation, dysregulated body weight, and insulin resistance (Reilly and Saltiel, 2017).

Chronic inflammation as the result of a high fat diet stems from elevated levels of circulating tumor necrosis factor alpha (TNFα) which induces the expression of the kinases inhibitor of NF-κB (IκB) kinase epsilon (IKKε) and TANK-binding kinase 1 (TBK1) (Chiang *et al.*, 2009). IKKε and TBK1 are Ser/Thr kinases that share 64% sequence identity overall and 72% identity in their kinase domains. In addition to an N-terminal canonical kinase domain, both kinases possess an ubiquitin-like domain (ULD) and an extensive coiled-coiled scaffolding and dimerization domain (SDD) (**Figure 1.5 A**) (Tu *et al.*, 2013; Larabi *et al.*, 2013; Shu *et al.*, 2013). The extreme C-terminus of either kinase is critical for interactions with adaptor proteins.

Whereas IKKε and TBK1 have been most studied for their role in interferon signaling in response to viral infection (Tenoever *et al.*, 2007; Shu *et al.*, 2013), the kinases share significant homology to the canonical proinflammatory kinases IKKα and IKKβ and are also able to activate nuclear factor kappa-light-chain-enhancer of activated B cells (NF-κB) (Shimada *et al.*, 1999; Chau *et al.*, 2008). In addition to their contributions to chronic inflammation, overexpression of IKKε and TBK1 in adipocytes leads to phosphorylation and activation of phosphodiesterase 3B (PDE3B) that degrades cAMP to attenuate β3AR-mediated thermogenic signaling (**Figure 1.5 B**) (Chiang *et al.*, 2009; Mowers *et al.*, 2013). Reduced cAMP levels suppresses PKA and p38 MAPK activity, leading to reduced levels of UCP1 and IL-6, respectively. As UCP1 levels directly affect non-shivering thermogenesis, reduced levels slow basal metabolism to produce additional weight gain. Meanwhile, reduction in hepatic stimulation by IL-6 leads to dysregulated glucose metabolism and insulin response that contributes to the development of type 2 diabetes (Reilly *et al.*, 2015). Furthermore, decreased levels of cAMP suppresses AMPK and promotes direct phosphorylation of TBK1 by Unc-51-like autophagy-
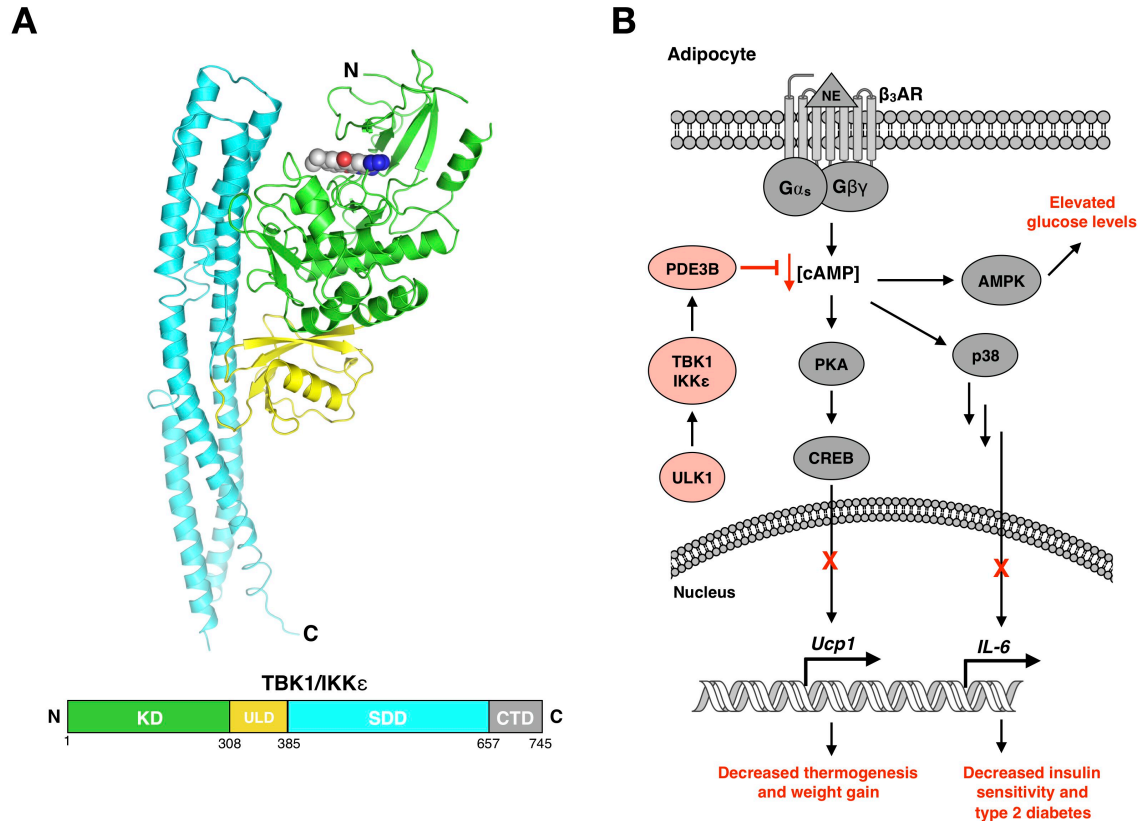
Figure 1.5: TBK1 and IKKε attenuate catecholamine-stimulated cAMP production. **A)** Structure and domain layout of TBK1 in complex with an ATP-competitive inhibitor (PDB 6BNY). The C-terminal domain (CTD) is absent in the construct crystallized. **B)** Schematic of the mechanism by which TBK1 attenuates thermogenic signaling and insulin response. TBK1 and IKKε directly phosphorylate and activate PDE3B which decreases intracellular [cAMP] thereby attenuating signaling through PKA, p38 MAPK, and AMPK while activating a feed-forward mechanism through direct phosphorylation of TBK1 by ULK1 which is normally repressed by AMPK.

activating kinase 1 (ULK1) at Ser172 in its activation loop leading to increased TBK1 kinase activity (Zhao *et al.*, 2018). Together, increased levels and activity of IKKε and TBK1 engages a feed-forward mechanism that promotes additional weight gain and further reduces insulin sensitivity.

Deletion of the IKKε gene in obese mice attenuated some of the deleterious metabolic effects of high fat feeding resulting in reduced weight gain, lowered insulin resistance, and less

chronic low-grade inflammation than wild-type controls (Chiang *et al.*, 2009). These data suggest IKKε and TBK1 may represent attractive therapeutic targets in the treatment of obesity and diabetes.

1.4. Pharmacological targeting of protein kinases

1.4.1. Types of kinase inhibitors. Given their role in the regulation of fundamental cellular processes, extensive effort has been invested in the development of therapeutics targeting kinases. In fact, kinases are fourth in the overall number of current FDA-approved therapeutics and first in approved cancer drugs over the past two decades (Vitaku *et al.*, 2014; Wu *et al.*, 2015; Jingchun Sun *et al.*, 2017; Santos *et al.*, 2017). The first kinase inhibitor, imatinib, was approved in 2001 for Bcr-Abl-driven leukemia (**Figure 1.6 A**) (Roskoski, 2015). Since then, more than 250 small molecules have progressed to human trials with nearly 40 earning FDA approval.

The vast majority of kinase inhibitors are small molecules that bind in or near the ATP binding pocket and are classified by their binding site and preferred kinase conformation (Dar and Shokat, 2011; Roskoski, 2016). Type I inhibitors are the most common and bind the DFG- and αC helix-in conformation. As both structural elements must be positioned inward toward the active site for catalysis, type I inhibitors are said to bind the active conformation of kinases. Type II inhibitors bind the less common DFG- and αC helix-out conformation (**Figure 1.6 A**) (Y Liu and Gray, 2006). Type I and II inhibitors almost always interact with the hinge and/or gatekeeper regions of the kinase and thus occupy the ATP binding site and are ATP-competitive.
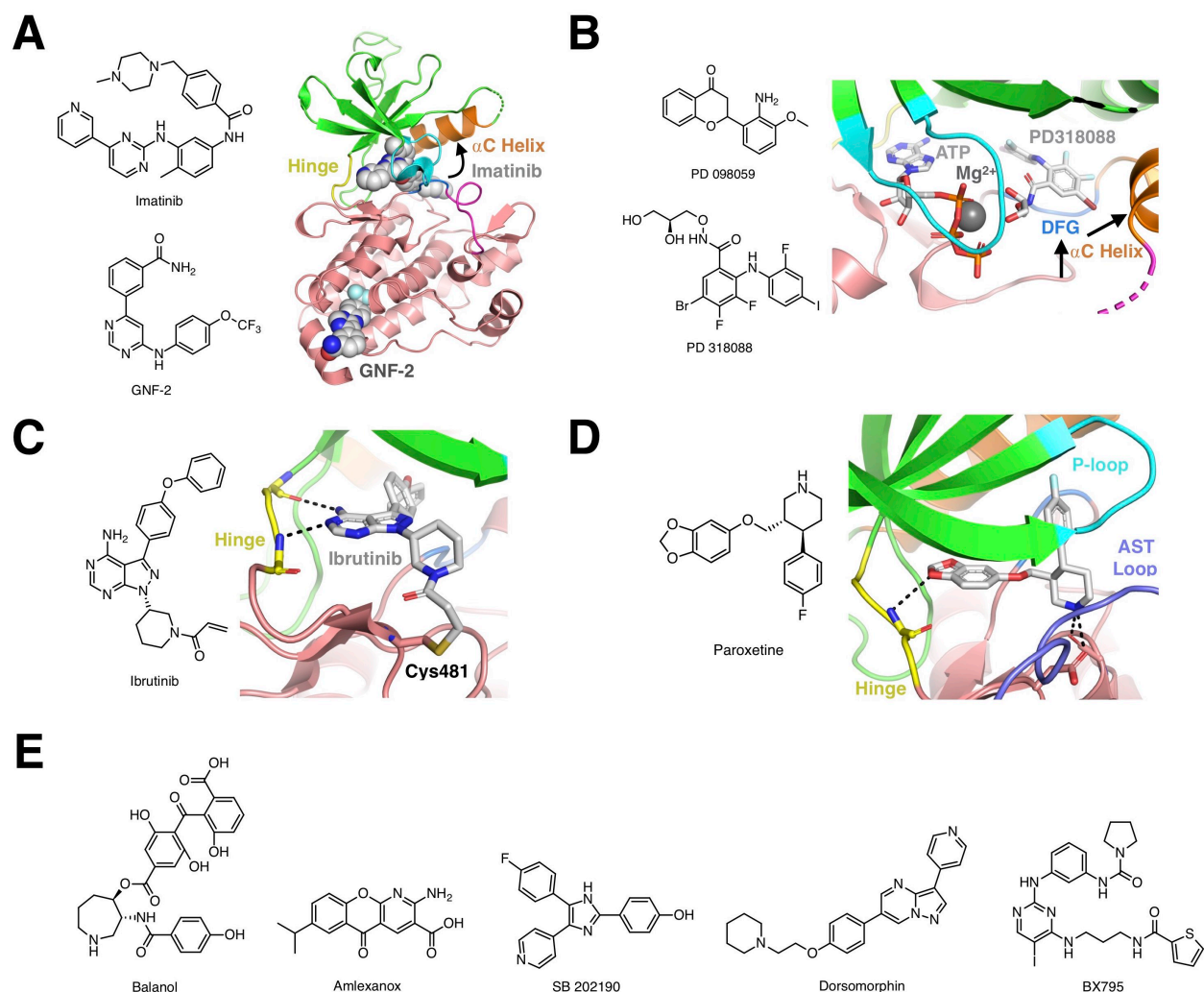
Figure 1.6: Structures of different classes of small molecule kinase inhibitors. **A)** Crystal structure of Abl kinase in complex with imatinib and GNF-2 (PDB 3K5V). Imatinib, a type II ATP-competitive inhibitor, binds along the hinge with a portion of the molecule extending toward the αC helix. This binding mode is only possible when the DFG motif and αC helix swing out (indicated by an arrow) to assume the inactive conformation. GNF-2 is an allosteric inhibitor that binds in a distant myristate-binding pocket which interferes with kinase activation. Kinase coloring is consistent with Figure 1.2 A. **B)** Crystal structure of MEK1 in complex with the allosteric inhibitor PD 318088, which occupies the same binding site as PD 098059, and ATP (PDB 1S9J). The compound forces the DFG motif and αC helix out to yield an inactive kinase conformation without affecting ATP binding. **C)** Crystal structure of Bruton's tyrosine kinase with the type VI covalent inhibitor ibrutinib (PDB 5P9J). The acrylamide group on ibrutinib forms a covalent bond with Cys481 in the large lobe of the kinase. **D)** GRK2 in complex with the type I inhibitor paroxetine (PDB 3V5W). The benzodioxole moiety forms a contact with the hinge while the fluorophenyl packs against the P-loop. **E)** Chemical structures of select kinase inhibitors.

A minority of small molecule kinase inhibitors target allosteric or regulatory regions of the protein. Researchers at Parke-Davis identified small molecules including PD 098059, that are capable of inhibiting MEK without displacing ATP, representing the first reported non-ATP-competitive kinase inhibitors (Alessi *et al.*, 1995; Dudley *et al.*, 1995). Such molecules bind adjacent to the ATP site (type III, **Figure 1.6 B**), at allosteric sites distant from the ATP site (type IV, **Figure 1.6 A**), or both (type V or bivalent) and often inhibit by preventing the kinase from assuming an active conformation, disrupting substrate binding, or altering cellular localization (Roskoski, 2016). Additional allosteric small molecule inhibitors include the type IV inhibitor GNF-2 which binds the myristate-binding pocket on Abl kinase thereby disrupting the ability of the kinase to assume an active conformation (**Figure 1.6 A**) (J Zhang *et al.*, 2010). Type VI inhibitors form covalent adducts with cysteine residues within the protein often through a Michael acceptor group, such as an acrylamide, on the inhibitor (J Zhang *et al.*, 2009). Historically avoided for potential off-target reactivity, covalent kinase inhibitors have gained popularity due to recent successes in animals and humans (Chaikuad *et al.*, 2018) Consequently, several FDA-approved covalent kinase inhibitors, such as ibrutinib, are currently on the market primarily targeting tyrosine kinases in cancer (**Figure 1.6 C**) (J Zhang *et al.*, 2009; Ferguson and Gray, 2018).

1.4.2. Inhibitors targeting GRKs. Most efforts to target GRKs have focused on their role in heart failure, hypertension, and other facets of cardiovascular disease (Homan and Tesmer, 2014a; Homan, Larimore, *et al.*, 2015; Waldschmidt *et al.*, 2016). Many pan-kinase inhibitors, such as staurosporine and sangivamycin, inhibit GRKs as well as many other kinases. The natural product balanol (**Figure 1.6 E**) is selective for AGC-family kinases, to which GRKs

belong, and is nearly 100-fold selective for GRK2 over other GRK subfamilies (Tesmer *et al.*, 2010; Thal *et al.*, 2011; Homan and Tesmer, 2014a). A family of structurally related inhibitors produced by Takeda Pharmaceuticals exhibit greater selectivity for GRK2 and appeared to be promising inhibitors for the treatment of heart failure (Thal *et al.*, 2011). However, their low bioavailability precluded further development or clinical trials.

The FDA-approved antidepressant paroxetine was identified as an inhibitor of GRK2 and bears structural similarity to several well-characterized Rho-associated coiled-coiled containing kinase (ROCK) inhibitors reported by GlaxoSmithKline (**Figure 1.6 D**) (Thal *et al.*, 2012; Homan, Wu, *et al.*, 2013, Homan *et al.,* 2014, Homan and Tesmer, 2014). Through structure-based drug design (SBDD), numerous analogs of paroxetine were synthesized drawing from prior studies on balanol and ROCK inhibitors. Highly potent and GRK2-selective inhibitors were synthesized and evaluated in mouse models of heart failure and hypertrophy (Waldschmidt *et al.*, 2016; 2017; Bouley *et al.*, 2017). Paroxetine and several related analogs increased cardiac contractility in mouse models of heart failure (Schumacher *et al.*, 2015; Bouley *et al.*, 2017). The FDA-approved anti-inflammatory drug amlexanox was also identified as a GRK inhibitor (Homan *et al.*, 2014). Unlike paroxetine, amlexanox is only 5-10-fold selective for GRK5 (**Figure 1.6 E**). Administration of amlexanox treatment markedly reduced the activation of hypertrophic genes in line with prior data indicating aberrant nuclear GRK5 activity inducing cardiac hypertrophy. This suggests differential cellular permeability or subcellular localization of amlexanox relative to paroxetine.

Despite advances in potent and selective inhibition, no inhibitors targeting GRKs or other AGC-family kinases have been approved for clinical use perhaps due to the lack of mutations

adversely affecting GRK activity and regulation. Indeed, most type I/II approved inhibitors, particularly tyrosine kinase inhibitors, target mutant forms of the enzyme with aberrant activity (Wu *et al.*, 2015; Roskoski, 2015). An alternative to ATP-competitive inhibitors are those allosterically targeting protein-protein interactions. The overexpression of the dominant negative C-terminus of GRK2 (βARKct) sequesters free Gβγ and thereby suppresses GRK2 and 3 activity, leading to improved cardiac output during heart failure (Koch *et al.*, 1995; Rockman *et al.*, 1998). Thus, small molecule inhibitors of Gβγ interactions, such as gallein, may prove useful inhibitors of GRK2 and 3 (Casey *et al.*, 2010; Kamal *et al.*, 2014).

1.4.3. Inhibitors targeting p38 MAPK, AMPK, and IκB kinases. Inhibitors targeting p38 MAPK, AMPK, and IκB kinases have been aggressively pursued given the prevalence of inflammation in many disease states including cancer and metabolic disorders (Yong *et al.*, 2009). A key challenge of kinase inhibitor development is selectivity, as the ATP binding site among kinases is highly conserved. The groundbreaking p38 MAPK inhibitor SB 202190 (**Figure 1.6 E**) proved that selective inhibition of kinases was achievable (Barancík *et al.*, 2001). The selectivity of SB 202190 stems from differences in the gatekeeper residue of MAPKs, which forms a critical contact with the inhibitor. Several structurally related p38 inhibitors have entered clinical trials but, despite excellent selectivity, failed to illicit a significant response or were associated with toxicity (Llona-Minguez and Baiget, 2013). Unlike most kinases, therapeutic targeting of AMPK has focused on the development of activators rather than inhibitors, as substrate phosphorylation is beneficial in the context of diabetes and obesity (BB Zhang *et al.*, 2009; Hardie *et al.*, 2012; Cameron and Kurumbail, 2016). AMPK-activating compounds, such as the widely prescribed drug metformin, indirectly activate AMPK by altering cellular levels of

AMP/ATP. The direct, ATP-competitive AMPK inhibitor dorsomorphin/compound C (**Figure 1.6 E**) is being explored as a therapeutic option for several cancers, though off-target inhibition of other kinases is believed to contribute to its antiproliferative effects (Jin *et al.*, 2009; X Liu *et al.*, 2014).

Inhibitors targeting the canonical IκB kinases, predominantly IKKβ, but also IKKα, which canonically activate proinflammatory NF-κB signaling, have been extensively explored by both academic and industrial groups (Llona-Minguez and Baiget, 2013). However, out of several thousand patented compounds and more than a dozen clinical trials, no IKKα or IKKβ inhibitors have earned FDA-approval, typically as a result of severe side effects stemming from immunosuppressive effects of sustained NF-κB inhibition. Thus, there has been a significant decline in IKKα or IKKβ inhibitors since the mid-2000s. However, interest in targeting the non-canonical inflammatory kinases IKKε and TBK1 have dramatically increased over the past several years. The Medical Research Council has been at the forefront of IKKε and TBK1 inhibitor development, first with the identification of the pyruvate dehydrogenase kinase 1 inhibitor BX795 (**Figure 1.6 E**) as a potent inhibitor of IKKε and TBK1 (Clark *et al.*, 2009; 2011), and the synthesis of BX795 analogs which have progressed to pre-clinical trials (Llona-Minguez and Baiget, 2013). Several pharmaceutical companies have IKKε and TBK1 inhibitors nearing clinical trials, primarily as antiproliferative agents, highlighting the promise of pharmacological targeting of these kinases (Wang *et al.*, 2012; Hayden and Ghosh, 2012; Llona-Minguez and Baiget, 2013). However, no reported compounds under investigation are for the treatment of metabolic diseases including obesity and type 2 diabetes. Thus, it is unknown whether any reported compounds are promising leads for these indications.

1.5. Summary and research goals.

Kinases play critical roles in many important physiological signaling cascades including cardiac function and basal metabolism, which are both regulated by adrenergic receptors. Herein, I aim to use structural biology to improve our understanding of the structure, function, and regulation of some of the key kinases involved in these pathways to aid in the identification and development of novel therapeutic strategies for the treatment of heart disease, obesity, and diabetes (**Figure 1.7**). First, I will describe my contributions to a structure-based drug design campaign to develop inhibitors of IKKε and TBK1 and their translation towards a clinical treatment for diet-induced obesity and type 2 diabetes. Through the determination of co-crystal structures of TBK1 in complex with amlexanox and amlexanox analogs, we uncovered mechanisms for improving potency, efficacy, and selectivity against IKKε and TBK1. I also report on the biophysical characterization of the $Ca^{2+} \cdot CaM$–GRK5 complex implicated in cardiac hypertrophy. Structural studies of the complex were aided by the application of a natural product probe that targets $Ca^{2+} \cdot CaM$ and led to the identification of druggable features of the complex that may be exploited as a therapeutic strategy to block hypertrophy in the heart. Lastly, I will describe the first method for the expression and purification of human GRK5 in bacteria along with its biochemical characterization.
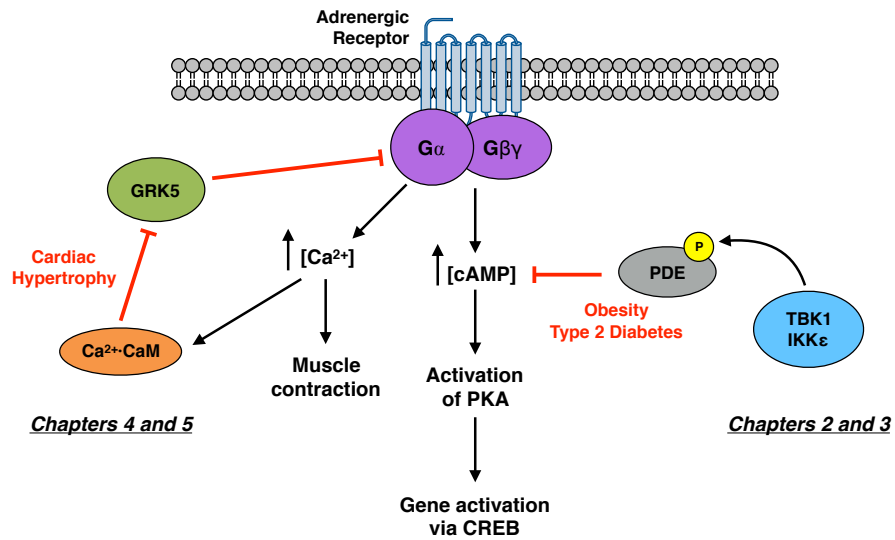
Figure 1.7: Summary of dissertation research centering on pathological regulation of adrenergic receptor signaling by kinases. Chapters 2 and 3 will describe efforts to develop therapeutics targeting TBK1 and IKKε for the treatment of metabolic disease. Chapters 4 and 5 will focus on the regulation of GRK5 by Ca^{2+}·CaM in the context of maladaptive cardiac hypertrophy.

Chapter 2: Characterization of Amlexanox and Carboxylic Acid Analogs as Inhibitors of IκB Kinases

2.1. Introduction

Obesity is the leading risk factor for the development of type 2 diabetes, and is characterized by chronic, low-grade inflammation in liver and adipose tissues stemming from overexpression of the proinflammatory kinases TBK1 and IKKε. Together, these kinases attenuate the actions of multiple hormones to produce a dysregulated metabolic state (Mowers *et al.*, 2013; Saltiel, 2016; Reilly and Saltiel, 2017).

Figure 2.1: Schematic depicting the signaling cascade underlying IKKε and TBK1-induced obesity. Amlexanox (structure inset) inhibits kinase activity to restore catecholamine-stimulated signaling cascades.

Several years ago, the FDA-approved asthma and aphthous ulcer drug amlexanox (Makino *et al.*, 1987; Bell, 2005) was identified as an inhibitor of IKKε and TBK1 (**Figure 2.1**) (Reilly *et al.*, 2013). When administered to obese mice, catecholamine-stimulated cAMP levels are restored, activating p38 MAPK and inducing expression of *Ucp1* in adipose tissue, which leads to weight loss via increased energy expenditure (Reilly *et al.*, 2013). Insulin sensitivity and regulation of glucose levels were also improved due to activation of the hepatic JAK/STAT pathway by IL-6 whose expression is regulated by cAMP levels in adipocytes (Reilly *et al.*, 2015).

Given the history of safety using amlexanox (Bell, 2005), phase I and II clinical trials in obese and diabetic patients were conducted at the University of Michigan Medical Center in which a subset of patients was identified for their positive response to amlexanox treatment (Oral *et al.*, 2017). Patients showed improvements in glycated hemoglobin (HbA1C), insulin sensitivity, and displayed a reduction in hepatic steatosis while exhibiting changes in energy expenditure gene expression similar to those previously noted in animal studies. Interestingly, in contrast to prior animal studies, no significant weight loss was observed in human patients.

Despite these promising results, the future use of amlexanox in the clinic for obesity and type 2 diabetes intervention will likely be limited by its poor aqueous solubility, moderate potency, and/or poor metabolic profile. We demonstrate *in vitro* that the carboxylic acid on amlexanox is critical for maintaining potency against TBK1 whereas its elimination significantly enhances potency toward IKKε. Replacement of the carboxylic acid with a tetrazole acid bioisostere results in improved potency toward both kinases, whereas a simple amide only displays potency toward IKKε, suggesting a potential routes for the development of IKKε-selective inhibitors. To understand how amlexanox interacts with this family of kinases and to interpret these results, the co-crystal structure of amlexanox bound to TBK1 was determined. This structure suggested a favorable interaction between the carboxylate on amlexanox and the Thr156 side chain in the active site that is critical for potent inhibition of IKKε and TBK1. Three additional amlexanox analog co-crystal structures shed light on how carboxylate analogs either improve or diminish potency. Together, these results provide the first critical insights into how to design an amlexanox analog for type 2 diabetes and obesity.

2.2. Materials and methods

   2.2.1. TBK1 protein expression and purification. Catalytically-inactive human TBK1 D135N spanning residues 1-308 ("KD") and 1-385 ("KU") (Ma *et al.*, 2012) were cloned into the bacterial expression vectors pMCSG7 (N-terminal, tobacco etch virus (TEV) protease cleavable hexahistidine tag) and pMCSG9 (N-terminal, TEV cleavable hexahistidine-maltose-binding protein (MBP)) via ligation-independent cloning (LIC). Positive clones were verified by Sanger sequencing, the DNA transformed into BL21 DE3 pLysS *Escherichia coli*. Cells were grown in terrific broth (TB) at 37 ºC to an optical density at 600 nm of 0.6-1.0, cooled to 18 ºC, and induced with 0.2 mM isopropyl β-D-1-thiogalactopyranoside (IPTG), and grown overnight. Cells were pelleted the next day, resuspended in buffer containing 20 mM HEPES pH 8.0, 200 mM NaCl, 40 mM imidazole, 1 mM DTT, 0.1 mM phenylmethanesulfonyl fluoride (PMSF), 2 µg mL^{-1} leupeptin, and 2 µg mL^{-1} lima bean trypsin protease inhibitor and briefly sonicated to lyse. Cell lysate was centrifuged for 30 m at 15,000xg and the supernatant glass filtered. Fractions of the supernatant and resuspended cell pellet were analyzed by polyacrylamide gel electrophoresis (SDS-PAGE).

   Wild-type and inactive (K38A or D135N) TBK1 spanning residues 1-308, 1-385, and 1-657 was cloned into the modified insect expression pFastBac vector pH7pFB (University of Michigan Center for Structural Biology) containing a TEV cleavable N-terminal hexahistidine tag via LIC. Positive clones were verified by Sanger sequencing, the DNA transformed into DH10Bac *E. coli*, and viral bacmid containing the gene of interest isolated by isopropanol precipitation. Recombinant baculovirus was prepared by transfecting Sf9 insect cells with purified bacmid and passaging several times to obtain virus of a higher titer. For expression, Sf9

24

or Hi5 insect cells at a density of 2×10^6 cells mL^{-1} were infected with baculovirus and harvested after 65-72 h. Cells were pelleted and flash frozen in liquid nitrogen.

TBK1 insect cell pellets were thawed and resuspended in lysis buffer containing 20 mM HEPES pH 8.0, 100 mM NaCl, 40 mM imidazole, 1 mM DTT, 0.1 mM PMSF, leupeptin, and lima bean trypsin protease inhibitor. Resuspended cells were homogenized with a Dounce homogenizer prior to brief sonication. The lysate was clarified by ultracentrifugation for 1 h at >200,000xg. The resulting supernatant was glass filtered prior to being slowly flowed through Ni-NTA resin. The resin was washed with lysis buffer and the protein eluted with lysis buffer supplemented with an additional 200 mM imidazole. Eluted TBK1 was further purified by anion exchange fast protein liquid chromatography (FPLC) using a HiTrap Q column and eluted with a NaCl gradient from 0.0-1.0 M at pH 8.0. Purified TBK1 was incubated at 4 °C overnight with 10% (w/w) TEV protease while being dialyzed against 20 mM HEPES pH 7.5, 100 mM NaCl, and 1 mM DTT to cleave the hexahistidine tag. The following day, the mixture was again passed through Ni-NTA resin to remove TEV protease and uncleaved TBK1. The cleaved TBK1 protein was dephosphorylated by incubating at room temperature for 4-6 h with λ phosphatase (New England Biolabs, Ipswich, MA) in buffer supplemented with 1 mM MnCl$_2$. The dephosphorylated protein was further purified via size-exclusion chromatography (SEC) on an analytical Superdex200 (S200) column in buffer lacking MnCl$_2$ (20 mM HEPES pH 7.5, 100 mM NaCl, and 1 mM DTT). Concentrations of ≥95% pure TBK1 by coomassie staining were determined by absorbance at 280 nm using the TBK1 molecular weight and molar extinction coefficient calculated from the primary sequence. Typical final yields were <0.25 mg L^{-1} for TBK1 KD and 0.25-1.0 mg L^{-1} cells for TBK1 1-657.

2.2.2. IKKε protein expression and purification. Catalytically-inactive human IKKε D135N spanning residues 1-309 ("KD") and 1-385 ("KU") were cloned into pMCSG7 and pMCSG9 and expressed in *E. coli* as described above for TBK1. WT and inactive (K38A or D135N) IKKε spanning residues 1-309, 1-385, 1-641, 1-643, and 1-655 were cloned into insect expression vectors and baculovirus generated also as described above for TBK1. Purification of IKKε from insect cells followed that previously described for TBK1. Briefly, cells were lysed in pH 7.5 buffer, clarified by ultracentrifugation, Ni-NTA resin, and anion exchange chromatography via a HiTrap Q column. Due to aggregation during concentration, IKKε was not purified by SEC. IKKε concentrations were determined by absorbance at 280 nm using the calculated molecular weight and molar extinction coefficient from the primary sequence and flash frozen in liquid nitrogen. Typical yields of IKKε KD and KU were 0.25-0.5 mg L^{-1} cells and 5-15 mg L^{-1} cells for the longer constructs.

2.2.3. TBK1 crystallization and structure determination. TBK1 crystal form 1 (*P6$_5$22*) was obtained with N-terminally hexahistidine-tagged TBK1 (1-657 at ~6 mg mL^{-1}) and 0.5 mM MRT67307 grown at 20 ºC via hanging drop vapor diffusion in drops containing 1 µL protein and 1 µL well solution comprised of 0.8-1.2 M Na/KPO$_4$ pH 6.4-7.0. Large (>200 µm along longest axis) hexagonal cylinders grew within 1-3 days. Crystals were harvested and briefly soaked in a cryoprotecting solution comprised of well solution supplemented with 20% glycerol and 0.5 mM inhibitor.

Crystallization conditions for crystal form 2 (*P3$_2$21*) with hexahistidine-tag cleaved TBK1 (1-657) were based on those previously reported with modification (Tu *et al.*, 2013; Larabi *et al.*, 2013). TBK1·amlexanox crystals were grown at 20 ºC via hanging drop vapor

diffusion in drops containing 1 µL of 0.1 M HEPES pH 7.5, 4% (w/v) PEG 8,000, 2 µL of

purified wild-type human TBK1 (residues 1-657 at ~3 mg mL^{-1}), and 0.2 µL amlexanox (10 mM

in DMSO) over wells containing 1 mL of 0.1 M HEPES pH 7.5, 4% (w/v) PEG 8,000, and 10%

DMSO. To obtain TBK1 crystals in complex with 224182, 224120, or 224183 analogs of

amlexanox, TBK1 was incubated with 1 mM inhibitor (from 100 mM stock in DMSO) for 1 h on

ice. Crystals were grown at 20 ºC via hanging drop vapor diffusion in drops containing 1 µL of

well solution and 1 µL of purified wild-type human TBK1 (residues 1-657 at ~3 mg mL^{-1}) over

wells containing 1 mL of 0.1 M HEPES pH 7.0-8.5 and 1-6% (w/v) PEG 8,000. Small diamonds

≤25 µm appeared within 1-2 days and grew for an additional 1-3 days to 50-100 µm in all

dimensions. Crystals were harvested and briefly soaked in a cryoprotecting solution composed of

0.1 M HEPES pH 8.5, 8% (w/v) PEG 8,000, 30% (v/v) PEG 400, and 0.5 mM inhibitor prior to

flash freezing in liquid nitrogen.

Data were collected at LS-CAT (Sector 21, Advanced Photon Source, Argonne National

Lab) under a cryostream maintained at 100 K using either MAR300 or Eiger 9M detectors. All

individual software were used as part of the SBGrid package (Morin *et al.*, 2013). Data were

processed with XDS (Kabsch, 2010) and the structure solved in Phenix (Adams *et al.*, 2010)

through molecular replacement implemented by Phaser (McCoy *et al.*, 2007) with a ligand-free

structure of TBK1 (PDB 4IM0, (Tu *et al.*, 2013) as the search model. Models were built by

alternating rounds of manual model building in Coot (Emsley *et al.*, 2010) with reciprocal space

refinement in Phenix alongside validation with MolProbity (Chen *et al.*, 2010). Ligand restraints

were generated with eLBOW in Phenix using the AM1/RM1 semi-empirical quantum-

mechanical optimization method (Moriarty *et al.*, 2009). Graphics were prepared with PyMol

(Version 2.1, Schrödinger, LLC). Coordinates and diffraction amplitudes have been deposited in the Protein Data Bank with the accession codes 5W5V, 6BNY, 6BOD, and 6BOE.

2.2.4. IC_{50} determination by radiometric kinase assay. Reactions containing 50 nM TBK1 or IKKε and 5 μM myelin basic protein (MyBP) in reaction buffer (50 mM HEPES pH 7.5, 10 mM NaCl, 10 mM $MgCl_2$, and 1 mM DTT) with varying concentrations of inhibitor were initiated with 5 μM ATP spiked with [γ-^{32}P]-ATP and allowed to proceed for 30 min at room temperature in a final volume of 20 μL. Reactions were quenched with SDS gel loading dye, run on 4-15% SDS-PAGE gels, and imaged on phosphor screens. Band intensities corresponding to phosphorylated MyBP were quantified with ImageQuant and the data analyzed in GraphPad Prism 7 using a three parameter dose-response curve model with the Hill slope constrained to −1. Statistical significance determined in GraphPad Prism via Student's two-tailed T-test using the amlexanox IC_{50} as the ideal value from a total of three experiments using protein from the same purification and a standardized ATP stock.

2.2.5. Differential scanning fluorometry thermal shift assay. Differential Scanning Fluorometry (DSF) was performed in either a ThermoFluor or HT7900 qPCR instrument. DSF via the ThermoFluor instrument was performed with 0.2 mg mL^{-1} TBK1 or IKKε (~5.8 μM for KD and KU constructs and ~2.6 μM for C-terminally truncated constructs) in assay buffer (20 mM HEPES pH 8.0, 5 mM $MgCl_2$, and 1 mM DTT), 0.1 mM 8-Anilino-1-naphthalenesulfonic acid (ANS) dye, and 200 μM ligand. DSF via qPCR instrument was performed with 0.2 mg mL^{-1} (2.6 μM) TBK1 or IKKε in assay buffer (20 mM HEPES pH 8.0, 5 mM $MgCl_2$, and 1 mM DTT), SYPRO Orange protein gel stain (5000x stock in DMSO), and 200 μM ligand. Melt curves were obtained by increasing the temperature from 25-60 ℃ at a rate of 1

ºC min^{-1} with a fluorescence reading every degree (ThermoFluor) or a rate of 2 ºC min^{-1} with continuous data acquisition (qPCR). Data were plotted in GraphPad Prism 7 with the inflection point of the sigmoidal curve representing the melting point (T_m) of the protein.

2.3. Results

2.3.1. Kinase domain purification and crystallographic studies.
Initial attempts at purifying TBK1 and IKKε focused on constructs spanning the kinase domain (KD) or kinase-ubiquitin-like domains (KU), as these constructs of TBK1 had been previously crystallized (Ma *et al.*, 2012). Expression of either wild-type (WT) or catalytically inactive (D135N or K38A) variants in *E. coli* yielded insoluble protein. Co-expression with chaperones or solubility tags did not improve soluble protein quantities (data not shown). Expression in insect cells yielded small amounts KD and KU constructs, with the best yields from the IKKε KD construct (**Figure 2.2 A**).

Purified IKKε KD was extensively screened for appropriate crystallization conditions with amlexanox and other potent pan-kinase inhibitors. Only one condition yielded crystals that diffracted to 2.7 Å with MRT67307 (**Figure 2.3 A**). However, the unit cell dimensions (56.3, 56.3, 81.9 Å, space group *P*6) is too small to accommodate the IKKε KD (**Figure 2.3 B**). Drops of protein from the same sparse-matrix screen were analyzed by SDS-PAGE and revealed a protein band at 15-20 kDa, suggesting degradation of the protein (**Figure 2.3 C**). Therefore, the crystals obtained were either a degraded form of IKKε or a minor contaminant that was not observed during prior purification steps.
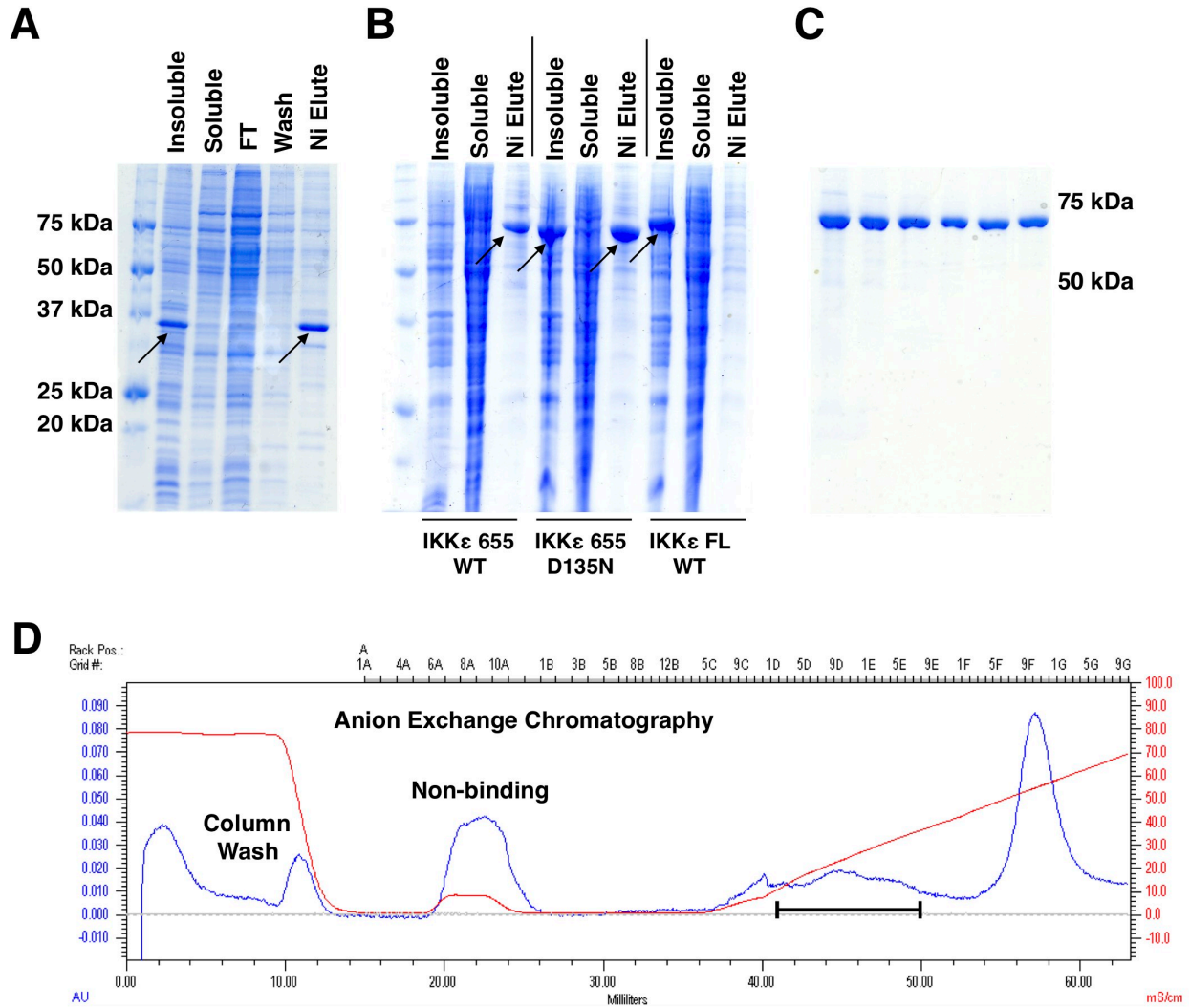
Figure 2.2: Expression and purification of IKKε. **A)** Purification of IKKε KD from insect cells. Arrows indicate insoluble and soluble kinase domain. **B)** Purification of C-terminally truncated and full-length IKKε. Only IKKε 1-655 WT and D135N yield soluble protein. **C)** IKKε 1-655 D135N elutions from Ni-NTA resin demonstrating protein purity without gel filtration. **D)** Representative anion exchange chromatogram from a HiTrap Q column. The blue trace is UV absorbance at 280 nm and the red trace is conductivity. At pH≤7.5 IKKε 1-655 elutes as a broad plateau indicated by a line under the UV trace.
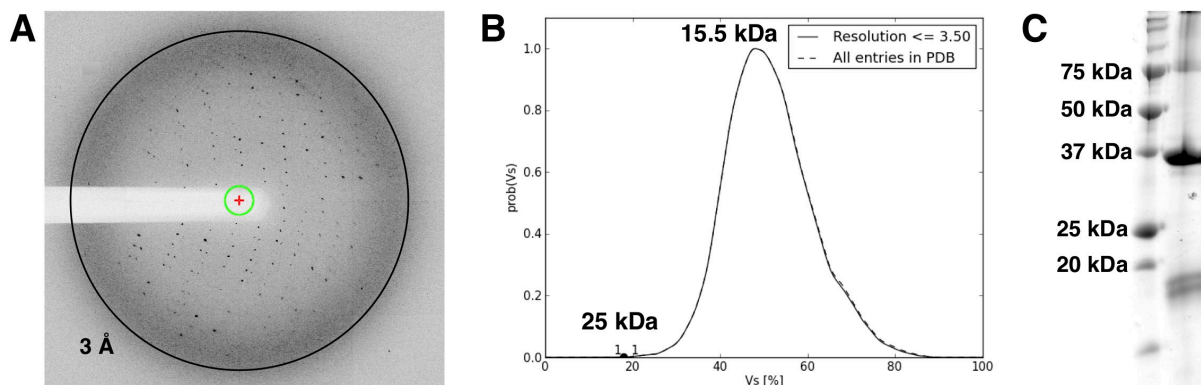
Figure 2.3: Attempted structure elucidation of IKKε KD. **A)** Diffraction pattern from crystals grown at 4 ºC in 0.1 M Bis-Tris pH 5.5 and 25% (v/v) PEG 3,350. Diffraction extends to 2.7 Å spacings. **B)** Matthews coefficient analysis plotting probability (out of total structures in the PDB) vs. solvent content (%) for the unit cell volume. Example protein masses are indicated. The mass of IKKε KD (34.5 kDa) does not lie on the distribution and cannot occupy such a small volume. **C)** SDS-PAGE analysis of protein from crystallization screen drops. IKKε KD is near 37 kDa. The bands below 20 kDa are degradation products or minor contaminants.
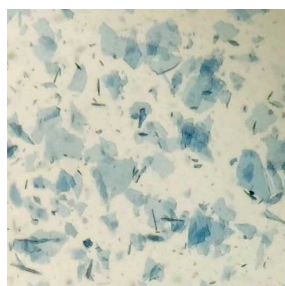
Figure 2.4: Aggregates of IKKε (residues 1-655) stained with methylene blue after concentrating >2 mg mL^{-1}.

2.3.2. Purification and crystallization of C-terminally truncated IKKε and TBK1. Given the poor expression and potential for degradation, longer constructs of TBK1 and IKKε were pursued. C-terminally truncated TBK1 (residues 1-657) had been previously crystallized and better expressed and purified from insect cells (Tu *et al.*, 2013, Larabi *et al.*, 2013). Analogous C-terminally truncated constructs of IKKε were also generated and expressed exceptionally well with typical yields >10 mg L^{-1} (**Figure 2.2 B**) but was prone to aggregation when concentrated or passed over chromatography columns. Interestingly, the aggregates formed microscopic sheets that stain with methylene blue dye similarly to protein crystals (**Figure 2.4**). However, these small plates did not diffract X-rays and attempts to image these objects via negative stain electron microscopy were unsuccessful.

31
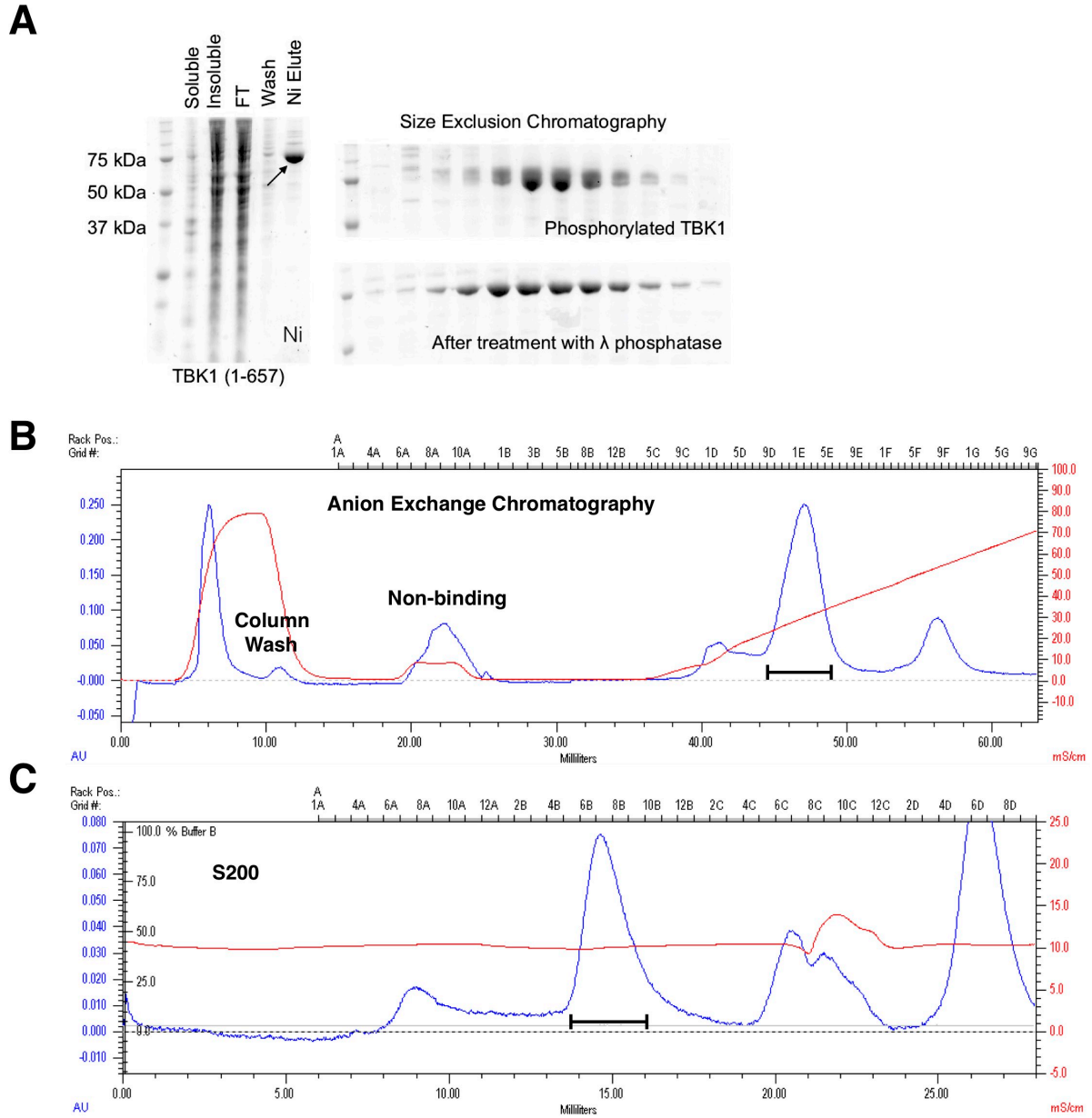
Figure 2.5: Purification of TBK1. **A)** Eluted TBK1 from Ni-NTA resin is indicated by an arrow. After S200 SEC and λ phosphatase treatment, homogeneous TBK1 was obtained. **B)** Representative anion exchange chromatogram from a HiTrap Q column. The blue trace is UV absorbance at 280 nm and the red trace is conductivity. **C)** Representative SEC chromatogram from an analytical S200 column. Eluted TBK1 is indicated by a bar under the peak.

Table 2.1: Crystallographic data collection statistics

TBK1·MRT67307	
Wavelength (Å)	1.0332
Resolution range	49.45 - 5.36 (5.45 - 5.36)*
Space group	$P\,6_5\,2\,2$
Unit cell constants (Å, °)	248.9 248.9 239.8 90 90 120
Total reflections	604583 (29982)
Unique reflections	15936 (771)
Multiplicity	37.9 (38.9)
Completeness (%)	100.0 (100.0)
Mean I/σ(I)	15.0 (1.5)
Wilson B-factor	521
R_{meas}	0.181 (3.52)
$CC_{1/2}$	0.999 (0.621)

*Statistics for the highest-resolution shell are shown in parentheses
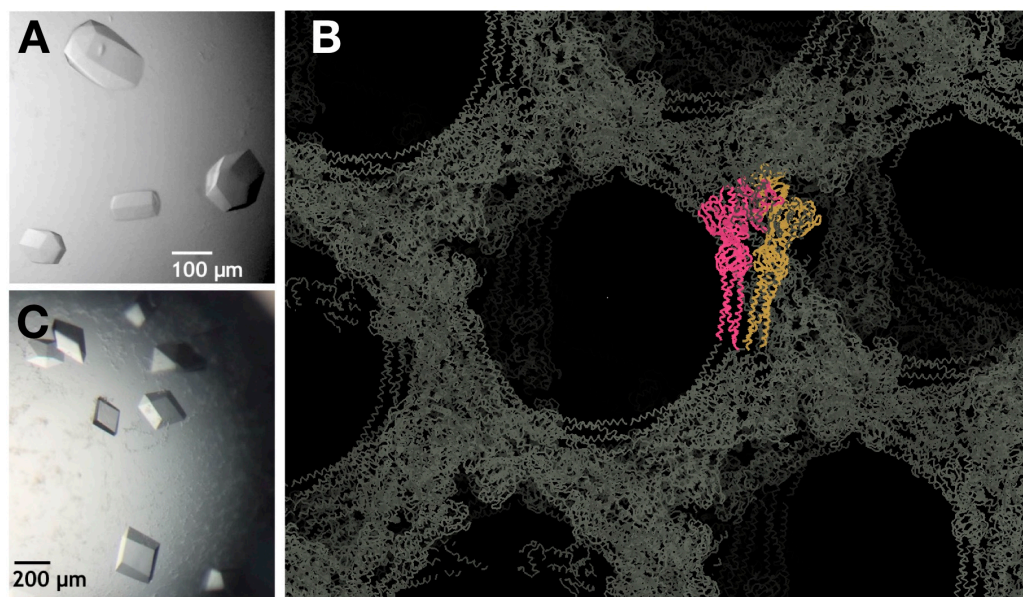
Figure 2.6: Crystallization of TBK1. **A)** Crystal form 1 ($P6_522$). Crystals grown in 1.0 M Na/ KPO$_4$ pH 6.4 with MRT67307. **B)** Crystal lattice with a solvent content of 82%. TBK1 crystallizes as a dimer in the asymmetric unit (ASU). One homodimer is colored. **C)** Crystal form 2 ($P3_221$) grown in 0.1 M HEPES pH 7.5, 5% PEG 8,000, and 10% DMSO with MRT67307.

Despite poorer expression, TBK1 was not prone to aggregation but appeared phosphorylated by SDS-PAGE due to the presence of two broad bands. Indeed, treatment with λ phosphatase resulted in a tight, single band by SDS-PAGE (**Figure 2.5**). In light of this observation, catalytically inactive TBK1 K38A was focused on, as the extent of phosphorylation was markedly decreased. Crystals of a previously reported form (form 1, $P6_522$, **Table 2.1, Figure 2.6 A**) were obtained under new conditions with the inhibitor MRT67307. However, diffraction only extended to ~5.36 Å spacings due to an solvent content of 82% (**Figure 2.6 B**).

Given the poor resolution of crystal form 1, a better diffracting crystal form was sought. Cleavage of the N-terminal hexahistidine tag yielded crystal form 2 ($P3_221$) under previously published conditions that diffracted to ~3 Å spacings with inhibitor MRT67307. However, crystals with amlexanox could not be obtained. Soaking amlexanox into TBK1 K38A·MRT67307 was unsuccessful, as the potency of MRT67307 is approximately two orders of magnitude greater than amlexanox and crystals rapidly degraded during soaking.

2.3.3. Characterization of amlexanox and co-crystal structure with TBK1. Efforts to obtain a co-crystal structure with a better-expressing, inactive form of TBK1 (K38A) were unsuccessful, but differential scanning fluorometry (DSF) with wild-type (WT) and TBK1-K38A revealed that the WT protein was significantly stabilized whereas the K38A variant was significantly destabilized by amlexanox (**Figure 2.7 A**). Using WT protein, the TBK1·amlexanox crystal structure was determined to 3.65 Å spacings (**Figure 2.7 B, Table 2.2**). The structure features strong density for amlexanox binding along the hinge of the kinase domain, mimicking the interactions made by the adenine ring of ATP. The type I binding mode is similar to that observed in the GRK1·amlexanox complex (**Figure 2.8**) (Homan *et al.*, 2014). The amine forms

Table 2.2: TBK1 crystallographic data collection and refinement statistics

Ligand	Amlexanox	224120	224182	224183
Wavelength (Å)	0.97857	0.97872	0.97857	1.03312
Resolution range	39.2 - 3.65 (3.78 - 3.65)*	44.1 - 3.34 (3.46 - 3.34)*	40.0 - 3.20 (3.31 - 3.20)*	35.4 - 3.60 (3.73 - 3.60)*
Space group	$P\,3_2\,2\,1$	$P\,3_2\,2\,1$	$P\,3_2\,2\,1$	$P\,3_2\,2\,1$
Unit cell constants (Å, °)	135.0 135.0 84.9 90 90 120	134.8 134.8 85.3 90 90 120	134.3 134.3 85.3 90 90 120	134.5 134.5 85.5 90 90 120
Total reflections	76280 (6549)	145201 (13401)	245551 (24305)	201857 (20642)
Unique reflections	10120 (923)	13238 (1305)	14970 (1463)	10626 (1055)
Multiplicity	7.5 (7.1)	11.0 (10.3)	16.4 (16.6)	19.0 (19.5)
Completeness (%)	98.0 (90.6)	99.5 (96.2)	99.6 (99.3)	99.5 (98.7)
Mean I/σ(I)	12.60 (1.09)	16.24 (1.63)	18.17 (1.60)	16.37 (1.25)
Wilson B-factor	166.0	112.4	121.9	166.0
R_{meas}	0.102 (2.23)	0.143 (1.66)	0.113 (2.14)	0.145 (1.91)
$CC_{1/2}$	0.999 (0.403)	0.999 (0.599)	1 (0.548)	1 (0.553)
Reflections used in refinement	10087 (907)	13206 (1277)	14926 (1458)	10592 (1050)
Reflections used for R_{free}	1011 (91)	1321 (127)	1495 (145)	1061 (105)
R_{work}	0.229 (0.350)	0.227 (0.352)	0.223 (0.412)	0.244 (0.428)
R_{free}	0.290 (0.371)	0.286 (0.382)	0.271 (0.454)	0.267 (0.416)
Number Non-hydrogen atoms	4887	4956	4960	4895
Protein	4865	4932	4936	4868
Ligand	22	24	24	27
RMSD bonds (Å)	0.003	0.002	0.002	0.002
RMSD angles (°)	0.77	0.50	0.41	0.41
Ramachandran favored (%)	98.6	91.0	96.3	95.6
Ramachandran allowed (%)	1.4	8.7	3.7	4.1
Ramachandran outliers (%)	0	0.3	0	0.3
Rotamer outliers (%)	0	0	0	0
Clashscore	7.0	6.9	4.2	5.1
Average B-factor	185	133	142	182
Protein	185	133	142	182
Ligand	158	97	184	187
PDB Entry	**5W5V**	**6BNY**	**6BOD**	**6BOE**

*Statistics for the highest-resolution shell are shown in parentheses
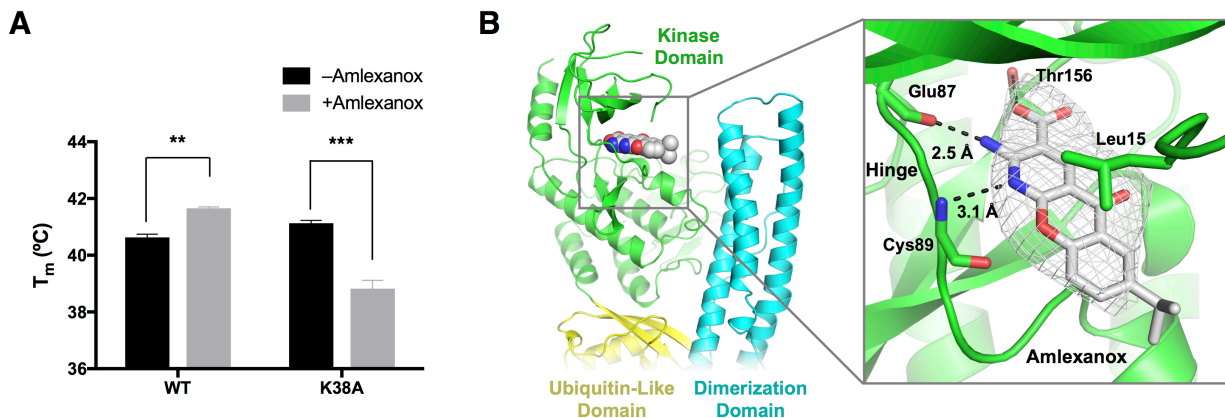
Figure 2.7: Structural analysis of the TBK1·amlexanox complex. **A)** Amlexanox (200 μM) only stabilizes the wild-type (WT) form of TBK1, as indicated by a positive shift in the melting temperature T_m (average ± SEM, n=2, two-way ANOVA with Bonferroni correction for multiple comparisons, **p≤0.01, ***p≤0.001). **B)** TBK1·amlexanox crystal structure at 3.65 Å. Amlexanox binds along the kinase hinge and forms specific interactions with the backbone of Glu87 and Cys89 and the side chain of Thr156. Mesh represents positive $|F_o|$ - $|F_c|$ density contoured at 3.0 σ.
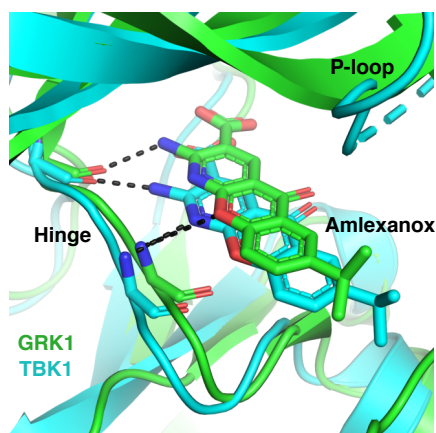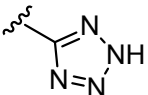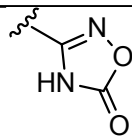
Figure 2.8: Alignment of the small lobe of the kinase domain of GRK1·amlexanox (4WBO, green) and TBK1·amlexanox (5W5V, cyan).

a hydrogen bond with the backbone carbonyl of Glu87 whereas the pyridine nitrogen interacts with the backbone nitrogen of Cys89. The side chain of Leu15 in the phosphate-binding loop (P-loop) packs against the tricyclic core of the drug. The carboxylic acid on amlexanox is 4.1 Å away from Thr156 and thus, considering the low resolution, either forms a weak hydrogen bond or favorable electrostatic interaction with the Thr156 hydroxyl. Indeed, TBK1 T156A displays a significant decrease in amlexanox potency but, interestingly, displays a slight but significant increase in potency toward IKKε T156A (**Table 2.3, Figure 2.9**). No electron density is however observed for the side chain of Lys38, which was critical for obtaining the co-crystal structure, indicating a high degree of mobility. Regardless, the Lys38 side chain would complement the negative charge of the carboxylate of amlexanox and, together with Thr156, help direct the compound into the active site.

2.3.4. Structure-activity relationships of carboxylic acid analogs of amlexanox.

Amlexanox displays an *in vitro* IC_{50} of 0.8 ± 0.1 and 5.8 ± 0.8 μM toward TBK1 and IKKε, respectively (**Table 2.4, Figure 2.9**). All analogs reported within were synthesized by Xinmin Gan, Ph.D. in the University of Michigan Vahlteich Medicinal Chemistry Core. Two analogs of amlexanox were synthesized in which the carboxylic acid was reduced to a primary alcohol (258167) or removed (232340). Reduction of the carboxyl in 258167 decreased potency 30-fold whereas elimination of the carboxylic acid in 232340 decreased potency 40-fold toward TBK1. Reduction of the carboxylate to a hydroxyl however only modestly reduced potency toward IKKε, whereas elimination of the group enhanced potency two-fold. These data show that the carboxylic acid of amlexanox plays an important role in inhibition of TBK1, but that inhibition of IKKε appears less dependent upon the carboxylate.

Table 2.3: Potency of carboxylic acid analogs against TBK1 and IKKε variants

Compound #	Amlexanox	224120	224253	224254
R	–COOH	(tetrazole)	(oxadiazolone)	(oxadiazole)
[a]Solubility (mg mL^{-1})	≥20	≥2.5	<1	<<0.5

	^{b}IC$_{50}$ (μM)			
TBK1	0.8 ± 0.1	0.1 ± 0.05	2.9 ± 1.0	>100
TBK1 T156A	10 ± 1.5***	0.06 ± 0.06	1.9 ± 1.4	n.i.
IKKε	5.8 ± 0.8	0.2 ± 0.05	1.5 ± 0.7	
IKKε M86L	1.0 ± 1.0***	0.03 ± 0.02	0.04 ± 0.03*	
IKKε T156A	1.9 ± 1.4***			

[a]Thermodynamic solubility determined by first dissolving each compound at a basic pH (dilute NaOH solution) and adjusting to pH 7.4-7.6 with buffer. [b]*In vitro* potency (IC$_{50}$, μM) towards TBK1 and IKKε variants (mean ± SEM, n=3). TBK1 M86L did not phosphorylate substrate. Statistical significance relative to WT variant determined via two-way ANOVA with Bonferroni correction for multiple comparisons (*p<0.05, ***p<0.001). n.i. no inhibition up to 200 μM.

A

B
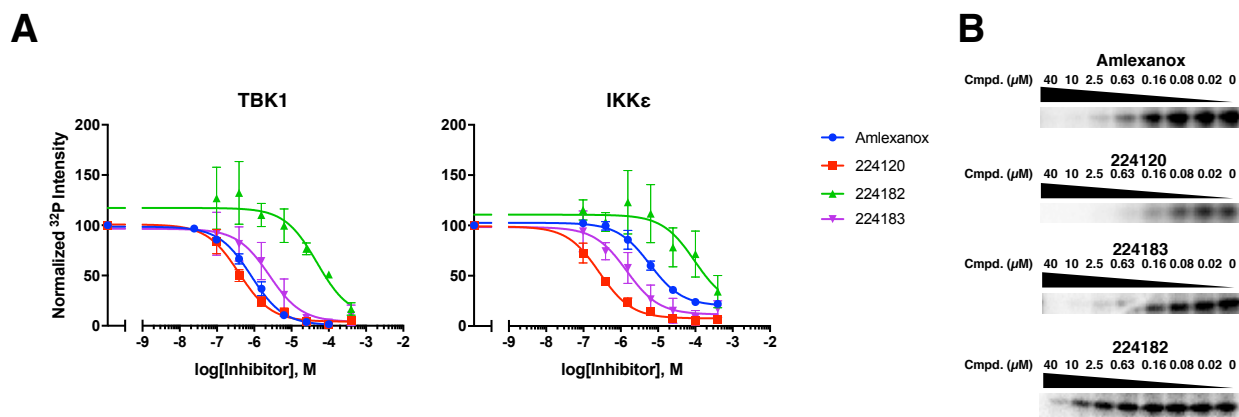
Figure 2.9: Representative dose-response curves and gels. **A)** Representative dose-response curves (Hill slope = -1) for selected analogs from Table 2.4. Data are shown as mean ± SD (N=3) and normalized to no inhibitor (100%) and background (0%). **B)** Representative SDS-PAGE gels imaged from phosphor screens. Darker bands indicate greater substrate phosphorylation in the presence of the indicated inhibitor. Inhibitor concentrations (left to right, μM): 40, 10, 2.5, 0.63, 0.16, 0.08, 0.02, 0.

Table 2.4: Potency of C-3 modified 5-Oxo-5*H*-[1]benzopyrano[2,3-*b*]pyridines
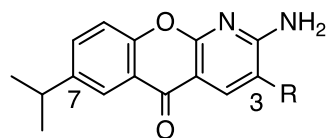
CCG #	R	^{a}cLogP	^{b}TBK1 IC$_{50}$ (μM)	^{b}IKKε IC$_{50}$ (μM)	Selectivity for IKKε
Amlexanox	−COOH	3.65	0.8 ± 0.1	5.8 ± 0.8	0.2
224182	−COOEt	4.63	55 ± 29***	65 ± 47***	0.8
258167	−CH$_2$OH	2.58	24 ± 5.7***	18 ± 8.2	1.3
224183		3.43	2.9 ± 0.5	1.6 ± 0.4	1.8
223900		3.07	>100***	17 ± 13	>5.9
223920		3.80	36 ± 14***	14 ± 8.6	2.6
223921		2.87	73 ± 26***	57 ± 23***	1.3
257636		4.02	4.5 ± 0.8**	5.4 ± 2.0	0.8
232340	−H	3.35	33 ± 18***	2.6 ± 1.1	13
224120		3.22	0.4 ± 0.05	0.2 ± 0.03***	2.0
224253		3.04	2.9 ± 1.0	1.6 ± 0.7	1.8
224254		3.39	>100***	>100***	1

^{a}Calculated partitioning coefficient assuming an unionized molecule (calculated via Marvin, ChemAxon). Larger values suggest enhanced cellular permeability. ^{b}*In vitro* potency (IC$_{50}$) towards TBK1 and IKKε (n=3, mean ± SEM). Statistical significance from amlexanox determined by two-way ANOVA with Dunnett's multiple comparison correction,*p≤0.05, **p≤0.01, ***p≤0.001.

Methyl (223900), 2-(diethylamino)ethyl (223920), and morpholine (223921) amide

derivatives were synthesized to expand the SAR around the carboxylic acid moiety. Potency of

223920 and 223921 toward TBK1 was decreased by nearly 50-fold and 90-fold, respectively.

Similar decreases in potency were observed toward IKKε. A selective loss in potency of more

than 125-fold for TBK1 was observed for the simple methyl amide analog 223900. These data

suggest that the conversion of the carboxylic acid to an amide is responsible for decreased

potency toward TBK1 rather than the steric bulk associated with the other amide derivatives.

IKKε is however more tolerant to short modifications of the carboxylic acid.

A pair of related ester analogs were next synthesized because they better mimic the parent

carboxylic acid and thus might be less detrimental to compound binding. An ester-linked 2-

(dimethylamino)ethyl analog 257636, similar to the amide-coupled amine 223920, displayed a

significant 5-fold decrease in potency but only toward TBK1. To test whether the length of the

modification could underlie the observed decrease in potency, a short ethyl ester analog (224182)

was synthesized which decreased potency by more than 65-fold toward TBK1 and 10-fold

toward IKKε, similar to the change observed for the related analog 223900.

Given the decrease in potency resulting from the elimination or derivatization of the

carboxylic acid group, a series of bioisosteres was next investigated. Analogs of amlexanox

containing tetrazole (224120), oxadiazolone (224253), or oxadiazole (224254) groups in place of

the carboxylic acid were synthesized. The tetrazole analog 224120 displayed significantly

improved potency of 400 and 200 nM against TBK1 and IKKε, respectively. Despite reduced

solubility, installation of an oxadiazolone moiety (224253) reduced potency toward TBK1 to 2.9

$\pm$ 1.0 μM and improved potency to 1.6 $\pm$ 0.7 μM toward IKKε, consistent with IKKε being able

to accept a wider variety of C-3 modifications. The oxadiazole analog 224254 was essentially inactive against both TBK1 and IKKε, likely due to its extremely poor aqueous solubility (**Table 2.3**). Given the significant enhancement in potency of the tetrazole analog, an analog bearing a tetrazole attached to the core of amlexanox through an amide linkage, 224183, was synthesized. 224183 displayed a three-fold reduction in potency toward TBK1 but significantly improved potency by three-fold toward IKKε.

2.3.5. Co-crystal structures of amlexanox C-3 derivatives. To investigate the molecular basis for the loss in potency observed for 224182 and 223900, the crystal structure of TBK1 in complex with the ethyl ester analog 224182 was determined to 3.2 Å spacings (PDB 6BOD, **Table 2.2**). Relatively weak ligand density is observed, consistent with its relatively weak 55 μM IC$_{50}$ value, but the planar density is situated along the hinge of the kinase domain analogous to the parent compound amlexanox (**Figure 2.10 A**). A shift of the P-loop and neighboring strand (residues 37-42) in the N-terminal lobe of the kinase domain is also observed, resulting in a more open active site (**Figure 2.10 B**). Compared to the TBK1·amlexanox structure, additional density is observed for residues 160-163 adjacent to the DFG motif of the kinase domain. Thus, it seems that steric clashes introduced by the addition of an ethyl group induce a twisting motion of the N-lobe of the kinase domain that leads to less favorable binding interactions with the ligand.

To investigate the binding mode of the tetrazole analog 224120, its crystal structure in complex with TBK1 was solved at 3.3 Å spacings (PDB 6BNY). The compound again binds similarly to amlexanox, forming specific interactions with the kinase hinge (**Figure 2.10 C**). Compared to the co-crystal structure with 224182, the kinase domain of TBK1 adopts a more closed conformation. Unlike amlexanox, which forms a relatively long hydrogen bond with
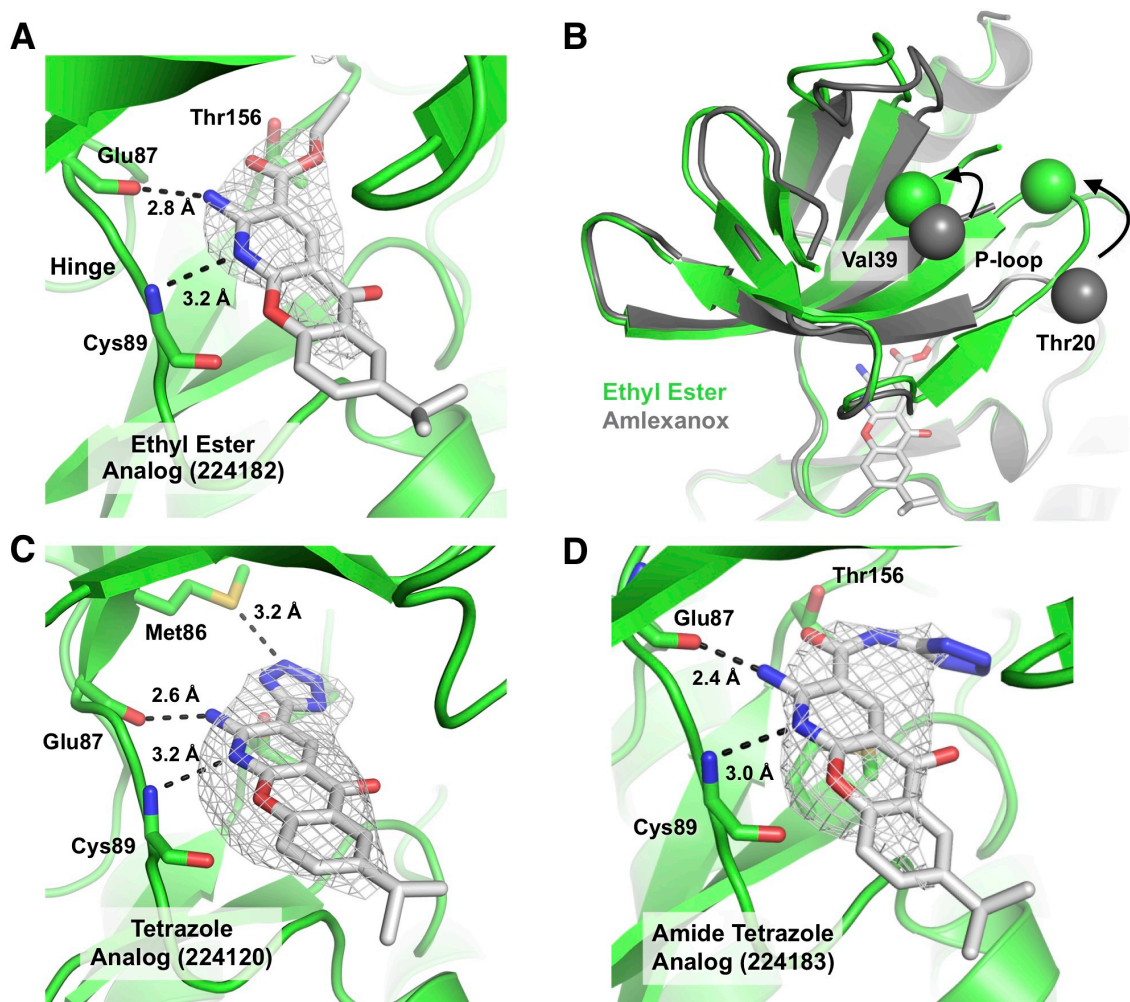
Figure 2.10: Crystallographic analysis of TBK1 in complex with carboxylic acid analogs. **A)** TBK1·224182 crystal structure at 3.2 Å. M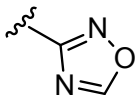esh represents positive $|F_o| - |F_c|$ omit map density contoured at 2.0 σ. **B)** Alignment of TBK1·224182 (green) and TBK1·amlexanox (gray) complexes. The rotation in the P-loop is denoted by spheres at the Cα positions of Thr20 and Val39. **C)** TBK1·224120 crystal structure at 3.3 Å with mesh representing 3.0 σ positive $|F_o| - |F_c|$ omit density. **D)** TBK1·224183 crystal structure at 3.6 Å with mesh representing 3.0 σ positive $|F_o| - |F_c|$ omit density.

Thr156, the side chain of Thr156 rotates to accommodate the tetrazole ring, which allows a 3.2 Å

hydrogen bond to form between the sulfur of the gatekeeper residue Met86 and the tetrazole

moiety. The TBK1 variant M86L, another common gatekeeper residue in Ser/Thr kinases, did

not express in insect cells but 224120 displayed an increase in potency toward IKKε M86L

(**Table 2.3**). The related compound 224253 displays increased potency toward IKKε M86L.

Additionally, 224120 and 224253 display increased potencies against both TBK1 T156A and

IKKε T156A, perhaps through the reduction of steric clashes as Thr156 is forced to rotate away

from the cyclic bioisosteres.

Because other amide derivatives were significantly less potent than amlexanox, the

molecular basis for the retained potency of 224183 was assessed via a 3.6 Å co-crystal structure

with TBK1 (PDB 6BOE). The core of the molecule again binds along the hinge (**Figure 2.10 D**).

Weak positive $|F_o|$ - $|F_c|$ omit map density is observed for the amide linker and terminal tetrazole

ring. The amide arm assumes a *cis* conformation relative to the amide bond and core of the

inhibitor, and packs between Met142 and Val23. Residues 18-21 in the P-loop are disordered,

disrupting P-loop crystal contacts observed in the other reported TBK1 structures and possibly

accounting for the decreased resolution of the diffraction data. The loss in carboxylate

interactions with Thr156 and Lys38 and disordering of the P-loop turn may partially be

compensated for by the packing of the planar tetrazole ring under the ordered portion of the P-

loop.

2.3.6. Cellular efficacy of selected carboxylic acid analogs. To determine whether

carboxylic acid modifications improve cellular efficacy, 3T3-L1 adipocytes were treated with the

highest-potency tetrazole analog 224120 and the related oxadiazolone bioisostere 224253. TBK1
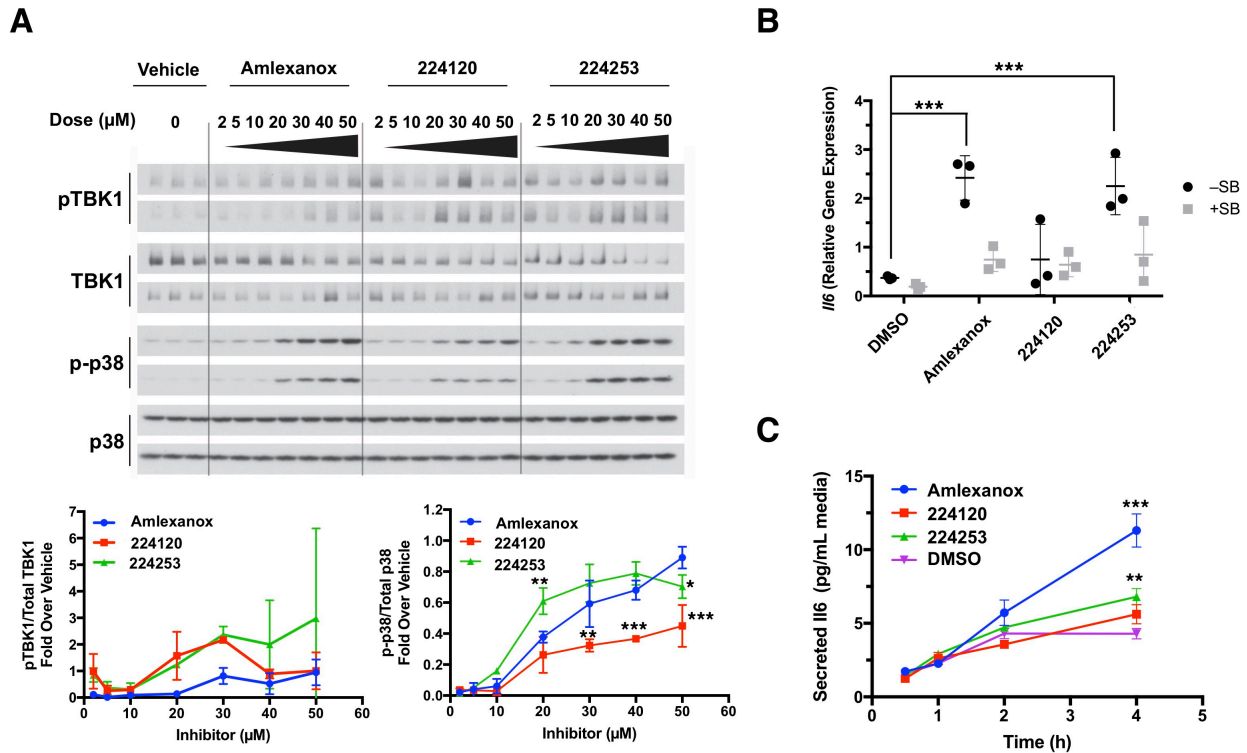
Figure 2.11: Adipocyte cellular responses upon treatment with amlexanox and selected analogs. **A)** Western blot for phosphorylation of TBK1 and p38 MAPK after incubation of 3T3-L1 adipocytes with 2-50 µM amlexanox, 224120, or 224253 for 1 h. Quantified results for pTBK1 and p-p38 are displayed below the blot (average ± SD, n=2 technical replicates, **p≤0.01, ***p≤0.001, two-way ANOVA with Dunnett's correction for multiple comparisons relative to amlexanox). **B)** Expression of *Il6* as determined by qPCR in 3T3-L1 adipocytes treated with 50 µM compound for 4 h. Expression was quantified with and without pretreatment with the p38 MAPK inhibitor SB203580 (average ± SD, n=3 biological replicates, two-way ANOVA with Dunnett's correction for multiple comparisons relative to DMSO control, ***p≤0.001). **C)** Secreted Il-6 from 3T3-L1 adipocytes treated with 50 µM compound for 4 h as determined by ELISA (average ± SD, n=2 technical replicates, two-way ANOVA with Dunnett's correction for multiple comparisons relative to DMSO control, **p≤0.01, ***p≤0.001).Experiments performed by Shannon Reilly and Louise Chang in the Saltiel lab (University of California – San Diego and University of Michigan).

mediates negative feedback regulation of AMP-activated protein kinase (AMPK) whereas IKKε,

and to a lesser extent TBK1, directly activate phosphodiesterase 3B and thereby reduce

intracellular cAMP levels to attenuate catecholamine-stimulated adrenergic receptor signaling.

Thus, inhibition of both kinases produces a unique readout consisting of increased TBK1

phosphorylation at Ser172 as a consequence of the AMPK mediated negative feedback loop

(Zhao *et al.*, 2018; Reilly *et al.*, 2013; Clark *et al.*, 2009), and phosphorylation and activation of

p38 MAPK (Reilly *et al.*, 2015), and production of IL-6 (Reilly *et al.*, 2015) downstream of

cAMP signaling. Treatment of adipocytes with 224120 or 224253 simultaneously stimulated

TBK1 and p38 phosphorylation in a dose-dependent manner (**Figure 2.11 A**). However, neither

224120 nor 224253 significantly increased pTBK1 response compared to amlexanox.

Furthermore, although 224253 more potently induces p38 phosphorylation, the maximum

response is not greater than amlexanox. Compound 224120 was worse than amlexanox at

stimulating p38 phosphorylation, likely as a result of decreased permeability, assessed by cLogP

(**Table 2.4**), and poor compound solubility in the assay medium (**Table 2.3**). Adipocytes treated

with amlexanox or 224253 display significantly increased *Il6* expression (**Figure 2.11 B**). In

agreement with previous studies, induction of *Il6* is blocked by pretreatment with the p38 MAPK

inhibitor SB203580, confirming that the observed response to 224253 is through activation of

p38 (Barancík *et al.*, 2001; Reilly *et al.*, 2015). The tetrazole analog 224120 did not induce *Il6*

gene expression. Secretion of IL-6 from treated adipocytes was also assessed by ELISA (**Figure

2.11 C**). In line with *Il6* expression, only treatment with analog 224253 resulted in a significant

increase in IL-6 secretion, though the increase was less robust than that produced by amlexanox.

2.4. Discussion

Amlexanox shows promise as a therapeutic lead for the treatment of obesity and type 2 diabetes via inhibition of kinases that are effectors of chronic low-grade inflammation in hepatic and adipose tissues. Initial characterization showed inhibition by amlexanox to be through an ATP-competitive mechanism, however the precise binding mode and molecular interactions leading to inhibition were unknown (Reilly *et al.*, 2013). The elucidation of the structure of TBK1 bound to amlexanox reveals a canonical ATP-competitive binding along the hinge of the kinase in space occupied by the adenine ring on ATP.

Figure 2.12: Chemical structures of BX795 and MRT67307.

Compared to previously reported TBK1 structures in complex with the nanomolar inhibitors BX795 and MRT67307 (Ma *et al.*, 2012; Tu *et al.*, 2013; Larabi *et al.*, 2013; Shu *et al.*, 2013), the small lobe of the kinase domain appears less ordered in complex with amlexanox, particularly residues 15-19 in the P-loop. This finding is not unexpected because amlexanox is a lower potency inhibitor and occupies only the region along the hinge, whereas the more extended BX795 and MRT67307 inhibitors (**Figures 2.12, 2.13**) also pack under the P-loop.

The interaction between the carboxylate on amlexanox and the side chain hydroxyl of Thr156 or Lys38 amine seems important for potent inhibition of TBK1, but less so in the context of IKKε where removal of the carboxylic acid moiety in 232340 instead improves potency. Reduction of the carboxylic acid to a primary alcohol in 258167 also only perturbs inhibition of TBK1. As TBK1 and IKKε are >70% identical in their kinase domains, the potency exhibited

46

Figure 2.13: Comparison of inhibitor packing under the P-loop. **A)** TBK1·MRT67307 (PDB 4IM0), **B)** TBK1·BX795 (4IM2), and **C)** TBK1·CCG-224183 (6BOE).

toward IKKε by 232340 and 223900 is surprising. One notable difference between the two kinases lies at position 90 in the hinge, which is a proline in TBK1 and a serine in IKKε. The presence of a proline in the hinge of TBK1 may restrict the relative orientation of its kinase domain lobes. Thus, the loss of the carboxylate interactions in TBK1 could result in decreased potency because the kinase is unable to optimally interact with inhibitors lacking the carboxylate. Verification of this model will await determination of atomic structures of IKKε. Taken together, disruption of the carboxylate-Thr156 interaction appears a viable strategy for improving selectivity and often potency toward IKKε.

All amide and ester modifications of the carboxylic acid significantly decreased potency toward TBK1 relative to amlexanox whereas only 223921 significantly decreased potency toward IKKε, suggesting that extensions to the carboxylic acid introduce steric clashes in TBK1 that further impede ligand binding. Indeed, the co-crystal structure of TBK1 bound to **3** reveals that esterification of amlexanox does not change the binding position of the core of the inhibitor along the kinase hinge, but the introduction of an ethyl group clearly leads to a twist in the P-loop and a more open conformation of the kinase domain. Interestingly, the amide- and ester-coupled amines 223920 and 257636, respectively, and the short methyl amide 223900, display no

significant reduction in potency toward IKKε, possibly as a result of increased hinge flexibility in this enzyme. The coupling of a 5-membered tetrazole ring through an amide linkage in 224183 improves IKKε inhibition but only exhibits a modest decrease in potency toward TBK1, whereas the 6-membered 2-morpholinoethyl analog 223921, bearing a 6-membered ring, is a poor inhibitor of both kinases. These results further suggest that there is a steric size limit for packing under the P-loop. Indeed, other potent TBK1 and IKKε inhibitors such as BX795 and MRT67307 pack 4- and 5-membered thiophene and cyclobutyl rings under the P-loop (**Figure 2.13**) (Ma *et al.*, 2012; Tu *et al.*, 2013; Larabi *et al.*, 2013).

Because TBK1 and IKKε may play different roles in chronic inflammation associated with obesity, the development of inhibitors selective for either kinase would enable pharmacological interrogation of the signaling pathways associated with each enzyme. The SAR around the carboxylic acid moiety of amlexanox reveals that IKKε is more tolerant to modifications at the C-3 position. Simple decarboxylation of amlexanox (**7**) improves selectivity toward IKKε by more than one order of magnitude. Other modifications, such as conversion of the carboxylic acid to a methyl amide (223900), also improve selectivity toward IKKε. Coupled with modifications at other positions, such as the C-7 isopropyl, these and related carboxylic acid derivatives represent possible routes to the generation of IKKε-selective inhibitors.

The lack of cellular activity observed for the tetrazole analog of amlexanox is not surprising, as tetrazole modifications have been reported to decrease cellular permeability (Lassalas *et al.*, 2016). Despite a decrease in potency toward TBK1 and solubility (**Table 2.3**), the oxadiazolone analog 224253 produces a significant cellular response, albeit less than amlexanox, perhaps due to increased cellular permeability (cLogP) of oxadiazolones (**Table 2.4**)

compared to carboxylic acids (Lassalas *et al.*, 2016). Since amlexanox and related analogs are type I kinase inhibitors with a general ATP-competitive mechanism, we cannot exclude the possibility of off-target effects, especially given the indirect nature of measuring p-TBK1, p-p38 MAPK, and IL-6. However, this particular combination of readouts has been extensively validated in the context of amlexanox (Reilly *et al.*, 2013, Reilly *et al.*, 2015, Zhao *et al.*, 2018). Given the modest nature of the C-3 modifications and expected effects in all three readouts, analogs 224120 and 224253 are likely predominantly on-target, at least in the context of cultured adipocytes. The selectivity of analogs exhibiting more promising cellular efficacy should be thoroughly assessed prior to studies *in vivo* to predict and minimize deleterious off-target effects stemming from inhibition of kinases prevalent in other cell types.

Because free carboxylic acid groups are prone to glucuronidation during phase II metabolism (Sakaguchi *et al.*, 2004), installation of less acidic bioisosteres may improve metabolic properties of amlexanox. However, in assays with cultured adipocytes metabolism is expected to be insignificant due to a lack of hepatic drug metabolizing enzymes. Difficulties solubilizing 224120 and 224253 (**Table 2.3**) prohibited testing in obese mice and highlights another PK property that may be improved through the installation of alternative bioisosteres. The co-crystal structure with the tetrazole analog 224120 will serve as a guide towards identifying alternative bioisosteres that maintain or improve potency while also improving cellular response. In particular, the related thiadiazolone and isoxazole bioisosteres are significantly more cell permeable and are targets for future exploration (Vitaku *et al.*, 2014; Lassalas *et al.*, 2016).

The co-crystal structures and *in vitro* SAR analysis presented herein will enable future development of TBK1 and IKKε inhibitors based on the amlexanox pharmacophore. Significant improvements in potency have been achieved through the installation of acid bioisosteres, whereas other carboxylic acid modifications suggest possible routes for improving inhibitor selectivity for IKKε. Despite improved potency, improving cellular efficacy remains a challenge because modification of the carboxylic acid may alter PK properties that hamper drug distribution and cellular permeability.

Chapter 3: Analysis of A Ring and Truncated Pharmacophore Analogs of Amlexanox as Inhibitors of IκB Kinases

3.1. Introduction

Elucidation of the TBK1·amlexanox structure revealed the amino pyridine moiety on amlexanox binds the kinase hinge and a critical interaction between the C-3 carboxylate and the sidechain of Thr156 in TBK1. Inhibition of IKKε is not dependent upon this carboxylate interaction and modification of the corresponding position is largely tolerated. Despite improvements in potency upon the installation of a tetrazole at the C-3 position, significant enhancements to efficacy and selectivity remain elusive. To remedy these concerns, we sought to modify additional positions on the amlexanox pharmacophore to improve potency, solubility, and efficacy.

Guided by prior structures and SAR, amlexanox analogs bearing conservative modifications at the C-7 position alongside a small set of C-6 and C-8 derivatives that may stabilize the P-loop or interact with the kinase hinge, respectively, were evaluated for their ability to inhibit either kinase. A large series of cyclic C-7 modifications were also examined due to their synthetic accessibility along with crystallographic data showing space to accommodate bulkier modifications. Drawing from previous analogs, bioisostere derivatives of the C-3 carboxylic acid were combined with C-7 modifications to assess the effect of dual modification of the pharmacophore. Lastly, in pursuit of a novel pharmacophore, a truncated form of

amlexanox lacking the solvent exposed A ring was prepared and a small subset of analogs tested to demonstrate future utility of this pharmacophore. Taken together, this extensive series of analogs reveals mechanisms for the selective and potent inhibition of IKKε which has recently been shown to play a distinct role in obesity and diabetes.

3.2. Materials and methods

3.2.1. Protein expression and purification. WT TBK1 (1-657) and IKKε (1-655) for assays and crystallography were purified as described previously in sections *2.2.1.* and *2.2.2.*

3.2.2. IC$_{50}$ determination by radiometric kinase assay. Single-dose inhibition assays were performed for TBK1 and IKKε with either 1 or 5 µM inhibitor, respectively. Percent inhibition was determined by normalizing substrate phosphorylation in the presence of inhibitor to a no inhibitor (0% inhibition) or background (100% inhibition) control. Dose-response assays were carried out as described previously in *2.2.4*. Statistical significance from amlexanox was determined by a Student's two-tailed t-test from three independent experiments.

3.2.3. Crystallization. Crystallization conditions were based off those previously reported with modifications (Tu *et al.*, 2013; Larabi *et al.*, 2013). TBK1 crystals were grown at 20 ℃ via hanging drop vapor diffusion in drops containing 1 µL of 100 mM HEPES pH 7.5, 4% (w/v) PEG 8,000, 2 µL of purified human TBK1 (residues 1-657 at ~3 mg mL^{-1}), and 0.2 µL inhibitor (10 mM in DMSO) over wells containing 1 mL of 100 mM HEPES pH 7.5, 4% (w/v) PEG 8,000, and 10% DMSO. Small diamonds appeared within 1-2 d and grew for an additional 1-2 d. Better diffracting and larger crystals were obtained through microseeding. Crystals of form 2 (*P*3$_2$21) were harvested and briefly soaked in a cryoprotecting solution containing 100 mM

HEPES pH 8.5, 8% (w/v) PEG 8,000, 30% (v/v) PEG 400, and 0.5 mM inhibitor prior to flash freezing in liquid nitrogen. Data were collected and processed as described in *2.2.3*. Coordinates and diffraction amplitudes have been deposited in the Protein Data Bank with the accession codes 6CQ0, 6CQ4, and 6CQ5.

3.2.4. Virtual docking. Docking was performed with PyRx (Dallakyan and Olson, 2015) using the Autodock Vina (Trott and Olson, 2010) algorithm. All docking was rigid body for the protein and side chains and flexible for the ligand. Docking grid space encompassed the entire active site.

3.3. Results

3.3.1. Structure-activity relationships of acyclic A ring analogs of amlexanox. All analogs reported within were synthesized by Xinmin Gan in the University of Michigan Vahlteich Medicinal Chemistry Core. Potency of simple amlexanox analogs was assessed *in vitro* by radiometric kinase assays (**Table 3.1**). Analogs 259012, 262485, 258073, 258702 bearing a 2-propenyl substituent at the C-7 or C-8 positions generally show significantly reduced potency toward TBK1 while significantly improving potency toward IKKε when located at the C-7 position. The addition of a methylene spacer(s) (258961 and 258762) had no significant effect on potency. The introduction of an alkyne spacer (258759) markedly reduced potency with the data likely compromised due to poor solubility in the assay medium. To improve the solubility of amlexanox, the isopropyl group was replaced with a dimethyl amino moiety in 232482 which improved potency two- and three-fold toward TBK1 and IKKε, respectively.

Moving the isopropyl group to the C-6 position in 262826, in an attempt to stabilize the

53

P-loop by packing against Leu15 and Gly16, reduced potency toward TBK1 while displaying no detrimental effect on inhibition of IKKε. Shifting the isopropyl to the C-8 position in 259043 significantly improved potency toward TBK1. The introduction of fluorine at the C-8 position in 262501 enhanced potency toward either kinase relative to des-fluoro congener amlexanox, and slightly improved potency of the C-7 2-propenyl analog 262485 for TBK1 compared to the non-fluorinated 258702. Installation of a nitrogen in place of carbon at the 8-position of amlexanox in 258101 enhanced potency toward both kinases. In contrast, making the same replacement for the C-7 2-propenyl congener 258702 to give 258073 negated the potency enhancing influence of the C-7 2-propenyl substituent toward IKKε.

Analogs bearing more extensive modifications at the C-7 and C-8 positions which may dramatically affect potency were synthesized and assessed as well, generally at ~40 µM near the amlexanox IC$_{50}$ toward TBK1 and IKKε, respectively (Fig. 3.1). Most of these amlexanox analogs displayed decreased potency relative to amlexanox. Selected analogs displaying
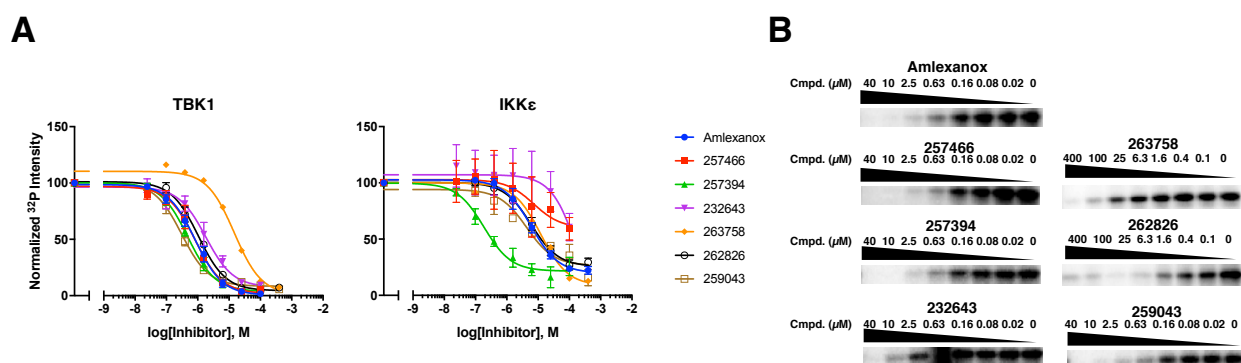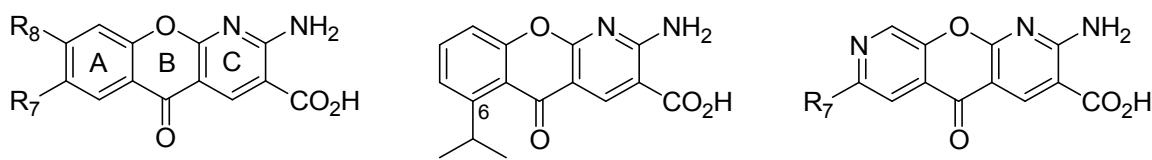
Figure 3.1: Representative dose-response curves and gels. **A)** Representative dose-response curves (Hill slope = -1) for selected analogs from Appendix 3.1. Data are presented as mean ± SD (N=3) and normalized to no inhibitor (100%) and background (0%). **B)** Representative SDS-PAGE gels imaged from phosphor screens. Darker bands indicate greater substrate phosphorylation in the presence of the indicated inhibitor. Inhibitor concentrations (left to right, µM): 40, 10, 2.5, 0.63, 0.16, 0.08, 0.02, and 0 except for 263758 and 262826 which are (left to right, µM): 400, 100, 25, 6.3, 1.6, 0.4, 0.1, and 0.

Table 3.1: Potency of Synthesized 5-Oxo-5*H*-[1]benzopyrano[2,3-*b*]pyridines

CCG#	R$_7$	R$_8$	Aq. sol. (μM)[a]	[b]Single Concentration % Inhibition [c](IC$_{50}$, μM)			
				TBK1	IC$_{50}$ Fold Change	IKKε	IC$_{50}$ Fold Change
Amlexanox	*i*-Pr	H	172	50 ± 1.3 (0.85 ± 0.14)		29 ± 7.4 (5.1 ± 1.6)	
258702	CH$_2$=C(CH$_3$)-	H	259	(1.3 ± 0.1*)	0.7	(1.3 ± 0.5**)	3.9
259043	H	*i*-Pr	19	(0.30 ± 0.03**)	2.8	(4.7 ± 2.3)	1.1
259012	H	CH$_2$=C(CH$_3$)-	n.d.	(2.3 ± 0.1**)	0.4	(7.2 ± 2.0)	0.7
262826	C-6 Amlex		229	(1.1 ± 0.02**)	0.8	(6.0 ± 0.5)	0.9
262501	*i*-Pr	F	14	(0.40 ± 0.08)	2.1	(5.4 ± 0.7)	0.9
262485	CH$_2$=C(CH$_3$)-	F	n.d.	(0.79 ± 0.07)	1.1	(1.7 ± 0.3*)	3.0
258101	*i*-Pr	8-aza	78	(0.57 ± 0.02**)	1.5	(3.1 ± 1.1)	1.6
258073	CH$_2$=C(CH$_3$)-	8-aza	373	(2.0 ± 0.3*)	0.4	(5.3 ± 0.5)	1.0
232482	Me$_2$N	H	n.d.	(0.40 ± 0.09*)	2.1	(1.6 ± 0.5)	3.2
232241	Me$_2$N(CH$_2$)$_3$-	H	n.d.	35 ± 2.2		21 ± 1.8	
232240	Me$_2$NCH$_2$C≡C-	H	n.d.	20 ± 3.4		17 ± 2.0	
258961	*i*-Bu	H	179	(0.55 ± 0.08)	1.5	(4.9 ± 2.0)	1.0
258762	*i*-pentyl	H	119	(0.83 ± 0.08)	1.0	(3.4 ± 0.4)	1.5
258759	(CH$_3$)$_2$CHC≡C-	H	n.d.	(12 ± 1*)	0.1	(20 ± 9)	0.3
262706	*i*-pentyl	F	n.d.	32 ± 0.7		-5.7 ± 4.7	
258727	*t*-BuCH$_2$CH$_2$	H	n.d.	14 ± 4.8		0.6 ± 11	
258726	*t*-BuCH=CH-	H	n.d.	8.7 ± 4.2		-3.1 ± 3.2	

[a]Thermodynamic solubility determined by Analiza Inc, Cleveland, OH 44114. [b]TBK1, (1 μM); IKKε (5 μM) (n=3, mean ± SEM). [c] Concentration for 50% inhibition in radiometric kinase assays using purified protein. Reported as IC$_{50}$ (μM) ± SEM (n=3). Significance relative to amlexanox determined by a two-tailed Student's T-test (*p<0.05, **p<0.01). n.d. = not determined

equivalent or improved potency were further tested in dose-response assays. Introduction of conformational restriction in amlexanox to give cyclopropyl analog 223901 resulted in reduced potency toward both kinases. A decrease in inhibition was observed as the ring size at the C-7 position was increased from c-Bu to c-heptyl (232960, 224081, 232643, and 257042) with IKKε inhibition the most adversely affected. However, unsaturation of the cyclohexyl ring in 232780 improved inhibition of IKKε while decreasing TBK1 inhibition, consistent with prior observation that unsaturated 2-propenyl substituents preferentially improve IKKε inhibition. When the C-7 cyclohexyl and cyclohex-2-enyl modifications are combined with fluorination at the 8 position or appended to the 8-aza scaffold a large decrease in inhibition is observed similarly to the decrease observed for 262501 and 258101. The phenyl analog 232925 displayed a similar trend in inhibition of TBK1 and IKKε.
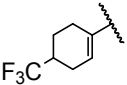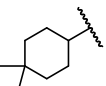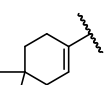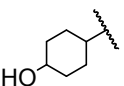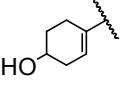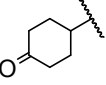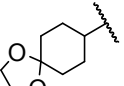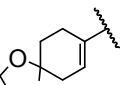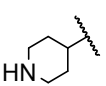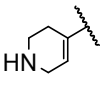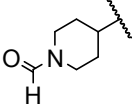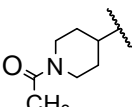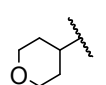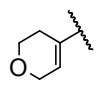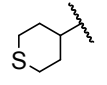
3.3.2. Structure-activity relationships of cyclic A ring analogs of amlexanox. Based off preliminary cellular results with 232643, we choose to focus on C-7 c-hexyl analogs (**Table 3.2**). Fluoro, methyl, or trifluoromethyl modifications were made at the para position (257089, 257082, 232900, 257134, 257133, 257783, and 257685). These modifications decreased compound solubility and reduced inhibition. Hydroxylation of the para position in 257273 also reduced potency, but the introduction of a double bond in 257226 improved IKKε inhibition to that of amlexanox while further decreasing TBK1 inhibition. Installation of a cyclohexanonyl ring at the C-7 position in 257635 significantly improved potency toward TBK1. Conversion to a ketal in 257366 significantly improved potency toward both kinases while the introduction of a double bond in the ring only significantly improved potency toward IKKε.

Next, nitrogen, oxygen, and sulfur containing heterocycles were examined. The

installation of a piperidinyl group at the C-7 position in 232606 and 232781 reduced inhibition

Table 3.2: Potency of C-7, C-8 cyclic and alkcyclic 5-Oxo-5H-[1]benzopyrano[2,3-b]pyridines

CCG#	R$_7$	R$_8$	Aq. sol. (µM)[a]	[b]Single Concentration % Inhibition [c](IC$_{50}$, µM)			
				TBK1	IC$_{50}$ Fold Change	IKKε	IC$_{50}$ Fold Change
Amlexanox	i-Pr	H	172	50 ± 1.3 (0.85 ± 0.14)		29 ± 7.4 (5.1 ± 1.6)	
223901	c-Pr	H	148	(2.3 ± 0.1**)	0.4	(10.6 ± 0.4**)	0.5
232960	c-Bu	H	n.d.	44 ± 3.7 (4.6 ± 3.6)	0.2	25 ± 3.4 (3.1± 0.7*)	1.6
224081	c-Pentyl	H	n.d.	67 ± 4.1 (1.8 ± 0.3*)	0.5	9.2 ± 1.9 (6.3 ± 1.0)	0.8
232643	c-Hexyl	H	94	34 ± 1.6 (1.9 ± 0.6)	0.5	9.0 ± 3.1 (>100)	
232780	(cyclohexenyl)	H	n.d.	44 ± 0.2 (1.7 ± 0.5)	0.5	41 ± 4.9 (5.4 ± 1.5)	0.9
257042	c-Heptyl	H	n.d.	32 ± 8.5		9.2 ± 4.1	
262457	H	c-Hexyl	n.d.	11 ± 9.6		8.2 ± 6.3	
259142	H	(cyclohexenyl)	n.d.	15 ± 3.7		15 ± 4.7	
232925	(phenyl)	H	n.d.	34 ± 2.9		33 ± 6.4	
257089	(difluorocyclohexyl)	H	n.d.	14 ± 3.8		11 ± 2.1	
257082	(difluorocyclohexenyl)	H	n.d.	27 ± 3.8		19 ± 5.6	
232900	(methylcyclohexyl)	H	n.d.	19 ± 5.6		3.2 ± 2.9	
257134	(trifluoromethylcyclohexyl)	H	n.d.	33 ± 8.0		11 ± 2.3	

57

ID	Structure					
257133		H	n.d.	4.0 ± 4.0		0.4 ± 0.4	
257783		H	n.d.	15 ± 6.5		-0.7 ± 7.5	
257685		H	n.d.	38 ± 4.5		22 ± 2.4	
257273		H	n.d.	37 ± 2.8		12 ± 2.2	
257226		H	n.d.	27 ± 2.8		26 ± 3.6	
257635		H	< 1	52 ± 6.2 (0.45 ± 0.07*)	1.9	27 ± 4.9 (1.5 ± 1.3)	3.4
257366		H	n.d.	63 ± 1.1 (0.44 ± 0.05*)	1.9	30 ± 8.1 (3.2 ± 0.03**)	1.6
257344		H	n.d.	54 ± 2.4 (0.75 ± 0.06)	1.1	63 ± 4.6 (2.1 ± 0.8*)	2.4
232606		H	n.d.	12 ± 8.7		7.9 ± 8.6	
232781		H	n.d.	22 ± 3.4		23 ± 2.7	
232867		H	n.d.	68 ± 1.1 (0.49 ± 0.05*)	1.7	34 ± 8.4 (5.2 ± 2.9)	1.0
232681		H	121	66 ± 1.3 (0.27 ± 0.03**)	3.1	26 ± 7.5 (1.9 ± 2.6)	2.7
232607		H	n.d.	46 ± 0.4 (0.75 ± 0.22)	1.1	32 ± 13 (11 ± 5.5)	0.5
232680		H	n.d.	46 ± 4.0 (0.86 ± 0.56)	1.0	50 ± 2.3 (2.0 ± 0.6*)	2.6
257174		H	61	46 ± 1.8 (0.29 ± 0.10*)	2.9	18 ± 2.5 (1.2 ± 0.4**)	4.3

58

257466	O$_2$S–	H	n.d.	57 ± 4.1 (0.83 ± 0.12)	1.0	23 ± 2.3 (11 ± 6.7)	0.5
224020	morpholino	H	n.d.	32 ± 5.9		3.5 ± 10	
262621	cyclohexyl	F	n.d.	26 ± 8.4		8.2 ± 3.0	
262562	cyclohexenyl	F	n.d.	10 ± 6.8		-0.5 ± 1.3	
258045	cyclohexyl	8-aza	n.d.	14 ± 4.9		7.0 ± 1.1	
258028	cyclohexenyl	8-aza	n.d.	-1.2 ± 6.6		3.0 ± 1.4	
257973	cyclopropyl–(CH$_2$)$_2$–	H	n.d.	31 ± 6.0		7.7 ± 1.9	
257972	cyclopropyl–CH=CH–	H	n.d.	29 ± 4.8		10 ± 6.8	
258451	cyclopropyl–C≡C–	H	n.d.	11 ± 3.2		-6.0 ± 8.0	
258907	cyclobutyl–(CH$_2$)$_2$–	H	n.d.	26 ± 4.9		8.7 ± 6.8	
257962	cyclopentyl–(CH$_2$)$_2$–	H	n.d.	3.2 ± 10		4.8 ± 5.5	
257961	cyclopentyl–CH=CH–	H	n.d.	44 ± 1.0		13 ± 4.6	
259141	H	cyclopentyl–(CH$_2$)$_2$–	n.d.	4.7 ± 7.1		5.2 ± 2.0	
259112	H	cyclopentyl–CH=CH–	n.d.	8.8 ± 2.5		6.5 ± 2.3	
262549	cyclopentyl–(CH$_2$)$_2$–	F	n.d.	-4.4 ± 7.2		-7.1 ± 4.0	
262502	cyclopentyl–CH=CH–	F	n.d.	2.9 ± 3.2		-0.2 ± 2.4	
257303	cyclohexyl–(CH$_2$)$_2$–	H	n.d.	-1.9 ± 2.3		-4.1 ± 3.7	
257300	cyclohexyl–CH=CH–	H	n.d.	13 ± 1.3		4.3 ± 0.7	

toward both kinases. Surprisingly, formylation or acetylation of the heterocyclic nitrogen in 232867 and 232681, respectively, significantly improved potency toward TBK1. The installation of a tetrahydropyranyl group had no significant effect on potency whereas introduction of a double bond in 232680 significantly improved potency toward IKKε. In contrast to 232607, the presence of a sulfur in 257174 significantly improved potency toward both kinases while no improvement was observed for the sulfone-containing ring 257466. The morpholinyl containing analog 224020 displayed a decrease in inhibition toward TBK1 and was essentially inactive toward IKKε.

A series of analogs bearing saturated rings appended to the C-7 or C-8 positions through short linkers were examined. All analogs were poor inhibitors of either kinase, likely due to poor solubility in the assay conditions. Installation of saturated or monounsaturated 6 membered rings at the C-8 position diminished inhibition possibly due to the introduction of steric clashes with the kinase hinge.

3.3.3. Structure-activity relationships of dual C-3 and C-7 modified analogs of amlexanox.

We previously reported that the installation of tetrazole acid bioisosteres at the C-3 position enhances potency toward both kinases (**Table 3.3**). The combination of a tetrazole and C-7 cyclohexyl moiety in 257407 exhibited the same potency toward TBK1 as the cyclohexyl-only 232643. However, the potency of 257407 against IKKε was significantly increased relative to 232643. A more than 20-fold increase in potency to 210 nM toward IKKε was observed for

Table 3.3: Potency of C-3 and C-7 Substituted 5-Oxo-5*H*-[1]benzopyrano[2,3-*b*]pyridines

CCG#	R$_7$	R$_3$	Aq. sol. (μM)[a]	[b]Single Concentration % Inhibition [c](IC$_{50}$, μM)			
				TBK1	IC$_{50}$ Fold Change	IKKε	IC$_{50}$ Fold Change
Amlexanox	*i*-Pr	CO$_2$H	172	50 ± 1.3 (0.85 ± 0.14)		29 ± 7.4 (5.1 ± 1.6)	
257407	cyclohexyl	tetrazole	n.d.	64 ± 1.5 (1.9 ± 0.2*)	0.4	30 ± 2.2 (1.0 ± 0.3*)	5.1
257394	cyclohexenyl	tetrazole	n.d.	52 ± 3.3 (0.49 ± 0.05*)	1.7	79 ± 2.1 (0.21 ± 0.06***)	24
257393	Me$_2$N	tetrazole	n.d.	33 ± 0.6 (0.53 ± 0.16)	1.6	65 ± 1.3 (0.58 ± 0.2***)	8.8
224481	morpholine	tetrazole	916	34 ± 3.6 (0.54 ± 0.10)	1.6	70 ± 1.1 (0.31 ± 0.14***)	16
224483	morpholine	acyl-tetrazole	n.d.	49 ± 0.5 (0.76 ± 0.11)	1.1	57 ± 1.7 (1.2 ± 0.4**)	4.3

[a]Thermodynamic solubility determined by Analiza Inc, Cleveland, OH 44114. [b]TBK1, (1 μM); IKKε (5 μM) (n=3, mean ± SEM). [c] Concentration for 50% inhibition in radiometric kinase assays using purified protein. Reported as IC$_{50}$ (μM) ± SEM (n=3). Significance relative to amlexanox determined by a two-tailed Student's T-test (*p<0.05, **p<0.01, ***p<0.001).

257394 which contained a cyclohexenyl substitution, consistent with prior observations that IKKε favors an unsaturated bond on C-7 modifications. Significant increases in potency were also observed for the dimethyl amine and morpholinyl analogs bearing tetrazole or amide-linked tetrazole modifications. Interestingly, analog 224181 was a potent 310 nM inhibitor of IKKε despite the morpholinyl-only analog 224020 having no inhibitory effect on IKKε, suggesting the tetrazole moiety is the primary driver of potency in this class of analogs.

3.3.4. TBK1 co-crystal structures with C-7 modified analogs. To verify the binding mode of analogs, select inhibitors were co-crystallized with TBK1 (**Figure 3.2, Table 3.4**). To represent the series of analogs with extended non-cyclic C-7 modifications such as 258762 and 258727, the more soluble analog 232241 was co-crystallized with TBK1 and the structure determined to 3.19 Å spacings (PDB 6CQ0, **Figure 3.2 A**). The core of the inhibitor binds identically to amlexanox along the kinase hinge. Weak density is observed for the dimethyl amino tail upon refinement which is positioned near Pro90 and Cys91. The placement of the C-7 tail in solvent may explain why no significant changes in potency are observed, however these analogs are generally less soluble which may also contribute to reductions in potency. The placement of the tail near Cys91, which is likely in the thiolate form due to its proximity to Arg143, suggests that incorporation of an acrylamide in place of the dimethyl amine in 232241 may serve as a strategy for covalent inhibitor design targeting Cys91.

To represent cyclic C-7 analogs, we determined the structure of TBK1 in complex with 257089 at 3.2 Å and 257466 at 3.35 Å resolution (PDB 6CQ4 and 6CQ5, **Figure 3.2 B,C**). Both structures reveal binding along the hinge as observed for all inhibitors bearing the amlexanox pharmacophore. The C-7 rings extend into solvent between the kinase and dimerization domains
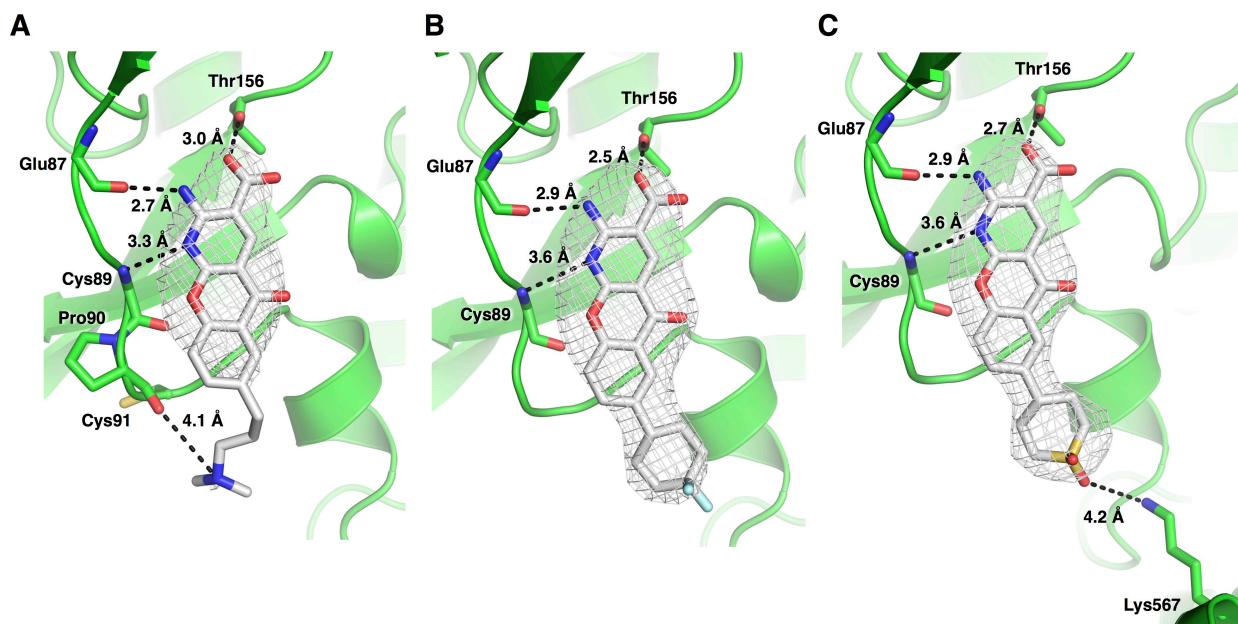
Figure 3.2: TBK1 co-crystal structures with **A)** 232241, **B)** 257089, and **C)** 257466. Mesh represents positive $|F_o| - |F_c|$ omit density contoured at 3 σ. The amino pyridine portion of the inhibitor core interacts with the backbone of Glu87 and Cys89 in the hinge of the kinase and the carboxylate with Thr156 adjacent to the DFG motif. The structures have been deposited in the PDB with the accession codes 6CQ0, 6CQ4, and 6CQ5, respectively.

of TBK1. The lack of interaction between the 4,4-difluorocyclohexyl modification on 257089 and TBK1 and decreased solubility explains why the analog displays decreased inhibition of both kinases. The sulfone-containing ring on 257466 also does not interact with the kinase but is within range of Lys567 and Lys568 which may form favorable electrostatic interactions with the sulfone carbonyl.

3.3.5 Efficacy of select C-7 modified analogs. Cellular and *in vivo* efficacy was assessed by the Saltiel Lab (University of California - San Diego) first assayed in cultured adipocytes and IL-6 secretion, a biomarker of TBK1 and IKKε inhibition (Reilly *et al.*, 2015), assessed with additional testing for promising compounds in obese mice (**Figure 3.3**). A subset of the results are reported here for the C-7 2-propenyl analog of amlexanox (258702), vinylcyclopentyl

Table 3.4: TBK1 Crystallographic data collection and refinement statistics.

Ligand	232241	257089	257466
Wavelength (Å)	0.97857	1.03312	0.97857
Resolution range	48.2 - 3.19 (3.30 - 3.19)*	48.0 - 3.20 (3.31 - 3.20)*	44.1 - 3.35 (3.47 - 3.35)*
Space group	$P\,3_2\,2\,1$	$P\,3_2\,2\,1$	$P\,3_2\,2\,1$
Unit cell constants (Å, º)	134.8 134.8 85.5 90 90 120	134.6 134.6 84.5 90 90 120	134.8 134.8 85.2 90 90 120
Total reflections	237693 (19958)	300633 (29913)	99937 (9694)
Unique reflections	15107 (1359)	14851 (1454)	12948 (1269)
Multiplicity	15.7 (14.7)	20.2 (20.6)	7.7 (7.6)
Completeness (%)	98.9 (90.2)	99.6 (98.0)	98.7 (97.7)
Mean I/σ(I)	18.98 (1.53)	16.59 (1.94)	16.61 (1.80)
Wilson B-factor	112.8	117.6	115.9
R_{meas}	0.122 (2.07)	0.124 (1.71)	0.108 (1.41)
$CC_{1/2}$	0.999 (0.49)	0.999 (0.79)	0.999 (0.50)
Reflections used in refinement	15093 (1355)	14823 (1450)	12931 (1269)
Reflections used for R_{free}	762 (71)	737 (71)	651 (64)
R_{work}	0.238 (0.394)	0.233 (0.387)	0.231 (0.363)
R_{free}	0.293 (0.468)	0.273 (0.452)	0.275 (0.374)
Number of non-hydrogen atoms	4902	4910	4899
Protein	4877	4883	4872
Ligand	25	27	27
RMS bonds (Å)	0.001	0.002	0.002
RMS angles (º)	0.36	0.41	0.43
Ramachandran favored (%)	96.1	96.3	95.8
Ramachandran allowed (%)	3.7	3.5	4.0
Ramachandran outliers (%)	0.2	0.2	0.2
Rotamer outliers (%)	0.56	0.00	0.00
Clashscore	3.9	4.8	4.5
Average B-factor	140	149	135
Protein	140	150	135
Ligand	123	103	103
PDB Entry	6CQ0	6CQ4	6CQ5

*Statistics for the highest-resolution shell are shown in parentheses.

(257961), and cyclohexyl (232643). Despite 258702 displaying improved potency toward IKKε, cellular response to treatment was equivalent to that of amlexanox (**Figure 3.3 A**). The vinylcyclopentyl analog displayed a significant increase in IL-6 secretion in cultured cells and was also tested in obese mice (**Figure 3.3 B**). Treatment with 257961 produced no significant weight loss in a short time course (**Figure 3.3 C**) but did significantly improve insulin sensitivity as determined by blood glucose testing after sugar administration (**Figure 3.3 D**). The cyclohexyl analog 232643 robustly stimulated IL-6 secretion (data not shown) and was evaluated in obese mice over four weeks. Significant weight loss was observed (**Figure 3.3 E**) but was not greater than amlexanox treatment. Taken together, it appears that the weight loss effect of amlexanox treatment may represent the ceiling for response through engagement of TBK1 and IKKε.

3.3.6. Design and evaluation of truncated amlexanox pharmacophore analogs. As the solvent exposed A ring on amlexanox is not involved in any direct interactions with the kinase, elimination of the ring from the inhibitor core may yield an inhibitor with improved ligand efficiency and will explore new chemical space. In collaboration with Hollis Showalter and Xinmin Gan in the Vahlteich Medicinal Chemistry Core, a truncated form of the amlexanox pharmacophore was designed based off manual modeling and docking into the TBK1·amlexanox structure (PDB 5W5V, **Figure 3.4**, **Table 3.5**). The core, which is not reported previously and required the development of a novel synthesis, retains the critical amino pyridine hinge binding moiety and carboxylate. The primary derivatization point is the C-3 position that is analogous to the C-7 position in amlexanox. Introduction of a C-3 *trans*-2-*i*-pentyl group results in a close mimic to amlexanox, whereas a shorter *i*-Bu resembles the C-6 isomer of amlexanox (262826).

At the present time, preparation of analogs based off the truncated amlexanox core is
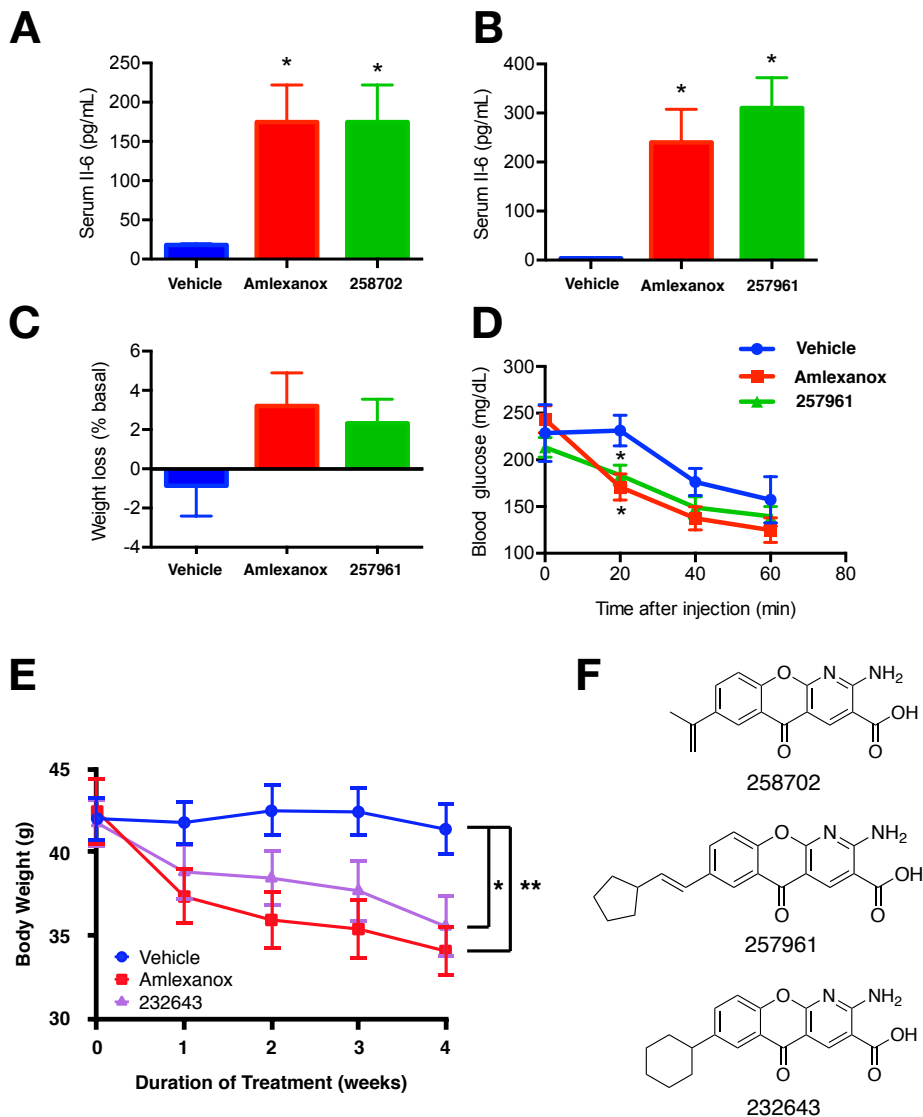
Figure 3.3: Cellular and *in vivo* response to select C-7 modified amlexanox analogs. **A, B)** Secreted IL-6 from 3T3-L1 adipocytes treated with 100 μM compound for 4 hr. **C)** Mean weight loss relative to starting weight and **D)** blood glucose levels after sugar injection in obese mice treated with compound for 2 weeks. **E)** Time course weight loss in obese mice treated with compound. **F)** Chemical structures of analogs assayed. Assays were performed by Shannon Reilly in the Saltiel Lab. Cellular experiments were performed three times and animal studies once with three animals. Statistical significance determined by one-way ANOVA (*$p<0.05$, ** $p<0.01$). Significance in A-C was determined relative to the vehicle control, D at each time point, and E at the final time point.
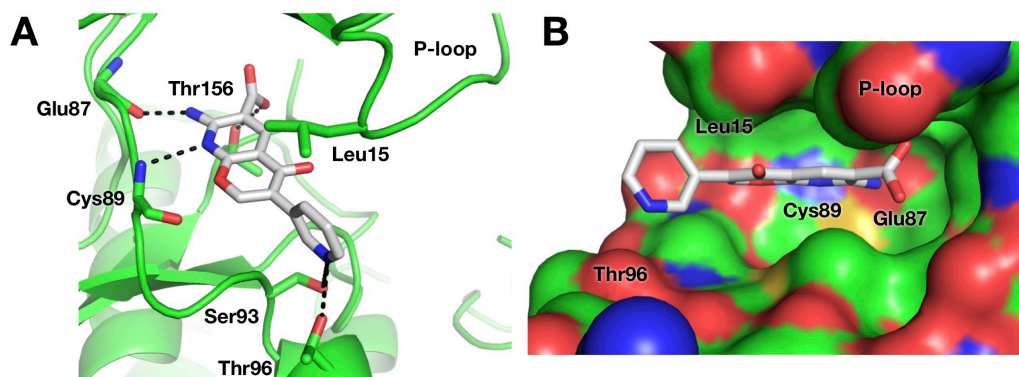
Figure 3.4: Docking of truncated amlexanox analog 263870 with deprotected carboxylate. **A)** AutoDock Vina docking pose assuming identical hinge contacts as with amlexanox. The pyridine nitrogen is predicted to interact with the sidechain of either Ser93 or Thr96. **B)** Surface representation of deprotected 263870 docked along the kinase hinge. Docking was performed with PyRx using the AutoDock Vina algorithm.

Table 3.5: Potency of pyrano[2,3-*b*]pyridines
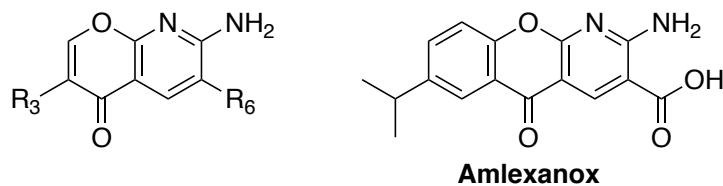
Amlexanox

CCG#	R$_3$	R$_6$	^{a}Single Concentration % Inhibition ^{b}(IC$_{50}$, μM)			
			TBK1	IC$_{50}$ Fold Change	IKKε	IC$_{50}$ Fold Change
Amlexanox			50 ± 1.3 (0.85 ± 0.14)		29 ± 7.4 (5.1 ± 1.6)	
263758	*i*-Pr	COOH	2.9 ± 3.2 (11)	0.1	6.1 ± 0.2 (11)	0.5
263869	*i*-pentyl	COOEt	0.2 ± 3.2		9.1 ± 4.5	
263870	(3-pyridyl)	COOEt	-5.7 ± 7.1		10.8 ± 2.9	
263882	*i*-pentyl	COOH	10.1 ± 2.6		5.6 ± 0.4	

^{a}TBK1, (1 μM); IKKε (5 μM) (n=3). ^{b} Concentration for 50% inhibition in radiometric kinase assays using purified protein. Reported as IC$_{50}$ (μM) ± SEM (n=3 for amlexanox, n=1 for 263758).

difficult due to the base sensitivity of the electrophilic dihydropyran ring, especially during

deprotection of the carboxylic acid. Therefore, a limited number of analogs have been

synthesized to assess the inhibitory potential of this ring system. Installation of an *i*-Pr or *i*-pentyl

group diminished potency by an order of magnitude likely due to decreased buried hydrophobic

surface area. The ethyl ester congener of 263882 also displayed little inhibition towards either

kinase, in line with prior observations regarding the modification of the carboxylate on

amlexanox. Docking indicated that the addition of a pyridine at the R_3 position may form

favorable contacts with the large lobe of the kinase domain while simultaneously packing against

the P-loop. Unfortunately, deprotection of the carboxylate was not achieved and thus the

compound was supplied as the protected ethyl ester which displayed very poor inhibition as

anticipated from compound 224182.

3.4 Discussion

We are utilizing the clinically approved drug amlexanox, a modest inhibitor of TBK1 and

IKKε, as a starting point for analog synthesis in order to develop inhibitors to test a novel

hypothesis about the role of inflammation in the generation of insulin resistance and type 2

diabetes during obesity. I previously determined the TBK1·amlexanox crystal structure which

revealed canonical ATP-competitive binding along the kinase hinge and demonstrated the

importance of the carboxylic acid for potent inhibition. Here, we extensively modified the

solvent exposed A ring of amlexanox to improve potency and pharmacokinetic properties and

investigate the effects of simultaneous substitution at two positions.

Analogs with a 2-propenyl substituent favor binding to IKKε relative to isopropyl

congeners, possibly due to the planarity of the sp^2 carbon center (compare 258702 vs amlexanox, 262485 vs 262501, and 259012 vs 259043). The presence of a Ser residue in the hinge of IKKε, in contrast to a Pro in TBK1, should affect the flexibility of the hinge region and, in conjunction with the planar 2-propenyl, may allow for more kinase domain closure and improved binding. This trend is in line with prior SAR surrounding the C-3 position of amlexanox in which more extensive modifications were only accommodated by IKKε. This trend does not apply to 8-aza analogs (258073 vs 258101) in which the isopropyl congener 258101 shows a greater fold change in binding relative to amlexanox. For binding to 8-aza analogs, the hinge region may assume a conformation that allows for a hydrogen bond to form with the kinase backbone. This possibility is supported by the TBK1·amlexanox crystal structure wherein the hinge would need to change conformation in order for an 8-nitrogen to interact with the kinase backbone.

Based off prior structural studies with amlexanox, analogs bearing cyclic C-7 modifications were predicted to assume an unusual binding mode for a kinase inhibitor in which the modification extends through solvent and contacts the neighboring dimerization domain. As such a binding mode is uncommon, a completely different binding mode along the hinge was envisioned wherein the cyclic modification would be positioned under the P-loop. Docking experiments also indicated the potential for global rearrangement of the inhibitor binding mode. However, two independent co-crystal structures confirmed that the inhibitor core binds identically to amlexanox along the hinge. Rings containing heteroatoms at the 4 position may interact with Tyr564, Lys570, or Lys576 such as with 257174 and 257466. More extended ring modifications such as acetylated piperidine in 232681 and ketal in 257366 and 257344 may begin to form contacts with the backbone of the dimerization domain.

The installation of saturated hydrocarbon rings at the C-7 position is tolerated in size up to cyclohexyl after which potency markedly decreases likely as a result of poor solubility and excessive bulk near the kinase hinge and P-loop. In line with the prior observation that IKKε prefers unsaturated bonds adjacent to the C-7 position, analogs 232780 and 232925 retain inhibition of IKKε while TBK1 inhibition is decreased. Appending saturated rings via short aliphatic linkers was detrimental to inhibition due to extremely poor solubility. However, analogs containing C-7 saturated ring substitutions display enhanced cellular response and *in vivo* efficacy likely as a result of their lipophilicity enhancing cellular permeability.

Among the most striking results from the C-7 modified analogs are dual modification with C-3 acid bioisosteres previously described. The analog 224120 bearing a tetrazole at the C-3 position was previously described to display a potency of 200-300 nM toward both TBK1 and IKKε. When combined with a 6-membered hydrocarbon ring, dimethyamine, or morpholine there is no significant change in potency relative to amlexanox. Strikingly, potency toward IKKε is significantly improved by nearly 25-fold compared to amlexanox to 210 nM in the case of a C-7 cyclohexene, as IKKε prefers planarity near the hinge, and a C-3 tetrazole. This potency is comparable to the tetrazole only analog 224120 suggesting that interactions with the gatekeeper Met86 drives potency even when unfavorable modifications such as a C-7 morpholine are present. Selectivity toward IKKε for dually modified analogs may stem from potentially increased hinge flexibility allowing for the accommodation of two additional rings off the amlexanox pharmacophore. Conversely, the installation of an amide linked tetrazole at the C-3 position was previously shown to decrease potency toward TBK1. However, when combined with a C-7 morpholine, potency is comparable to that of amlexanox. Thus, it appears that

70

modifications at the C-3 and C-7 positions influence each other in both directions to overcome unfavorable modifications at the opposite end of the inhibitor.

In an attempt to optimize the pharmacophore of amlexanox, a novel truncated ring system was designed with the assistance of available co-crystal structures wherein the A ring of amlexanox was eliminated. As the A ring does not make any polar contacts, elimination should not significantly perturb binding while entering novel chemical space. However, synthesis of this ring system is challenging and most analogs contained a protected carboxylate group which display poor potency. Interestingly, 263758 and 263882 which contain a free acid group and hinge binding atoms are poor inhibitors of either kinase. Loss of the A ring of the pharmacophore may destabilize the P-loop of the kinase by reducing Van der Waals contacts between Leu15 and the inhibitor core. Thus, a pyridine containing analog was designed which docking suggests may stabilize the P-loop by packing the hydrophobic side of the pyridine ring against Leu15 while simultaneously hydrogen bonding with side chains in the large lobe of the kinase domain. Unfortunately, deprotection of the carboxylate on the designed pyridine analog was not achieved, though the protected analog 263870 displayed weak inhibition against IKKε suggesting future promise for the deprotected version once synthesized.

In light of the surprising results of combining C-3 and C-7 modification on amlexanox, dual modification of the truncated pharmacophore warrants exploration. One such target is the pyridine analog 263870 bearing a tetrazole in place of the ethyl ester. Docking indicates such an analog would retain an amlexanox-style binding mode while greatly improving potency (data not shown). As the pyridine and dual modification analogs are more potent toward IKKε, additional selectivity may be achieved while improving potency to <200 nM.

Taken together, structural and pharmacological characterization of amlexanox as an inhibitor of TBK1 and IKKε has yielded insights into the SAR of the amlexanox pharmacophore. In addition to the observations made in Chapter 2 regarding the necessity of the carboxylate for TBK1 inhibition and dramatic potency improvements through the installation of acid bioisosteres, we have determined that the introduction of saturated hydrocarbon rings at the C-7 position greatly improve efficacy and that the modification of both the C-3 and C-7 positions yields potent IKKε inhibitors. This work has produced several analogs, namely 232643, with clinical potential that are undergoing preclinical profiling.

Chapter 4: Biophysical Characterization and Perturbation of the Ca²⁺·CaM–GRK5 Interaction

4.1. Introduction

   G protein-coupled receptors (GPCR) are the largest family of cell-surface receptors in humans and regulate numerous physiological processes through the activation of heterotrimeric G proteins, GPCR kinases (GRKs) and arrestins. To maintain proper physiology, mechanisms to attenuate or cease downstream signaling have evolved. The principal desensitization mechanism is initiated by GRKs which phosphorylate the third intracellular loops or C-terminal tails of active GPCRs, thereby facilitating the recruitment of arrestin which sterically occludes G protein binding and promotes receptor internalization (Tesmer, 2016).

   As membrane localization and recognition of activated receptors is critical for efficient receptor desensitization, several regulatory mechanisms have evolved to attenuate GRK activity and prolong receptor activation. The ubiquitous calcium-sensing protein calmodulin (CaM) binds all GRKs and inhibits both membrane localization and receptor phosphorylation in a Ca^{2+}-dependent manner (Chuang *et al.*, 1996; Pronin *et al.*, 1997; Levay *et al.*, 1998; Iacovelli *et al.*, 1999) without significantly affecting phosphorylation of most soluble substrates (Chuang *et al.*, 1996). The interaction between Ca^{2+}·CaM and GRK5 has been the most studied due to its high affinity (K_d=8 nM by surface plasmon resonance) and 50-fold greater potency (IC_{50}=40-60 nM toward rhodopsin phosphorylation) compared to other GRKs (Chuang *et al.*, 1996; Pronin *et al.*, 1997). Pulldown experiments showed Ca^{2+}·CaM affinity toward GRK5 was mediated by

contacts with the N-terminal helix (residues 1-17), C-terminal amphipathic helix (residues 552-561, **Figure 1.3 B**), and a phospholipid-interacting patch of basic residues (residues 20-39) near the junction between the kinase domain and regulator of G protein signaling homology (RH) domains (Pronin *et al.*, 1997; Levay *et al.*, 1998). More recently, $Ca^{2+} \cdot CaM$ was shown to directly strip peptides corresponding to the GRK5 N- and C-terminal regions from model membranes (Ding *et al.*, 2014). Interestingly, the binding of $Ca^{2+} \cdot CaM$ promotes GRK5 autophosphorylation at non-canonical C-terminal sites that further reduce the ability of GRK5 to associate with membranes and may represent a mechanism prolong GRK5 inhibition after $Ca^{2+} \cdot CaM$ has dissociated (Pronin *et al.*, 1997; Levay *et al.*, 1998).

Conflicting models for the $Ca^{2+} \cdot CaM$–GRK5 complex have been proposed. One depicts two $Ca^{2+} \cdot CaM$ simultaneously binding distal N- and C-terminal elements of GRK5 in a fashion that would interfere with its membrane binding and receptor phosphorylation. (Levay *et al.*, 1998). Alternatively, recent structures of GRK5 have revealed the N- and C-terminal elements to be in close proximity to one another, and thus a single $Ca^{2+} \cdot CaM$ may bind both simultaneously, although this would likely require a non-canonical interaction where each lobe binds to a separate element. (Komolov *et al.*, 2015; Homan, Waldschmidt, *et al.*, 2015; Beyett *et al.*, 2016).

GRK5 inhibition by $Ca^{2+} \cdot CaM$ is of growing interest because is plays a role in the development of cardiac hypertrophy during heart failure. To better understand the molecular mechanism of inhibition of GRK5 by $Ca^{2+} \cdot CaM$, we used multi-angle light scattering (MALS), small-angle X-ray scattering (SAXS) and negative stain electron microscopy (EM) to determine the architecture of the $Ca^{2+} \cdot CaM$–GRK5 complex. Our data reveal that a single $Ca^{2+} \cdot CaM$ binds at the junction of the regulator of G protein signaling homology (RH) and kinase domains of

GRK5 where Ca^{2+}·CaM is poised to interact with elements of the kinase critical for receptor recognition and allosteric activation, but also within reach of the C-terminal membrane-binding. We confirm that the binding of Ca^{2+}·CaM promotes an active conformation of GRK5 resulting in increased phosphorylation of non-receptor substrates. We investigated the outcome of disrupting the Ca^{2+}·CaM–GRK5 interaction through the application of the natural product malbrancheamide, a known Ca^{2+}·CaM inhibitor believed to block the C-lobe of the protein (González-Andrade *et al.*, 2016). Co-crystallization of malbrancheamide in complex with Ca^{2+}·CaM confirmed that the natural product stabilizes an unusual conformation of Ca^{2+}·CaM by binding to the C-terminal lobe while leaving the N-terminus exposed in a state that is free to interact with other proteins. This binding mode allows malbrancheamide to suppress Ca^{2+}·CaM-stimulated GRK5 membrane dissociation, and hence autophosphorylation, without relieving the ability of Ca^{2+}·CaM to suppress receptor phosphorylation.

4.2. Materials and methods

4.2.1. Calmodulin protein expression and purification. Human calmodulin (CaM) was inserted into pMCSG7 using ligation-independent cloning, confirmed with Sanger sequencing, and transformed into *E. coli* BL21 DE3 pLysS cells. Cells were grown at 37 ˚C in TB to an optical density at 600 nm of 0.6-1.0, cooled to 20 ˚C, and induced with 0.5 mM IPTG overnight. Cells were harvested by centrifugation were resuspended in lysis buffer composed of 20 mM HEPES pH 8.0, 200 mM NaCl, 40 mM imidazole, 5 mM CaCl$_2$, 1 mM DTT, leupeptin, lima bean trypsin protease inhibitor, and 0.1 μM PMSF and lysed by sonication. Lysate was clarified by centrifugation for 30 min at 15,000xg. After centrifugation, the supernatant was glass filtered

and slowly flowed through Ni-NTA resin. The resin was washed with lysis buffer and CaM eluted with lysis buffer supplemented with an additional 200 mM imidazole. Eluted CaM was further purified via size exclusion chromatography (SEC) on an analytical S75 column in 20 mM HEPES pH 8.0, 200 mM NaCl, 5 mM $CaCl_2$, and 1 mM DTT. CaM of ≥95% purity by SDS-PAGE was aliquoted, flash frozen, and stored at -80 ºC. Calmodulin protein concentrations were determined by absorbance at 280 nm using a calculated molecular weight of 19,580 Da and extinction coefficient of 4,470 M^{-1} cm^{-1}. His-tagged N- or C-terminal lobes (residues 1-75 and 78-149, respectively) of CaM were expressed and purified as described above for full-length CaM.

4.2.2. GRK5 protein expression and purification. Human GRK5 with a C-terminal hexahistidine tag was cloned into a modified pFastBac HTB lacking the N-terminal hexahistidine tag and verified by Sanger sequencing. High-titer recombinant baculovirus was prepared using the Bac-to-Bac protocol and used to infect Sf9 or Hi5 insect cells at a density of $2x10^6$ cells mL^{-1} for 48-60 hrs. Cells were pelleted and flash frozen in liquid nitrogen. GRK5 insect cell pellets were resuspended in lysis buffer containing 20 mM HEPES pH 8.0, 100 mM NaCl, 40 mM imidazole, 1 mM DTT, and 0.1 μM PMSF, leupeptin, and lima bean trypsin protease inhibitor and briefly sonicated. Lysis was verified by examination of the cells under a microscope. Lysate was clarified by ultracentrifugation for 1 h at >200,000xg. After centrifugation, the supernatant was glass filtered and slowly flowed through Ni-NTA resin. The resin was washed with lysis buffer and GRK5 eluted with lysis buffer supplemented with an additional 200 mM imidazole. Eluted GRK5 was further purified via cation exchange chromatography on a HiTrap S column with a gradient of 0.0-1.0 M NaCl at pH 8.0. Fractions containing GRK5 were combined and run

over an S200 SEC column in 20 mM HEPES pH 8.0, 200 mM NaCl, and 1 mM DTT. GRK5 of

$\geq$95% purity by SDS-PAGE was aliquoted, flash frozen, and stored at -80 ˚C. GRK5 protein

concentrations were determined by absorbance at 280 nm using a calculated molecular weight of

70,660 Da and extinction coefficient of 60,280 M^{-1} cm^{-1}. Lyophilized terminal peptides

encompassing the N-terminal helix (αN, residues 2-31) and C-terminal helix (αC, residues

546-565) were prepared via solid-phase peptide synthesis as described previously and

resuspended in DMSO (Ding *et al.*, 2014).

4.2.3. Determination of Ca^{2+}·CaM·malbrancheamide structure. Ca^{2+}·CaM at 10-12 mg

mL^{-1} was incubated at room temperature with 2 molar equivalents of malbrancheamide in buffer

containing 5 mM CaCl$_2$ for 30 min. Sitting drop sparse-matrix screens with 0.5 µL well solution

and 0.5 µL Ca^{2+}·CaM·malbrancheamide were set and incubated at 20 ˚C. Small rod-like crystals

appeared after 1-3 d in well D6 of the Qiagen JCSG+ screen which contains 0.1 M Tris pH 8.5,

0.2 M MgCl$_2$, and 20% (w/v) PEG 8,000. The best diffracting crystals were harvested directly

from the drop without cryoprotection. Diffraction data to 1.96 Å spacings was collected at LS-

CAT (Sector 21, Advanced Photon Source, Argonne National Lab) on an Eiger 9M detector at

100 K. Data were indexed, integrated, and scaled using xia2, DIALS, and AIMLESS (Winn *et

al.*, 2011; Winter *et al.*, 2018; Winter 2010.). Molecular replacement was performed with Phaser

(McCoy *et al.*, 2007) in Phenix (Adams *et al.*, 2010) using one chain of PDB 4HEX. Ligand

restraints were prepared using eLBOW (Moriarty *et al.*, 2009). Reciprocal space refinement was

carried out in Phenix Refine with real space refinement and model building in coot (Emsley *et

al.*, 2010). Graphics were prepared with PyMol (Version 2.1, Schrödinger LLC).

4.2.4. Isothermal titration calorimetry (ITC). ITC was performed with a NanoITC instrument. Malbrancheamide at 600 µM in 20 mM HEPES pH 8.0, 200 mM NaCl, 5 mM $CaCl_2$, and 5% DMSO was slowly titrated into a solution of 80 µM $Ca^{2+}\cdot$CaM in an identical buffer. The heat of binding was analyzed using Nano Analyze software and fit to a sigmoidal binding curve to obtain the binding affinity (K_d) and stoichiometry. ITC was repeated three times and statistical significance determined via Student's two-tailed T-test.

4.2.5 Radiometric kinase assays. Kinase assays were performed with 50 nM purified human GRK5 and 5 µM light activated bovine rhodopsin in native membranes, 5-10 µM porcine tubulin monomer, or 7 µM bovine myelin basic protein (MyBP) in buffer containing 20 mM HEPES pH 8.0, 10 mM $MgCl_2$, 0.5 mM $CaCl_2$, and 1 mM DTT. CaM, peptides, and/or malbrancheamide were added and the reactions initiated with 10 µM ATP spiked with $[\gamma\text{-}^{32}P]$-ATP and allowed to proceed for 2-5 min at room temperature prior to quenching with SDS loading dye. Samples were separated on 4-15% polyacrylamide gels, dried, and exposed overnight on phosphor screens. Screens were imaged on a Typhoon imager, band intensities quantified using ImageQuant, and fit to a three parameter dose-response model in GraphPad Prism. Data were normalized such that the background intensity = 0% kinase activity and a sample lacking calmodulin and/or inhibitors = 100% kinase activity.

4.2.6 Complex formation and light scattering. Purified GRK5 and $Ca^{2+}\cdot$CaM were mixed in a 1:3 molar ratio, supplemented with 5 mM $CaCl_2$, and incubated at 4 ˚C for 30 min prior to separation by size exclusion chromatography using an analytical S200 10/300 column. Approximately 500 µg of GRK5 or $Ca^{2+}\cdot$CaM–GRK5 complex was injected onto Shodex KW-804 liquid chromatography column coupled to a Dawn-Helios multi-angle light scattering

(MALS) detector to determine the molecular weight and stoichiometry of the complex from a standard curve.

4.2.7. Differential scanning fluorometry (DSF). Protein thermal stability was assessed with an HT7900 qPCR instrument using 0.25 mg mL^{-1} GRK5 or Ca^{2+}·CaM–GRK5 complex in assay buffer containing 20 mM HEPES pH 8.0, 5 mM MgCl$_2$, 5 mM CaCl$_2$, and 1 mM DTT, SYPRO Orange protein gel stain (5000x stock in DMSO), and 200 μM ATP or CCG-215022 (Homan, Waldschmidt, *et al.*, 2015; Waldschmidt *et al.*, 2016), Melt curves were obtained by increasing the temperature from 25-60 ˚C at a rate of 2 ˚C min^{-1}. Data were plotted in GraphPad Prism 7 with the inflection point of the sigmoidal curve representing the melting point (T$_m$) of the protein.

4.2.8. Small-angle X-ray scattering (SAXS). SEC-SAXS analysis was performed on purified Ca^{2+}·CaM–GRK5 complex at Bio-CAT (Sector 18, Advanced Photon Source, Argonne National Lab). Approximately 600 μg of GRK5 or complex was injected onto a Superdex-200 10/300 column and the eluted peak corresponding to the complex directly flowed through a 12 keV X-ray beam. Diffraction data were collected on a Pilatus 1M detector with a sample to detector distance of 3.5 m. The achievable Q range for this experimental setup is 0.004-0.33 Å^{-1}.

PRIMUS QT as part of the ATSAS software package was used to process raw SAXS data including data averaging, buffer subtraction, and data merging (Svergun, 1992; Franke *et al.*, 2017). DAMMIN and DAMAVER (Svergun, 1999; Volkov, 2003) was used to generate *ab initio* envelopes containing dummy atoms through iterative rounds of simulated annealing which were averaged together to obtain an unbiased average envelope (Franke and Svergun, 2009). The envelope was then filtered using DAMFILT (Volkov, 2003) to obtain a final, most probable

envelope. GASBOR was also used to generate an *ab initio* envelope by filling space with a dummy peptide containing the same number of $C\alpha$ atoms as found in the protein sample (Svergun *et al.*, 2001). CRYSOL (Svergun *et al.*, 1995) as part of the ATSAS PyMol plugin SASpy (Panjkovich and Svergun, 2016) was used to score models against the raw SAXS data. PyMol (version 2.1, Schrödinger LLC.) was used to manipulate structure coordinates and generate figures.

     4.2.9. Electron microscopy (EM). The $Ca^{2+} \cdot CaM$–GRK5 complex was isolated by SEC as described under *Complex formation and Light Scattering*. For negative stain imaging, protein samples were diluted with buffer (20 mM HEPES, 200 mM NaCl, 5 mM $CaCl_2$, 1 mM DTT) to 0.02-0.05 mg mL^{-1}. The negative staining samples were prepared using conventional negative staining protocol (Peisley and Skiniotis, 2015), and imaged at room temperature with a Technai T12 electron microscope operated at 120 kV using low dose procedures. Images were recorded at a magnification of 71,138x and a defocus value of approximately -1.4 μm on a Gatan US4000 CCD camera. All images were binned (2x2 pixels) to obtain a pixel size of 4.16 Å on the specimen level. Particles were manually picked using e2boxer.py (part of the EMAN2 software suite) (Tang *et al.*, 2007). 2D reference-free alignment and classification of particle projections was performed using ISAC (Z Yang *et al.*, 2012). To simulate 2D projections from the SAXS model, a 20 Å low-pass filter was applied to the high resolution model of $Ca^{2+} \cdot CaM$–GRK5 docked into SAXS envelope in Chimera (Pettersen *et al.*, 2004) and the project3d.py script of EMAN2 suite was used to generate 2D projections with 10˚ rotational spacings.

4.3. Results

4.3.1. Binding, thermal stabilization, and stoichiometry of CaM–GRK5. To better understand how each lobe of $Ca^{2+}\cdot CaM$ differentially regulates GRK5 function, we determined the architecture of the $Ca^{2+}\cdot CaM$–GRK5 complex. GRK5 was incubated with excess CaM and saturating Ca^{2+} prior to separation via analytical size exclusion chromatography (SEC) coupled to a multi-angle light scattering (MALS) detector. MALS analysis of the peak indicated a molecular weight for the complex of approximately 90 kDa indicating a 1:1 stoichiometry (**Figure 4.1 A,B**).

The effect of $Ca^{2+}\cdot CaM$ binding on the stability of GRK5 was next assessed by differential scanning fluorometry (DSF) (**Figure 4.1 C**). The addition of $Ca^{2+}\cdot CaM$ increased the melting temperature (T_m) of GRK5 by 2 ˚C. The addition of ATP or the potent GRK5 inhibitor CCG-215022 (Homan, Waldschmidt, *et al.*, 2015; Waldschmidt *et al.* 2016) increased the T_m of GRK5 by approximately 5 and 6 ˚C, respectively. The same increases in melting temperature were observed for the $Ca^{2+}\cdot CaM$–GRK5 complex, demonstrating that $Ca^{2+}\cdot CaM$ does not interfere with ligand binding and has an overall stabilizing effect on GRK5.

4.3.2. Small-angle X-ray scattering studies of $Ca^{2+}\cdot CaM$–GRK5. Attempts to crystallize the $Ca^{2+}\cdot CaM$–GRK5 complex were unsuccessful, likely due to the highly dynamic nature of the termini of GRK5 and CaM. To determine the arrangement of $Ca^{2+}\cdot CaM$ and GRK5 in complex, we performed small-angle X-ray scattering (SAXS). Purified GRK5 or complex were separated via SEC immediately prior to in-line SAXS analysis, eliminating contaminating aggregates and excess $Ca^{2+}\cdot CaM$ (**Figure 4.2, Table 4.1**). A *b initio* envelopes were generated through simulated annealing with two distinct data processing methods which revealed extra density upon the

81
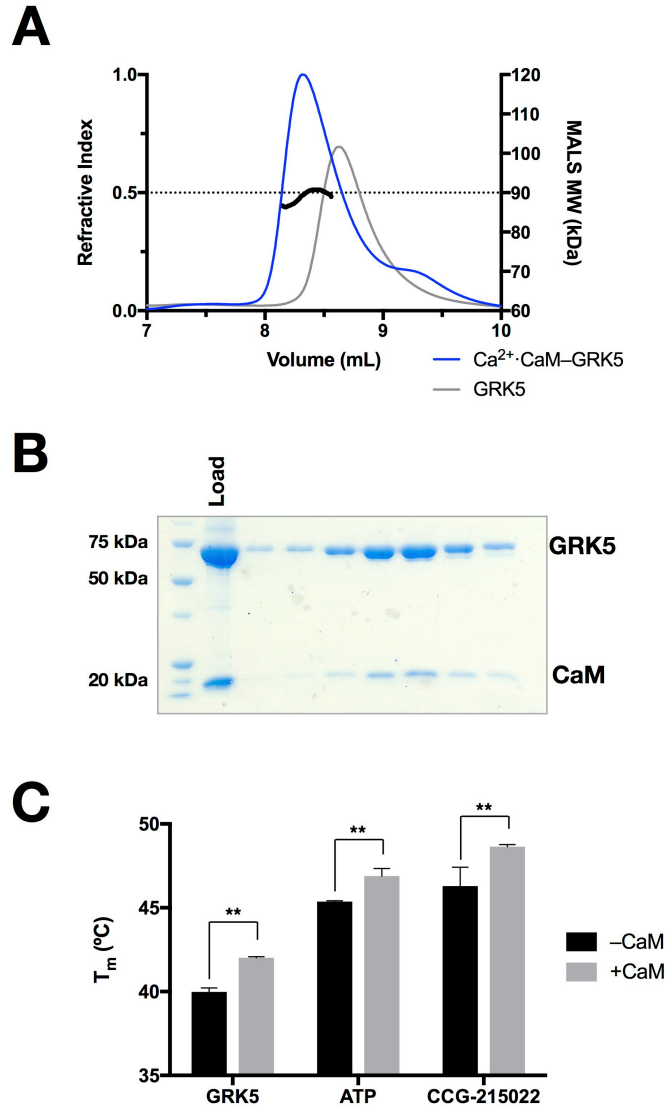
Figure 4.1: Isolation of Ca^{2+}·CaM–GRK5 complex and determination of stoichiometry. **A)** Representative chromatogram of GRK5 and Ca^{2+}·CaM mixed in a 1:3 molar ratio passed over an S200 SEC column. A shift toward a lower elution volume was observed upon the addition of Ca^{2+}·CaM. MALS was used to determine the molecular weight of the complex and is indicated by a solid line inside the peak. The dotted line corresponds to 90 kDa, the approximate weight of a 1:1 complex (n=2). **B)** SDS-PAGE analysis of the chromatogram peak corresponding to the Ca^{2+}·CaM–GRK5 complex. Both proteins co-elute indicating complex formation. Molecular weight ladder is shown on the left with relevant weights indicated. **C)** DSF thermal shift assay of GRK5 in the presence of Ca^{2+}·CaM and/or small molecule ligands. Error bars represent ± standard error of mean (SEM) (n=3, significance between the presence or absence of CaM determined by two-way ANOVA with correction for multiple comparisons, **p≤0.01).
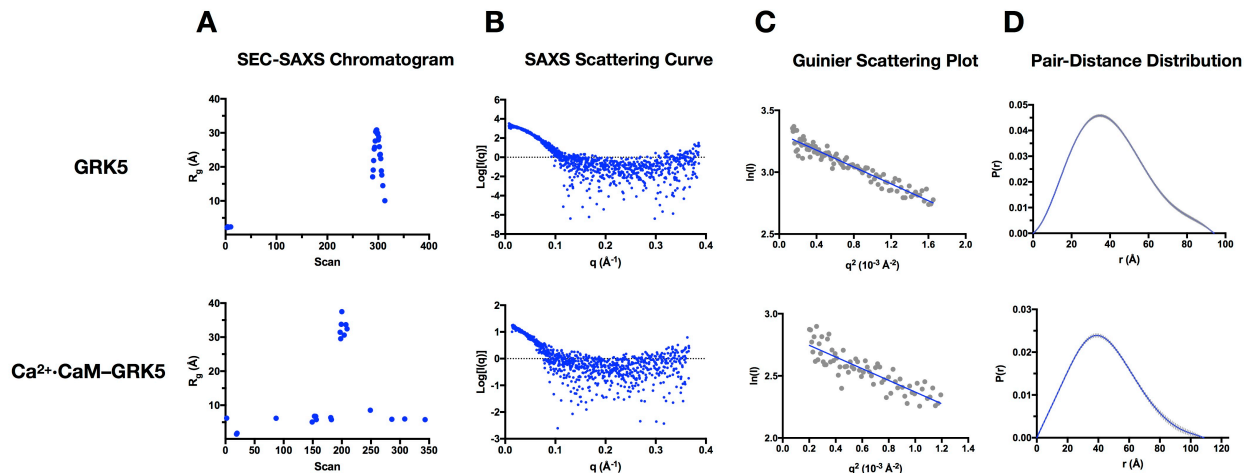
Figure 4.2: SAXS data processing for GRK5 and the $Ca^{2+}\cdot CaM$–GRK5 complex. **A)** SEC-SAXS chromatogram of S200 SEC column. A cluster of scans with R_g between 20-35 Å indicates the elution of the injected protein. Scans with $R_g < 0.1$ Å were omitted for clarity. **B)** Scattering plot of the scans corresponding to the complex. **C)** Guinier plot for the $qR_g < 1.3$ region of the scattering curve. The best-fit line used to calculate I(0) through extrapolation is shown. **D)** Pair-distance distribution [P(r)] for the scattering curve.

SAXS Data Collection Statistics		
	GRK5	**$Ca^{2+}\cdot CaM$–GRK5**
Guinier I(0)	27.4 ± 0.3	17.2 ± 0.4
Guinier R_g (Å)	31.8 ± 0.5	37.3 ± 1.7
Guinier Pearson CC	0.84	0.86
P(r) I(0)	27.0	15.2
P(r) R_g (Å)	31.2	32.2
P(r) Quality of Fit	0.81	0.83
D_{max} (Å)	94	108
Estimated Molecular Weight (kDa)	68	85
Actual Molecular Weight (kDa)	70.7	90.3

Table 4.1: Data collection statistics for SAXS experiments. Zero angle intensity [I(0)], radius of gyration (R_g), and quality of fit/Pearson correlation coefficient derived from Guinier and Pair-distance [P(r)] analyses are displayed. The maximum particle size D_{max} was determined from the largest radius in the P(r) plot (**Figure 4.2 D**). Estimated molecular weight was calculated by dividing the Porod volume by 1.7.[55] Guinier results are reported as average ± SD.
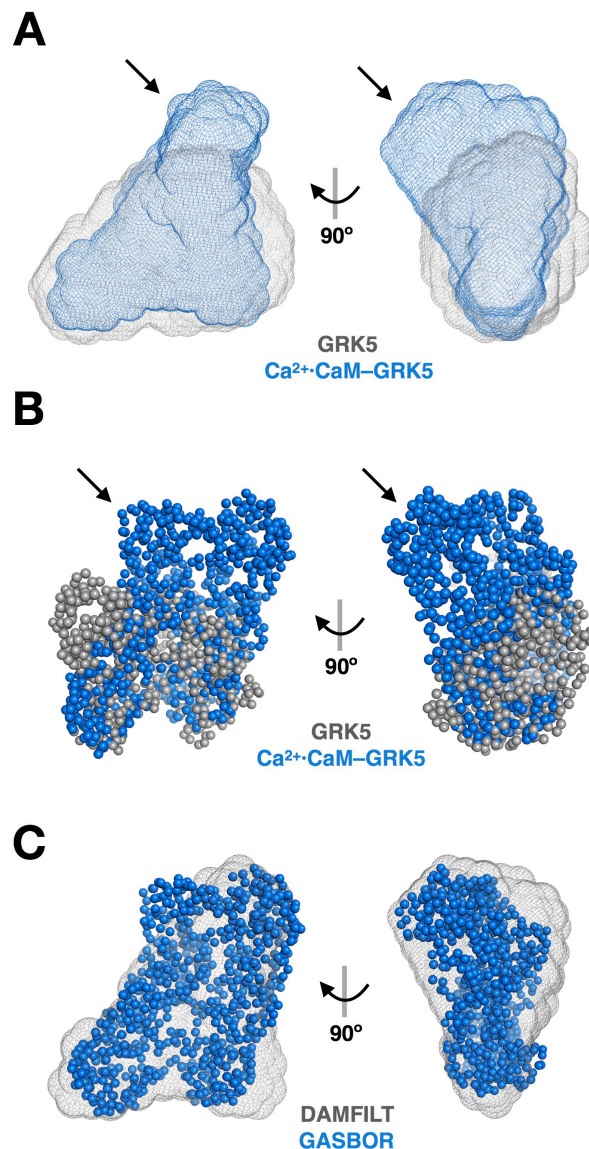
Figure 4.3: Generation of *ab initio* SAXS envelopes. **A)** Filtered envelopes for GRK5 (gray) and $Ca^{2+} \cdot CaM$–GRK5 (blue) generated using space filling dummy beads in DAMMIN. Envelope fits against raw data are $\chi^2 = 0.89$ for GRK5 and $\chi^2 = 0.96$ for $Ca^{2+} \cdot CaM$–GRK5. Extra density upon the addition of $Ca^{2+} \cdot CaM$ is indicated by an arrow. **B)** Mock polyglycine chains (only $C\alpha$ displayed) of the correct length generated in GASBOR representing the approximate shape of GRK5 (gray) and $Ca^{2+} \cdot CaM$–GRK5 (blue). Envelope fits against raw data are $\chi^2 = 0.90$ for GRK5 and $\chi^2 = 1.02$ for $Ca^{2+} \cdot CaM$–GRK5. Extra density upon the addition of $Ca^{2+} \cdot CaM$ is indicated by an arrow. **C)** Comparison of $Ca^{2+} \cdot CaM$–GRK5 envelope from DAMFILT (gray mesh) and polypeptide model from GASBOR (blue spheres).

addition of Ca^{2+}·CaM (**Figure 4.3**). Estimated molecular weights calculated from the envelope

volumes agree well with the actual molecular weights of GRK5 and a 1:1 Ca^{2+}·CaM–GRK5

complex (**Table 4.1**).

The published crystal structure of GRK5 (PDB 4WNK) (Homan, Waldschmidt, *et al.*,

2015) with a modeled N-terminal helix, a known site of Ca^{2+}·CaM binding, and active site tether

(AST) loop from GRK6 (PDB 3NYN) (Boguth *et al.*, 2010) was manually placed in the

envelope alongside Ca^{2+}·CaM (PDB 5J03) (Strulovich *et al.*, 2016). Ca^{2+}·CaM lies along the

small lobe of GRK5 near the N-terminus with its acidic surface adjacent to the basic

phospholipid binding patch (**Figure 4.4**). The AST loop (approximately residues 462-492)

conformation observed in recent GRK5 structures (PDB 4TNB, 4TND) (Komolov *et al.*, 2015) is

strongly influenced by crystal contacts and clashes with Ca^{2+}·CaM in our SAXS model, whereas

the AST conformation observed in GRK4 and 6 structures, which are not influenced by crystal

contacts, are compatible with this Ca^{2+}·CaM binding mode. In this conformation, the

phospholipid binding patch (residues 20-39) projects basic side chains toward several acidic

residues on Ca^{2+}·CaM, likely forming an extensive salt bridge network. Modeling of a C-

terminus onto GRK5 projects the αC helix toward the density for one lobe of Ca^{2+}·CaM. The

positioning of Ca^{2+}·CaM along the surface of the small lobe of the kinase domain does not

obscure the substrate or ATP binding pockets, which is consistent with the observation that

GRK5 retains catalytic activity toward soluble substrates and autophosphorylation when in

complex (Chuang *et al.*, 1996).
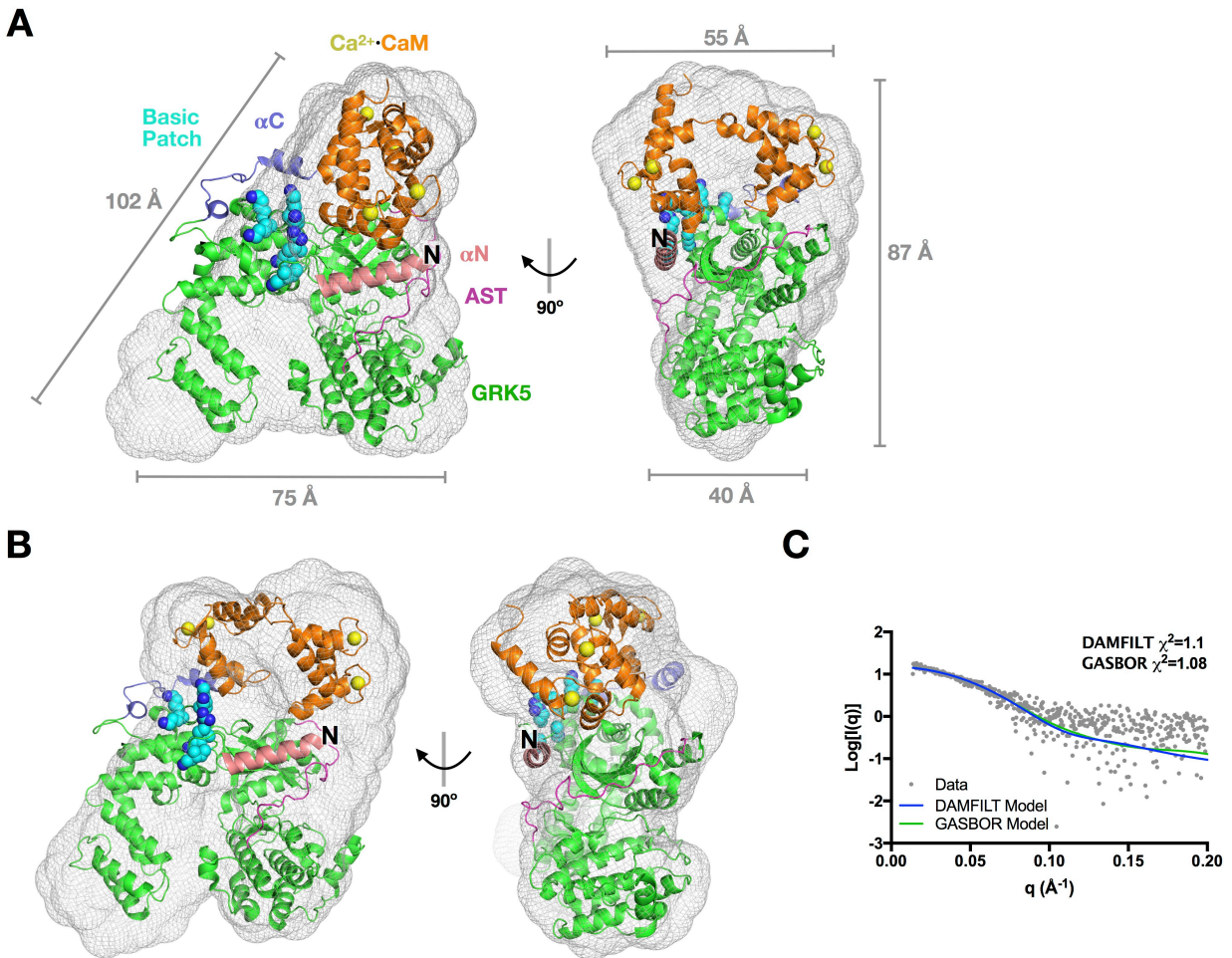
Figure 4.4: SAXS envelopes and modeling. **A)** Manual modeling of GRK5 and Ca^{2+}·CaM into the DAMFILT envelope. **B)** Manual modeling of the Ca2+·CaM–GRK5 complex in the GASBOR envelope. **C)** CRYSOL analysis of the manually modeled complex against the raw data.

4.3.3. Negative stain electron microscopy Ca^{2+}·CaM–GRK5. We next characterized

GRK5 and the Ca^{2+}·CaM–GRK5 complex by negative stain electron microscopy (EM). Particles

of the Ca^{2+}·CaM–GRK5 complex revealed additional protein density corresponding to

Ca^{2+}·CaM (**Figure 2 C**), modeled in similar position to the SAXS experiments, along the surface

spanning the junction between the RH domain (residues 29-181) and N-lobe of the kinase

domain (residues 182-267). To compare the class averages to our SAXS experiments, high-
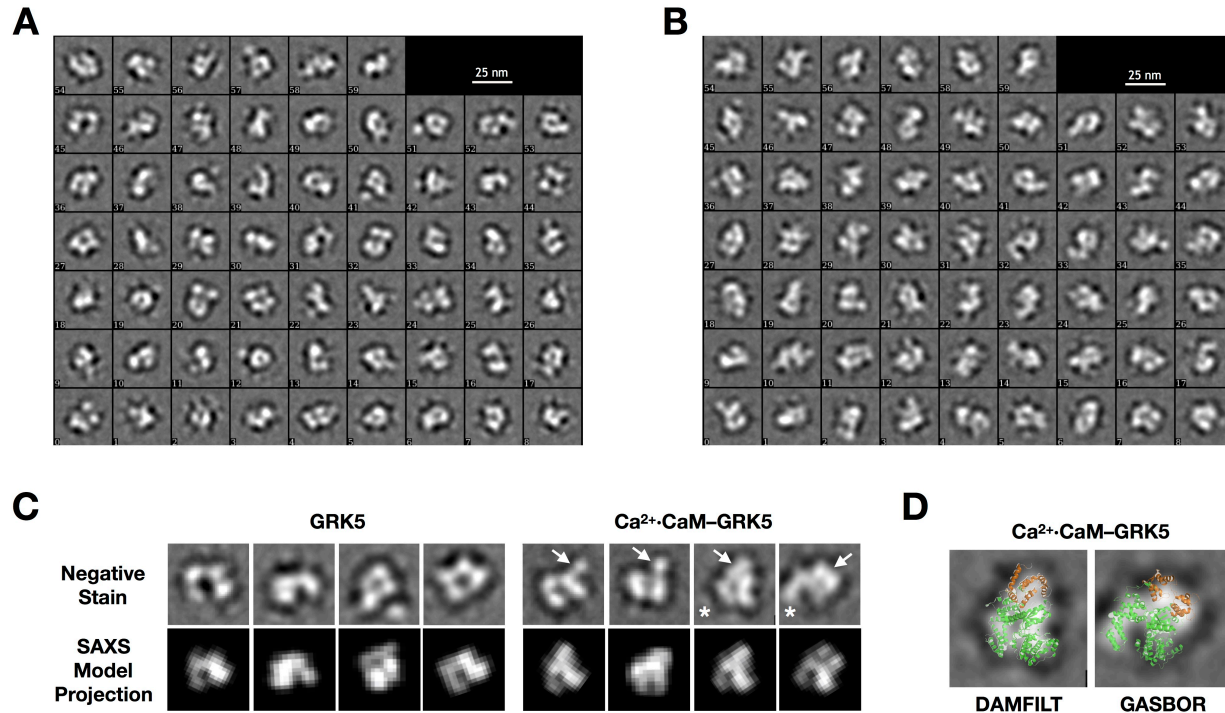
Figure 4.5: Ca^{2+}·CaM–GRK5 negative stain electron microscopy. **A)** Reference-free class averages of GRK5 alone. **B)** Reference-free class averages of the Ca^{2+}·CaM–GRK5 complex. **C)** Selected class averages compared to simulated projections from SAXS models. Density likely corresponding to Ca^{2+}·CaM is indicated by an arrow. **D)** Selected class averages (marked * in panel C) with SAXS models fitting the DAMFILT and GASBOR models overlaid.

resolution models fitting the SAXS envelopes were low-pass filtered and simulated class averages were generated. The SAXS simulated projections align well with those determined by negative stain electron microscopy (**Figure 4.5 C,D**), providing orthogonal confirmation of the architecture of the Ca^{2+}·CaM–GRK5 complex. However, the low resolution of the envelope in either technique prohibits definitive orientation of the two lobes of Ca^{2+}·CaM or their specific contributions to the regulation of GRK5.

  4.3.4. Activation and autophosphorylation of GRK5 by Ca^{2+}·CaM. We sought to determine the effect of Ca^{2+}·CaM binding on the activity of GRK5. As previously reported, Ca^{2+}·CaM inhibits GRK5-mediated receptor phosphorylation while simultaneously promoting

autophosphorylation (**Figure 4.6 A,B**) (Kunapuli *et al.*, 1994). Our structural analysis suggests

inhibition of receptor phosphorylation is likely the result of $Ca^{2+}\cdot CaM$ interacting with regions of

GRK5 critical for both receptor interaction and membrane association. However,

autophosphorylation is not the consequence of membrane dissociation as $Ca^{2+}\cdot CaM$ stimulates

autophosphorylation in the absence of membranes or other substrates (**Figure 4.6 C**).

Interestingly, while $Ca^{2+}\cdot CaM$ inhibits receptor phosphorylation, GRK5 activity toward soluble

substrates is enhanced suggesting that $Ca^{2+}\cdot CaM$ binding stabilizes an active kinase

conformation (**Figure 4.6 D-E**). $Ca^{2+}\cdot CaM$ is even able to promote phosphorylation of myelin

basic protein which is not phosphorylated at all by GRK5 in the absence of $Ca^{2+}\cdot CaM$ **(Figure

4.6 F-G**) further demonstrating the activating effect of $Ca^{2+}\cdot CaM$.

Our structural results are consistent with binding to both the N-terminus and C-terminus

of GRK5 by a single molecule of $Ca^{2+}\cdot CaM$. To dissect the roles of the individual domains of

$Ca^{2+}\cdot CaM$, we studied the effects of its independent N- and C-terminal lobes (residues 1-75 and

78-149, respectively). Both less potently inhibited receptor phosphorylation than full-length

$Ca^{2+}\cdot CaM$, consistent with the fact that interfering with membrane association or receptor

binding would diminish receptor phosphorylation (**Figure 4.6 H**). Interestingly, addition of both

independent lobes of $Ca^{2+}\cdot CaM$ was not sufficient to stimulate autophosphorylation (**Figure 4.6

I**), suggesting that full-length $Ca^{2+}\cdot CaM$ induces an autophosphorylation-prone conformation

mediated by covalently linked lobes, and also that phosphorylation occurs *in cis* and not *in trans*.

This effect is not limited to receptor substrates, as the independent lobes of $Ca^{2+}\cdot CaM$ are also

unable to stimulate autophosphorylation in the presence of soluble substrates (**Figure 4.6 J,K**).
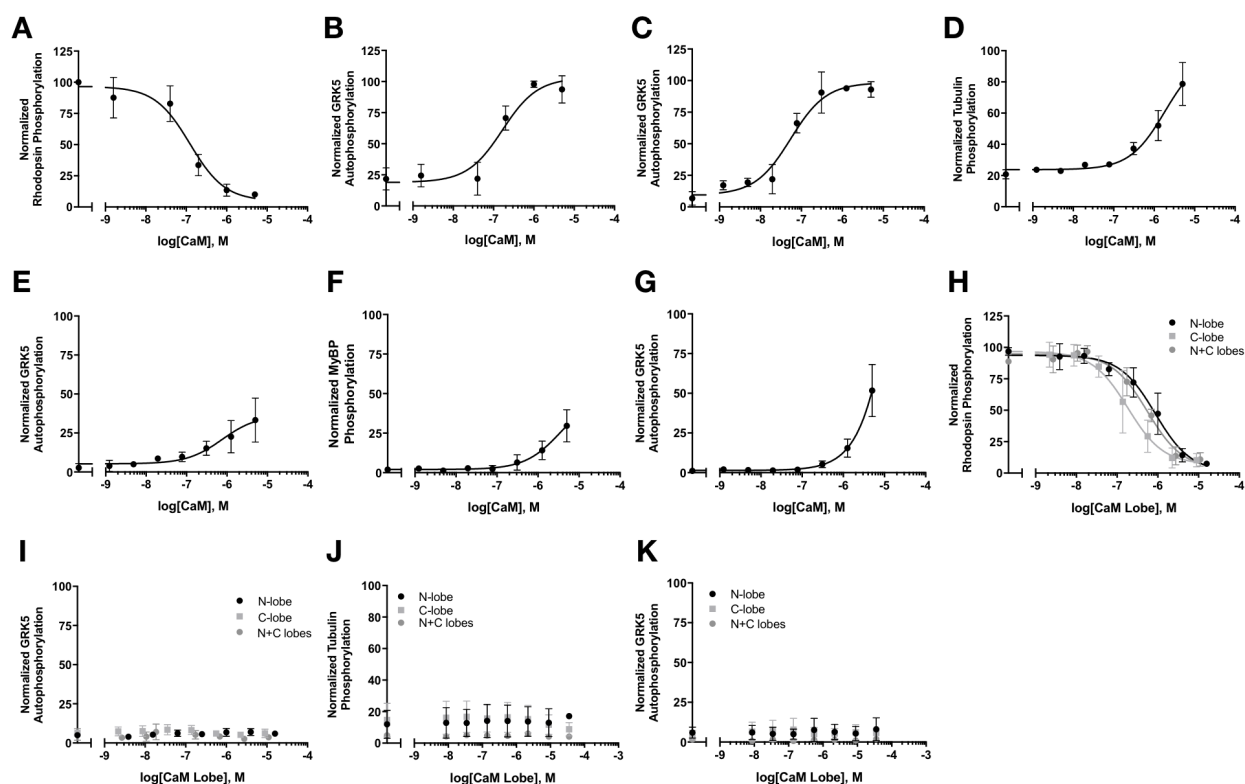
Figure 4.6: Substrate phosphorylation in the presence of calmodulin. **A)** Rhodopsin (5 μM, light activated) phosphorylation and **B)** accompanying GRK5 (50 nM) autophosphorylation in the presence of Ca^{2+}·CaM. **C)** Stimulation of GRK5 (50 nM) autophosphorylation by Ca^{2+}·CaM in the absence of membranes or other substrates. **D)** Tubulin (10 μM) and **E)** corresponding GRK5 autophosphorylation in the presence of Ca^{2+}·CaM. **F)** Phosphorylation of myelin basic protein (7 μM) and **G)** accompanying GRK5 autophosphorylation in the presence of Ca^{2+}·CaM. **H)** Rhodopsin phosphorylation and **I)** accompanying GRK5 autophosphorylation in the presence of the N-lobe, C-lobe, or 1:1 combination of N- and C-lobes of Ca^{2+}·CaM. **J)** Tubulin phosphorylation and **K)** accompanying GRK5 autophosphorylation in the presence of the N-lobe, C-lobe, or 1:1 combination of N- and C-lobes of Ca^{2+}·CaM. All experiments were performed three times and reported as mean ± SD. Data were normalized to either substrate or GRK5 phosphorylation in the absence of small molecule inhibitor and/or Ca^{2+}·CaM (100%) and an SDS-PAGE background (0%) measurement.

4.3.5. Binding analysis of malbrancheamide with Ca²⁺·CaM and its effects on the

Ca²⁺·CaM–GRK5 interaction. To discern which lobe of CaM is involved in binding each GRK5

binding site, we turned to malbrancheamide, a halogenated fungal indole alkaloid that

antagonizes Ca²⁺·CaM (**Figure 4.7 A**) (Figueroa *et al.*, 2011) and is predicted through docking

studies to bind to the C-terminal lobe (González-Andrade *et al.*, 2016). However, prior binding

experiments suggested a 2:1 malbrancheamide to Ca²⁺·CaM stoichiometry (Figueroa *et al.,*

2011). We first used isothermal titration calorimetry (ITC) to confirm the binding affinity and

stoichiometry of malbrancheamide, provided by Amy Fraley of the Sherman lab, for Ca²⁺·CaM.

The affinity (K_d) of malbrancheamide was determined to be 5.2 ± 0.8 µM, consistent with prior

reports (Figueroa *et al.*, 2011), and binds Ca²⁺·CaM with a 1:1 stoichiometry (**Figure 4.7 B,C**).

The congener isomalbrancheamide D with a Br atom in place of the C-9 Cl (Fraley *et al.*, 2017)

was also assessed by ITC and displayed an affinity of 1.8 ± 0.3 µM and a stoichiometry of 1:1

(**Figure 4.7 B,C**).

We next determined the crystal structure of the Ca²⁺·CaM·malbrancheamide complex to

1.96 Å spacings (**Figure 4.8 A-C and Table 4.2**), wherein a single malbrancheamide molecule is

observed bound with its dichlorinated indole buried in the hydrophobic pocket of the C-lobe of

Ca²⁺·CaM (**Figure 4.8 B,C**). Malbrancheamide forms a pair of hydrogen bonds with a

neighboring molecule in a crystallographic symmetry mate (**Figure 4.8 D**). The C-8 chlorine

packs against Phe93 while the indole is positioned between Leu106, Met125, and Met145.

Malbrancheamide buries approximately 250 Å² of surface area in the hydrophobic pocket (via

PISA server, Krissinel and Henrick, 2007), consistent with ligands of similar affinities

(Waldschmidt *et al*., 2016). The observed Ca²⁺·CaM conformation is rare and only reported one
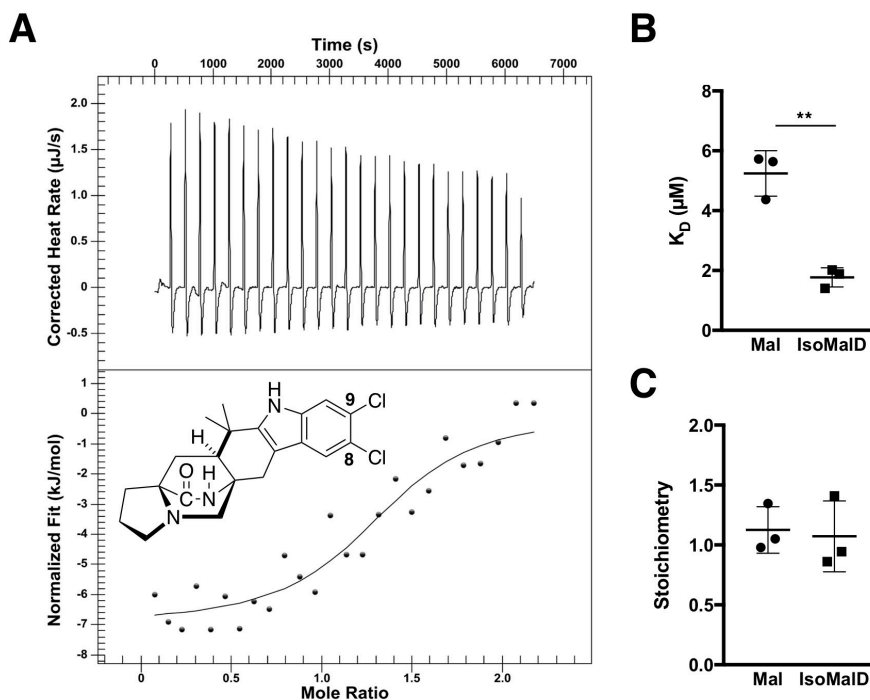
Figure 4.7: Binding analysis of malbrancheamide to $Ca^{2+} \cdot CaM$. **A)** Representative ITC binding curve for malbrancheamide (Mal) and $Ca^{2+} \cdot CaM$ and chemical structure of malbrancheamide (inset). **B)** Binding affinity and **C)** stoichiometry. Isomalbrancheamide D (IsoMalD) contains a bromine atom in place of the C-9 chlorine. Data represented as mean ± SD (n=3). Statistical significance determined by Student's two-tailed T-test (**p<0.01).

other time our of several hundred $Ca^{2+} \cdot CaM$ structures (Kumar *et al.*, 2013). In this open

conformation, the canonical binding site on the N-lobe of $Ca^{2+} \cdot CaM$ is free to interact with other

substrates while the C-lobe is bound to malbrancheamide.

Addition of malbrancheamide to phosphorylation reactions containing $Ca^{2+} \cdot CaM$–GRK5

did not recover rhodopsin phosphorylation, but inhibited GRK5 autophosphorylation (**Figure 4.9**

A-D). Malbrancheamide also had no effect on the stimulation of phosphorylation of soluble

substrates mediated by $Ca^{2+} \cdot CaM$ (**Figure 4.9 E**), but similarly inhibited stimulation of

autophosphorylation (**Figure 4.9 F**). This results indicates that the C-lobe of $Ca^{2+} \cdot CaM$ is

involved in phosphorylation of the C-terminus of GRK5, and that the N-lobe is responsible for

Table 4.2: Crystallographic Data Collection and Refinement Statistics for the Ca^{2+}·CaM·Mal Complex

Wavelength (Å)	1.03315
Resolution range	35.42 - 1.96 (2.03 - 1.96)*
Space group	$C\,2\,2\,2_1$
Unit cell constants (Å, °)	49.1 56.9 116.8 90 90 90
Total reflections	158616 (16218)
Unique reflections	12096 (1184)
Multiplicity	13.1 (13.7)
Completeness (%)	99.8 (99.8)
Mean I/σ(I)	7.47 (1.73)
Wilson B-factor	29.7
R$_{meas}$	0.200 (0.831)
CC$_{1/2}$	0.995 (0.944)
Reflections used in refinement	12080 (1181)
Reflections used for R$_{free}$	1207 (118)
R$_{work}$	0.216 (0.366)
R$_{free}$	0.243 (0.386)
Number Non-hydrogen atoms	1221
Protein	1127
Ligand	32
Solvent	62
RMSD bonds (Å)	0.002
RMSD angles (°)	0.41
Ramachandran favored (%)	99.3
Ramachandran allowed (%)	0.7
Ramachandran outliers (%)	0
Rotamer outliers (%)	0.8
Clashscore	3.6
Average B-factor	54.0
Protein	53.7
Ligand	85.4
Solvent	43.3
PDB Entry	TBD

*Statistics for the highest-resolution shell are shown in parentheses

stimulation of GPCR and soluble substrates, likely via direct interactions with the small lobe of the kinase domain.

4.3.6. Perturbation of Ca^{2+}·CaM lobe interactions with terminal regions of GRK5. In another approach, peptides spanning the known Ca^{2+}·CaM binding sites on GRK5, αN (residues 2-31) and αC (residues 546-565), were evaluated for their ability to disrupt regulation of GRK5 by Ca^{2+}·CaM. Titration of either peptide inhibited autophosphorylation (**Figure 4.9 H,J**). However, whereas the addition of the αN peptide recovered receptor phosphorylation, addition of the αC peptide did not, mimicking the effect observed upon addition of malbrancheamide (**Figure 4.9 G,I**). Neither peptide affected soluble substrate phosphorylation (**Figure 4.9 I**), although similar inhibition of autophosphorylation was observed (**Figure 4.9 J**). Thus, the C-terminus of GRK5 likely binds the C-lobe of Ca^{2+}·CaM in the same manner as malbrancheamide.
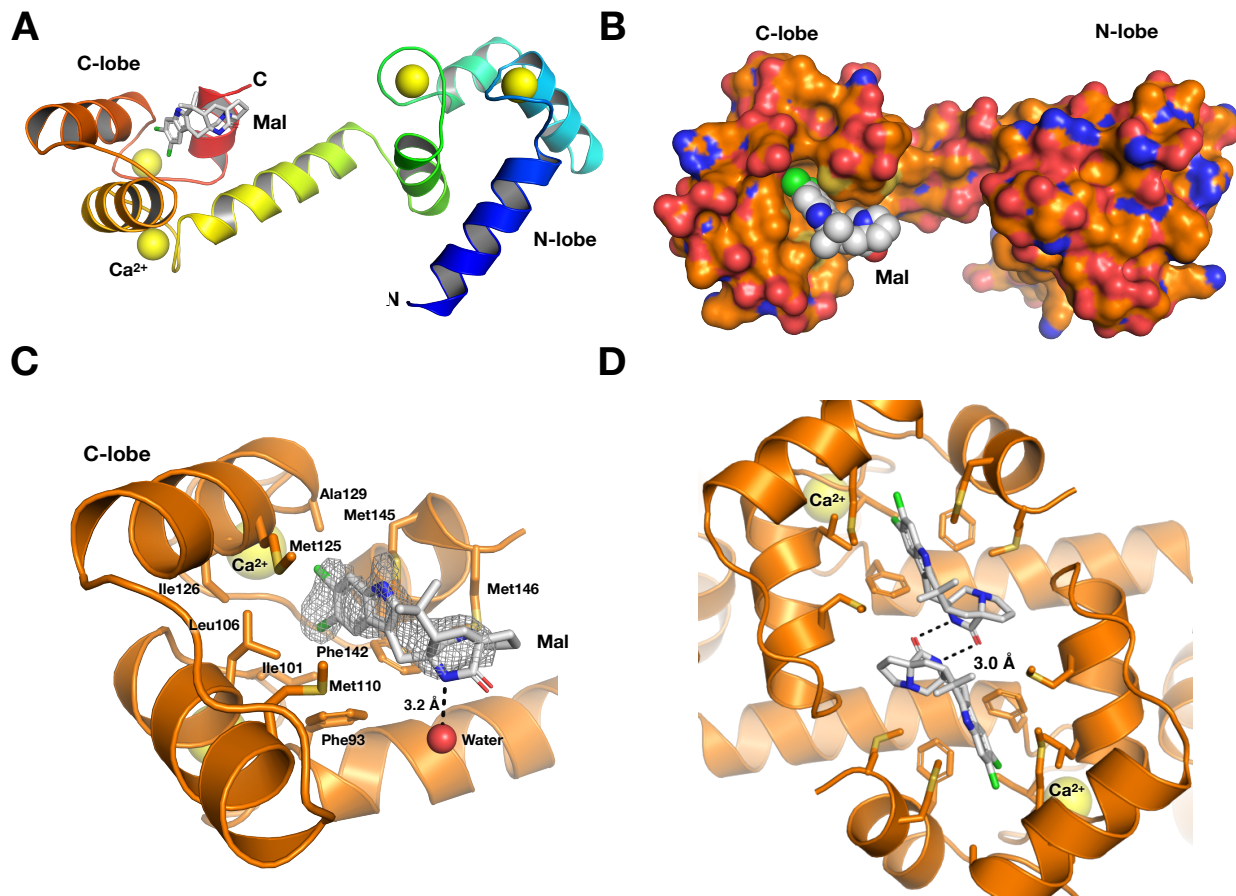
Figure 4.8: Ca^{2+}·CaM·malbrancheamide crystal structure. **A)** Rainbow ribbon representation of the Ca^{2+}·CaM·Mal structure. Ca^{2+} are shown as yellow spheres. **B)** Surface representation of Ca^{2+}·CaM with malbrancheamide shown in spheres bound to the C-lobe. **C)** C-lobe hydrophobic pocket with malbrancheamide bound. Black dotted line represents a hydrogen bond with a water molecule. Ca^{2+} is shown as a yellow sphere. Mesh represents $|2F_o| - |F_c|$ electron density contoured at 1 σ. **D)** Interactions between malbrancheamide molecules in crystallographic symmetry mates.
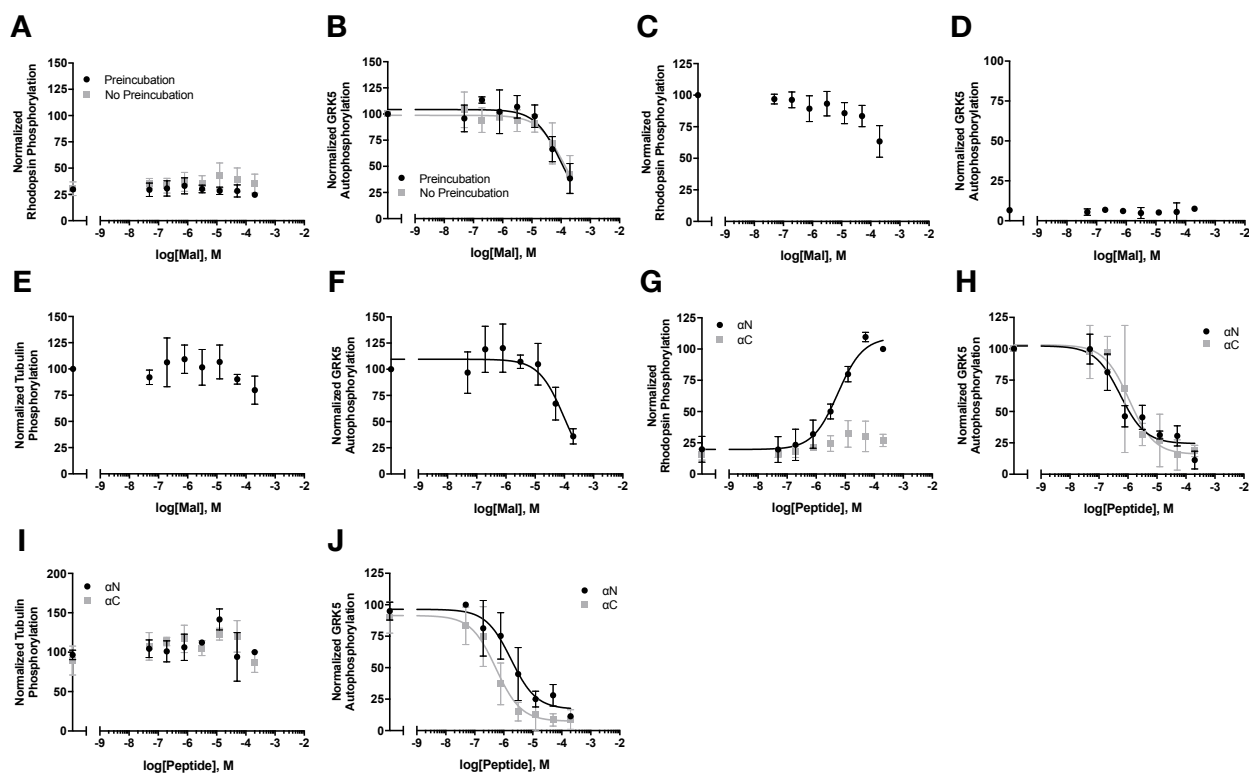
Figure 4.9: Effects of malbrancheamide and GRK5 peptides on Ca²⁺·CaM modulation of GRK5 activity. **A)** Rhodopsin (5 µM, light activated) phosphorylation and **B)** accompanying GRK5 (50 nM) autophosphorylation in the presence of 500 nM Ca²⁺·CaM and increasing concentrations of malbrancheamide. In these assays, Ca²⁺·CaM was either preincubated with malbrancheamide or with GRK5prior to the addition of malbrancheamide ("no preincubation"). **C)** Effect of malbrancheamide on rhodopsin phosphorylation and **D)** autophosphorylation in the absence of Ca²⁺·CaM. **E)** Tubulin (5 µM) phosphorylation and **F)** accompanying GRK5 autophosphorylation in the presence of 500 nM Ca²⁺·CaM and varying concentrations of malbrancheamide. **G)** Rhodopsin phosphorylation and **H)** accompanying GRK5 autophosphorylation in the presence of 500 nM Ca²⁺·CaM and varying concentrations of GRK5 αN or αC peptides. **I)** Tubulin phosphorylation and **J)** accompanying GRK5 autophosphorylation in the presence of 500 nM Ca²⁺·CaM and varying concentrations of GRK5 αN or αC peptides. All experiments were performed three times and reported as mean ± SD. Data were normalized to either substrate or GRK5 phosphorylation in the absence of small molecule inhibitor and/or Ca²⁺·CaM (100%) and an SDS-PAGE background (0%) measurement.

4.4. Discussion

The role of GRK5 in heart failure and cardiac hypertrophy has spurred interest in both therapeutic development and the underlying molecular mechanisms of disease. Several recent studies have shed light on the role of GRK5 regulation by Ca^{2+}·CaM at the cellular and physiological levels (Martini *et al.*, 2008; Gold *et al.*, 2013). However, the molecular basis of the interaction remains understudied. Prior pulldown assays showed that Ca^{2+}·CaM affinity toward GRK5 was mediated by contacts with the N-terminal helix (residues 1-17), the basic phospholipid binding patch (residues 20-39), and the C-terminal amphipathic helix (residues 552-561) (Pronin *et al.*, 1997; Levay *et al.*, 1998). Two primary models for the Ca^{2+}·CaM–GRK5 complex have been proposed, including one in which two Ca^{2+}·CaM molecules bind distinct sites on GRK5 and one in which a single Ca^{2+}·CaM molecule binds multiple elements simultaneously. Here, I present light scattering, SAXS, and negative stain EM data that reveal a single Ca^{2+}·CaM binds in a manner that is in agreement with the latter model (**Figure 4.10**).

The architecture of the complex reveals Ca^{2+}·CaM binding near and likely interacting with the αN and αC helices simultaneously. Indeed, numerous structures of Ca^{2+}·CaM bound to two helices have been reported in which Ca^{2+}·CaM the pair of helices are positioned between the lobes containing Ca^{2+}-bound EF-hands (Tidow and Nissen, 2013). The αN helix has been proposed in some models to dock into the hydrophobic core of activated GPCRs and is well known to be critical for receptor recognition and phosphorylation (Pao *et al.*, 2009; Huang and Tesmer, 2011). Thus, Ca^{2+}·CaM binding to the αN partially explains the inability of GRK5 to efficiently phosphorylate receptor substrates. Furthermore, the basic patch on GRK5 (residues 20-39) that interacts with PIP_2 to aid in membrane localization and allosteric activation of the
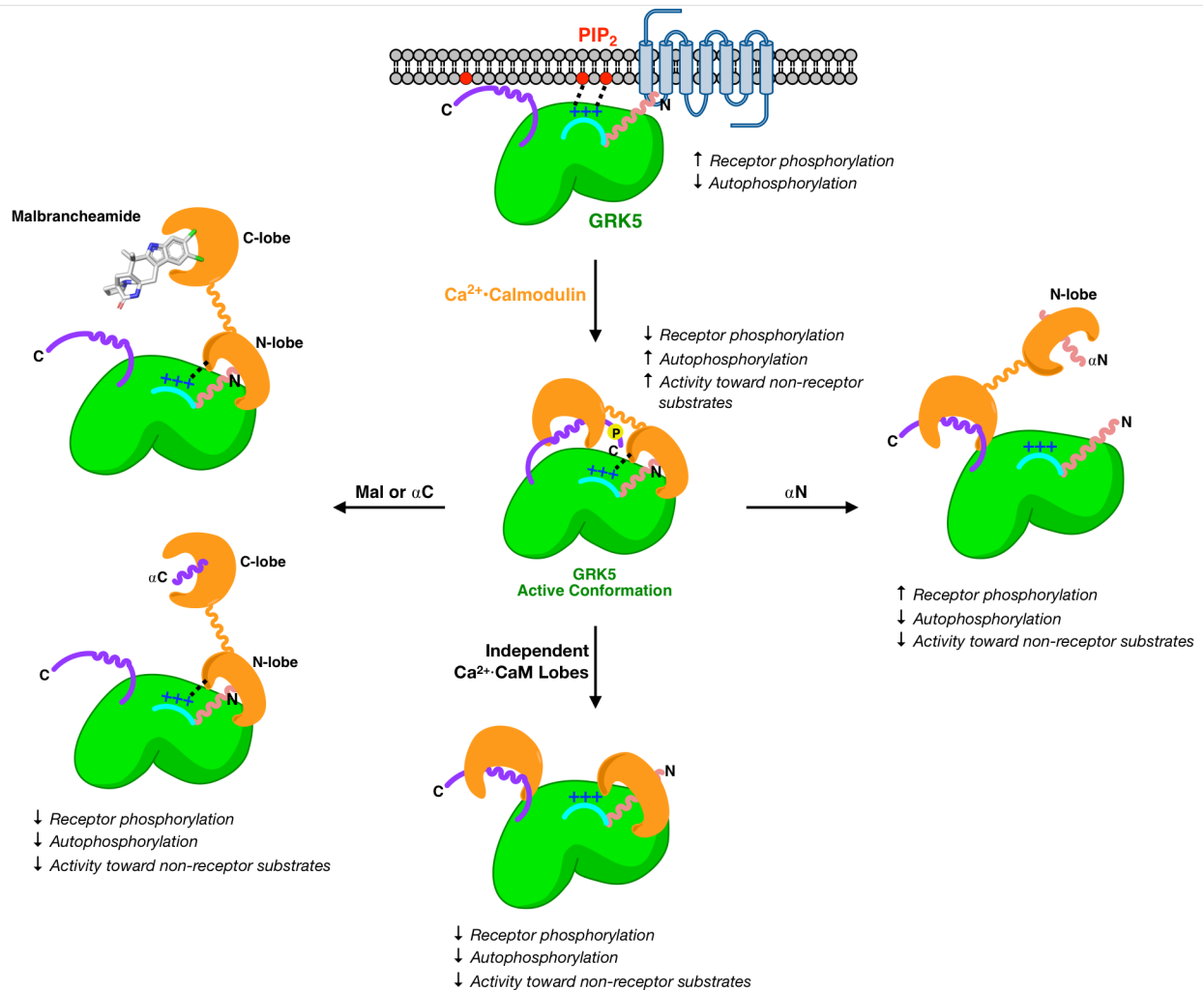
Figure 4.10: Proposed model of the regulation of GRK5 by Ca^{2+}·CaM. Features critical for receptor docking and membrane association are sequestered by Ca^{2+}·CaM but also induce an active conformation of the kinase. However, addition of the two independent lobes Ca^{2+}·CaM does not promote an activated state of GRK5. The addition of αN and αC peptides or malbrancheamide (Mal) are able to relieve various aspects of regulation through differential binding to Ca^{2+}·CaM.

kinase enhances $Ca^{2+} \cdot CaM$ affinity when added to peptides of the αN helix (Levay *et al.*, 1998). In our model, this patch is adjacent to multiple acidic residues on $Ca^{2+} \cdot CaM$ and would project basic residues toward the acidic surface of $Ca^{2+} \cdot CaM$ which would engage in favorable electrostatic interactions and sterically occlude PIP_2 binding (**Figure 4.11**). Because GRK5 is not lipid modified like other GRK4 subfamily members, its C-terminal amphipathic helix significantly contributes to membrane association. Sequestration of the αC helix by $Ca^{2+} \cdot CaM$ as suggested by our model would lead to impaired membrane association or altered orientation along the membrane surface further disrupting interactions with GPCRs.[5] Together, this architecture is consistent with a kinase that would have difficulty interacting with membranes and receptor substrates when bound to $Ca^{2+} \cdot CaM$.

Substrates of $Ca^{2+} \cdot CaM$ often contain positively charged amphipathic helices with bulky hydrophobic side chains that anchor in the hydrophobic pockets of each lobe of $Ca^{2+} \cdot CaM$ (Bhattacharya *et al.*, 2004; Kursula, 2014). The terminal helices and basic patch of GRK5 resemble canonical $Ca^{2+} \cdot CaM$ substrates such as the well characterized myristoylated alanine-rich protein kinase C substrate (MARCKS) (Pronin *et al.*, 1997; Arbuzova *et al.*, 1998; Yamauchi *et al.*, 2003). With only minor manual movement of the terminal regions of GRK5 in our SAXS models, the αN and αC helices can both be placed in a canonical $Ca^{2+} \cdot CaM$ binding mode with potential hydrophobic anchoring residues positioned near the hydrophobic pockets of $Ca^{2+} \cdot CaM$ (**Figure 4.11**).

Interestingly, although $Ca^{2+} \cdot CaM$ potently inhibits receptor phosphorylation, the activity of GRK5 toward soluble substrates is enhanced. It has been previously reported that $Ca^{2+} \cdot CaM$ stimulates phosphorylation of certain cytosolic proteins such as synucleins (Pronin *et al.*, 2000),
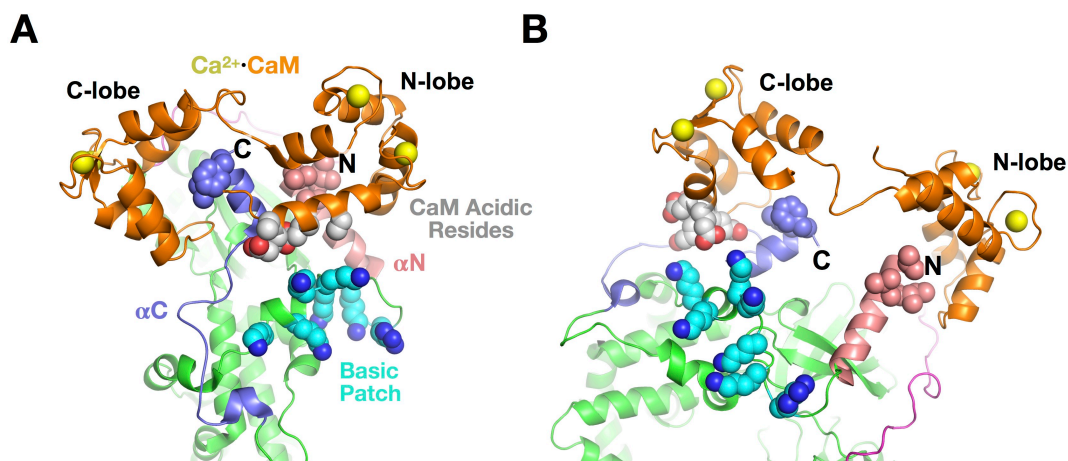
Figure 4.11: Potential docking residues in the GRK5 termini. Modeled termini for the **A)** DAMFILT and **B)** GASBOR SAXS models. Hydrophobic residues Leu3, Ile6, Val7, Leu554, and Phe555 are shown in spheres positioned near canonical hydrophobic binding pockets on $Ca^{2+} \cdot CaM$.

but this appears to apply to all soluble substrates suggesting that $Ca^{2+} \cdot CaM$ binding stabilizes an activated state of GRK5. As suggested by the GRK6·sangivamycin crystal structure (Boguth *et al.*, 2010), the activated state of GRKs is stabilized by a network of contacts between the αN helix, AST loop, and RH domains (Lodowski, Tesmer, and Benovic, 2006; Pao *et al.*, 2009; Huang *et al.*, 2009; Boguth *et al.*, 2010; Huang *et al.*, 2011). Because one lobe of $Ca^{2+} \cdot CaM$ binds near these features based on our SAXS and EM data, stabilization of this interaction network likely explains the increase in GRK5 activity towards its soluble substrates. Addition of the isolated lobes of $Ca^{2+} \cdot CaM$, however, did not similarly activate kinase activity at any concentration tested, indicating that full-length $Ca^{2+} \cdot CaM$ is required for stabilizing this active conformation of GRK5.

Unlike other members of the AGC family of protein kinases, GRKs do not require activation loop autophosphorylation for efficient catalysis. However, GRK5 undergoes PIP_2-

stimulated autophosphorylation at Ser484 and Thr485 in the AST loop (Kunapuli *et al.*, 1994). Ca^{2+}·CaM-stimulated autophosphorylation has been mapped to non-canonical residues in the extreme C-terminus of GRK5 (residues 579-590) that, similarly to phosphorylation by protein kinase C (PKC), further reduces the ability of GRK5 to associate with membranes and may represent a mechanism to prolong GRK5 inhibition after Ca^{2+}·CaM has dissociated (Pronin and Benovic, 1997; Levay *et al.*, 1998; Penn *et al.*, 2000). Cleavage of the helix connecting the two lobes of Ca^{2+}·CaM abolished Ca^{2+}·CaM-stimulated autophosphorylation, suggesting that intact Ca^{2+}·CaM positions the terminal elements of GRK5 in a specific conformation that allows for robust *cis*-autophosphorylation. A likely mechanism for this "repositioning" may simply be loss of membrane shielding of the C-terminal region of the kinase via the binding of Ca^{2+}·CaM, which would free this disordered region to instead be acted on by the active site of the kinase domain, but it is also possible that Ca^{2+}·CaM redirects the path of the C-terminus towards the active site. In addition to a shorter C-tail, the C-terminus of other GRK4 subfamily members is often palmitoylated (Stoffel *et al.*, 1994; Premont *et al.*, 1996; Sallese *et al.*, 1997; Loudon and Benovic, 1997) and may remain membrane anchored when bound to Ca^{2+}·CaM, explaining why GRK4 and 6 do not display Ca^{2+}·CaM-induced autophosphorylation.

Despite a lack of high-resolution structures, our model, in combination with prior biochemical studies, allude to mechanisms of selectivity. The αN helix is bound to one lobe of Ca^{2+}·CaM in our model is variable across GRKs but is highly conserved within the GRK4 subfamily, which are most potently inhibited by Ca^{2+}·CaM. Likewise, the αC helix and basic phospholipid binding patch are absent in the GRK1 and GRK2 subfamilies (**Figure 1.3 B)**. Thus, these evolutionary differences may explain the preference for GRK4 subfamily members.

However, while GRK1 is inhibited by Ca^{2+}·CaM *in vitro*, the primary regulator in cells is the related neuronal Ca^{2+}-sensing protein recoverin further supporting evolutionary divergence between GRK subfamilies (Kawamura *et al.*, 1993; Levay *et al.*, 1998; Torisawa *et al.*, 2008; Komolov *et al.*, 2009). The potency of Ca^{2+}·CaM for GRK4 subfamily members directly correlates with the number of basic residues in this patch which interacts with acidic residues on Ca^{2+}·CaM in our model. Despite similarities in their αC helices, GRK4 and 6 tend to be lipid modified which may limit accessibility of this region for binding to one lobe of Ca^{2+}·CaM.

Determination of the roles of the individual lobes of Ca^{2+}·CaM were aided by the natural product malbrancheamide, which we showed to stabilize an unusual conformation of Ca^{2+}·CaM and bind solely to the C-lobe. This implies that addition of the compound would mimic the action of a GRK5 that binds to the C-lobe. Indeed, the addition of malbrancheamide or the αC peptide inhibited kinase autophosphorylation but did not affect receptor phosphorylation. Therefore, the C-lobe of Ca^{2+}·CaM interacts with the C-terminus of GRK5 to dissociate the kinase from membranes, whereas the N-lobe interacts with the αN helix to interfere with receptor phosphorylation. It has been previously noted that rhodopsin phosphorylation is similarly inhibited by an antibody that recognize epitopes in the N-terminus of GRK1 without affecting soluble substrate phosphorylation. (Palczewski *et al.*, 1993). While not tested, the increased binding affinity of isomalbrancheamide D may more potently inhibit Ca^{2+}·CaM interactions with GRK5.

Extraction of GRK5 from the plasma membrane by Ca^{2+}·CaM is thought to allow the nuclear localization sequence located in the large lobe of the kinase (Johnson *et al.*, 2004) to promote nuclear translocation and pathological gene activation. The fact that Ca^{2+}·CaM activates

GRK5 against soluble targets would augment this ability. Pharmacological disruption of the interaction of the C lobe of $Ca^{2+} \cdot CaM$ with GRK5 may represent a therapeutic strategy for attenuating $Ca^{2+} \cdot CaM$–GRK5-induced cardiac hypertrophy without attenuating the ability of $Ca^{2+} \cdot CaM$ to repress receptor phosphorylation and hence downregulation (**Figure 4.12**). Several FDA-approved antipsychotics are known to bind $Ca^{2+} \cdot CaM$, though often with low affinity and with various side-effects due to inhibition of other targets (Feldkamp *et al.*, 2015; González-Andrade *et al.*, 2016). Furthermore, $Ca^{2+} \cdot CaM$ inhibitors often assume multiple binding poses, as is the case with the antipsychotic drug trifluoperazine which has been observed to bind in various orientations in either or both lobes of $Ca^{2+} \cdot CaM$ (Vandonselaar *et al.*, 1994; Feldkamp *et al.*, 2015; González-Andrade *et al.*, 2016; Cook *et al.*, 1994).

Our elucidation of the binding mode of malbrancheamide at the C-terminal lobe of $Ca^{2+} \cdot CaM$ and its successful application in probing the $Ca^{2+} \cdot CaM$–GRK5 interaction highlights its potential as both a chemical probe and lead molecule for rational design. Milligram quantities of malbrancheamide can be readily obtained from small-scale fungal cultures (Fraley *et al.*, 2017). The elucidation of the biosynthetic pathway and more recent structural studies of the late-stage halogenase have enabled the generation of novel analogs through chemoenzymatic synthesis using engineered enzymes (Fraley *et al.*, 2017). One such analog, isomalbrancheamide D bearing a C-9 bromine in addition to C-8 chlorine, displays significantly higher affinity. Analysis of the $Ca^{2+} \cdot CaM \cdot Mal$ structure reveals additional space in the binding pocket near the C-9 position which the bulkier bromine may better occupy. However, the majority of reported malbrancheamide analogs and structurally similar natural products have yet to be evaluated for their ability to modulate the $Ca^{2+} \cdot CaM$–GRK5 interaction. Nonetheless, recent studies on
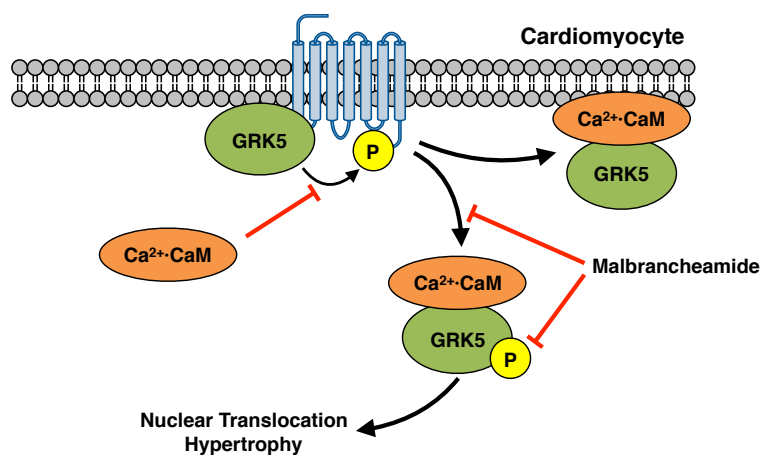
Figure 4.12: Scheme depicting the mechanism by which malbrancheamide may prevent nuclear translocation by releasing the C-terminus of GRK5 from $Ca^{2+} \cdot CaM$.

manipulating the biosynthetic pathways for malbrancheamide and structurally related natural products, along with our co-crystal structure and inhibition data, provide a starting point for the development of new products for use in selectively blocking C-lobe interactions of $Ca^{2+} \cdot CaM$.

Chapter 5: Recombinant Production of Human GRK5 in a Bacterial System

5.1. Introduction

As highlighted in Chapters 1 and 4, GRK5 is an important kinase in the progression of cardiovascular pathologies and an attractive therapeutic target (Métayé *et al.*, 2005; Hullmann *et al.*, 2014). Thus, efficient expression and purification of GRK5 is needed to supply high-quality protein for structural and pharmacological studies. GRK5 is almost exclusively recombinantly purified from insect cells using engineered baculovirus (see *4.2.2*) with small quantities obtained through mammalian cell expression systems. Both expression systems are more expensive and, in the case of insect cells, time consuming than recombinant expression in standard bacterial systems. Kinases in general are not often purified from bacterial systems due to cytotoxicity, resulting from phosphorylation of intracellular substrates, or misfolding. However, considerable success has been achieved using truncated or catalytically inactive kinases (Shrestha *et al.*, 2012), though such variants have limited use in biochemical assays. To date, there is only one report of a GRK being expressed and purified from a bacterial system. Gan *et al.* reported purification of soluble human GRK2, but the result was not reproducible in our lab.

To facilitate future studies of GRK5, we sought to develop a method for the rapid and cost-effective purification of full-length, human GRK5 from *E. coli*. In addition to cost and time savings, expression in bacterial systems affords other advantages. The production of isotopically labeled proteins for nuclear magnetic resonance (NMR) studies is significantly easier in bacterial expression systems. Additionally, the production of numerous protein variants in bacteria is

streamlined as time-consuming recombinant baculovirus does not need to be produced for each variant.

Previous attempts to purify GRK5 from bacterial systems yielded insoluble protein, even in the presence of solubilizing tags such as MBP. A GRK5 construct and purification protocol was devised to produce full-length human GRK5 in *E. coli* with comparable yields to insect expression systems. Characterization of the bacterially expressed kinase revealed extensive autophosphorylation that leads to a slight reduction in V_{max} compared to GRK5 purified from insect cells which is restored upon mutation of a single phosphorylation site.

5.2. Materials and methods

5.2.1. GRK5 cloning, expression, and purification. The human GRK5 gene was amplified with the addition of a C-terminal Val-Asp spacer directly followed by a hexahistidine tag (**Figure 5.1**, see peptide sequence in **Figure 5.5 F**). 5' NdeI and 3' EcoRI restriction sites were also introduced to the gene fragment via PCR. The bacterial expression vector pMalC$_2$H$_{10}$T was digested with NdeI and
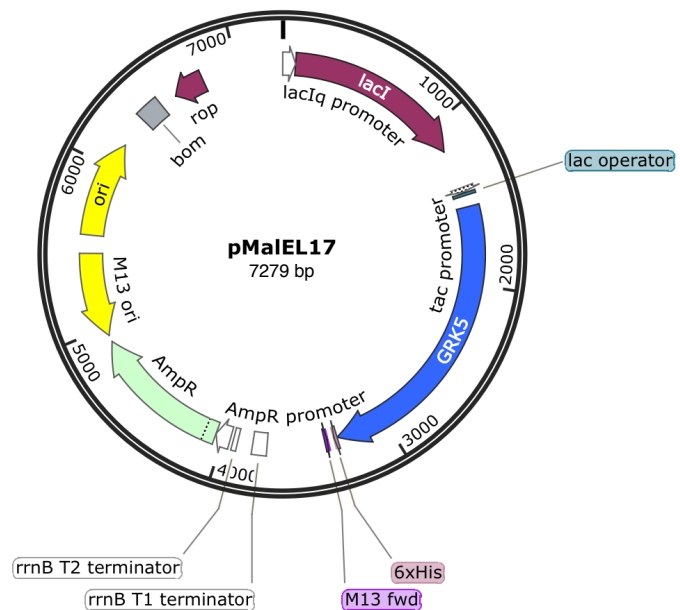
Figure 5.1: Vector map of human GRK5 in a modified pMalC2H10T (pMalEL17). Cloning was performed with the assistance of Emily Labudde (University of Michigan).

EcoRI to remove the MBP-polyhistidine-TEV features and the GRK5 gene ligated into the modified vector to produce plasmid pMalEL17.

5.2.2. GRK5 protein expression and purification. GRK5 was expressed in BL21 Rosetta

cells containing the pRARE plasmid encoding rare tRNAs. Cells were grown in TB at 37 ºC until

OD_{600} of ~0.6, cooled to 18 ºC, induced with 0.2 mM IPTG at OD_{600} = 1.0-1.2 , and grown

overnight at 18 ºC. Cells were pelleted and resuspended in lysis buffer containing 20 mM

HEPES pH 8.0, 200 mM NaCl, 40 mM imidazole, 5 mM $MgCl_2$, 5 mM $CaCl_2$, 1 mM DTT,

leupeptin, lima bean trypsin protease inhibitor, and 2 µg mL^{-1} DNaseI and lysed with a

EmulsiFlex-C3 cell homogenizer. Alternatively, DNaseI can be replaced with 0.02% (v/v) Triton-

X100 but should be omitted from later wash and elution buffers. Lysate was incubated on ice for

30 m to allow for digestion of DNA prior to ultracentrifugation at >200,000xg for 1 h. The

resulting supernatant was glass filtered, flowed through Ni-NTA resin, washed with lysis buffer,

and eluted with lysis buffer containing and additional 200 mM imidazole. Eluted GRK5 was

further purified by cation exchange chromatography with a HiTrap S column and eluted with a

gradient of 0.0-1.0 M NaCl at pH 8.0. Anion exchange can also be used to purify GRK5 but

removal of the lower band of truncated kinase is not as easily achieved. Eluted GRK5 was

subsequently purified via SEC in a buffer containing 20 mM HEPES pH 8.0, 200 mM NaCl, and

1 mM DTT with an analytical S200 column. GRK5 concentrations were determined by

absorbance at 280 nm using the calculated molecular weight and molar extinction coefficient

from the primary sequence and flash frozen in liquid nitrogen. Typical yields of ≥95% purity

GRK5 by SDS-PAGE from *E. coli*. were 2 mg L^{-1}.

5.2.3. Western blotting. Protein samples were separated via SDS-PAGE and transferred

to nicrocellulose membranes overnight. The membrane was blocked with 5% (w/v) bovine serum

albumin (BSA) in Tris-buffered saline Tween (TBST, 50 mM Tris pH 7.4, 150 mM NaCl, 0.1%

105

(v/v) Tween 20), incubated overnight with primary antibody (anti-hexahistidine [H3, Santa Cruz Biotechnology] or anti-N-terminus of GRK5 [LS-A3470-50, LifeSpan Biosciences]), washed with TBST, incubated with appropriate secondary antibody conjugated to horseradish peroxidase, washed with TBST, and protein detected via chemiluminescence on film.

5.2.4. Mass spectrometry and phosphosite mapping. Intact protein mass spectrometry (MS) was performed on an Agilent quadrupole time-of-flight tandem mass spectrometer (QTOF-MS/MS) with an 1-3 μL injection volume of GRK5 at 1 mg mL^{-1} in buffer containing 1% (v/v) formic acid. Protein was desalted on a C18 chromatography column prior to mass analysis with positive electrospray ionization (ESI$^+$). Phosphosite mapping was performed through the Purdue University Proteomics Facility. Briefly, purified GRK5 was digested with trypsin, the fragments analyzed via high-resolution MS without TiO_2 enrichment, and phosphorylation sites identified through peptide ionization patterns compared to the nonphosphorylated primary amino acid sequence.

5.2.5. Kinetic analysis. Steady-state kinetic parameters were determined as previously described (Yao *et al.*, 2017). Briefly, 50 nM GRK5 expressed and purified from insect cells or *E. coli* and 5 μM bovine rhodopsin in native membranes were combined in assay buffer containing 20 mM HEPES, 10 mM $MgCl_2$, and 1 mM DTT. Reactions were initiated with 2-200 μM ATP spiked with [γ-^{32}P]-ATP and allowed to proceed for 5 min at room temperature prior to separation by SDS-PAGE and image analysis on phosphor screens. Standard curves for quantification were prepared using a serial dilution of [γ-^{32}P]-ATP given the initial specific activity and number of half-lives passed. The maximum reaction velocity (V_{max}) and apparent

Michaelis constant (K_m) were determined via GraphPad Prism using a classic Michaelis-Menten plot.

   5.2.6. Crystallization. GRK5 from *E. coli* at 9-11 mg mL^{-1} was incubated for 1 hr on ice with 2 mM ATP, 5 mM MgCl$_2$ after which sitting-drop sparse-matrix screens were set with drops containing 0.5 µL protein and 0.5 µL well solution. Screens were incubated at either 4 or 20 ºC. After 1 wk at 4 ºC, rod-like crystals ranging from 25-250 µm in length appeared in Hampton Research Index HT E8 (0.2 M KCl, 0.05 M HEPES pH 7.5, 35% v/v pentaerythritol propoxylate (5/4 PO/OH)), C4 (35% v/v tacsimate pH 7.0), C9 (1.1 M sodium malonate pH 7.0, 0.1 M HEPES pH 7.0, 0.5% v/v Jeffamine ED-2001 pH 7.0), and Qiagen ProComplex G10 (1.6 M Na/ KPO$_4$ pH 6.5). Crystals from Index C4 were reproduced in hanging-drop form after 1 mo at 4 ºC in 0.1 M Bis-Tris pH 5.8 and 35% (v/v) tacsimate. Crystals from ProComplex G10 were reproduced at 20 ºC in hanging-drop form under identical conditions. Diffraction data were collected at either LS-CAT or GMCA beamlines (Advanced Photon Source, Argonne National Lab).

5.3. Results

   5.3.1. Optimization of expression and purification in *E. coli*. Human GRK5 was cloned with a C-terminal hexahistidine tag, as N-terminal tags interfere with receptor phosphorylation, separated by a Val-Asp linker. Initial attempts to purify recombinant GRK5 from *E. coli* yielded insoluble protein. Expression in *E. coli* cell lines co-expressing different chaperones or the use of slower promoters such as Trc did not yield soluble protein (data not shown). Screening buffer additives revealed the addition of 0.02% (v/v) Triton-X100 or DNase to yield soluble protein
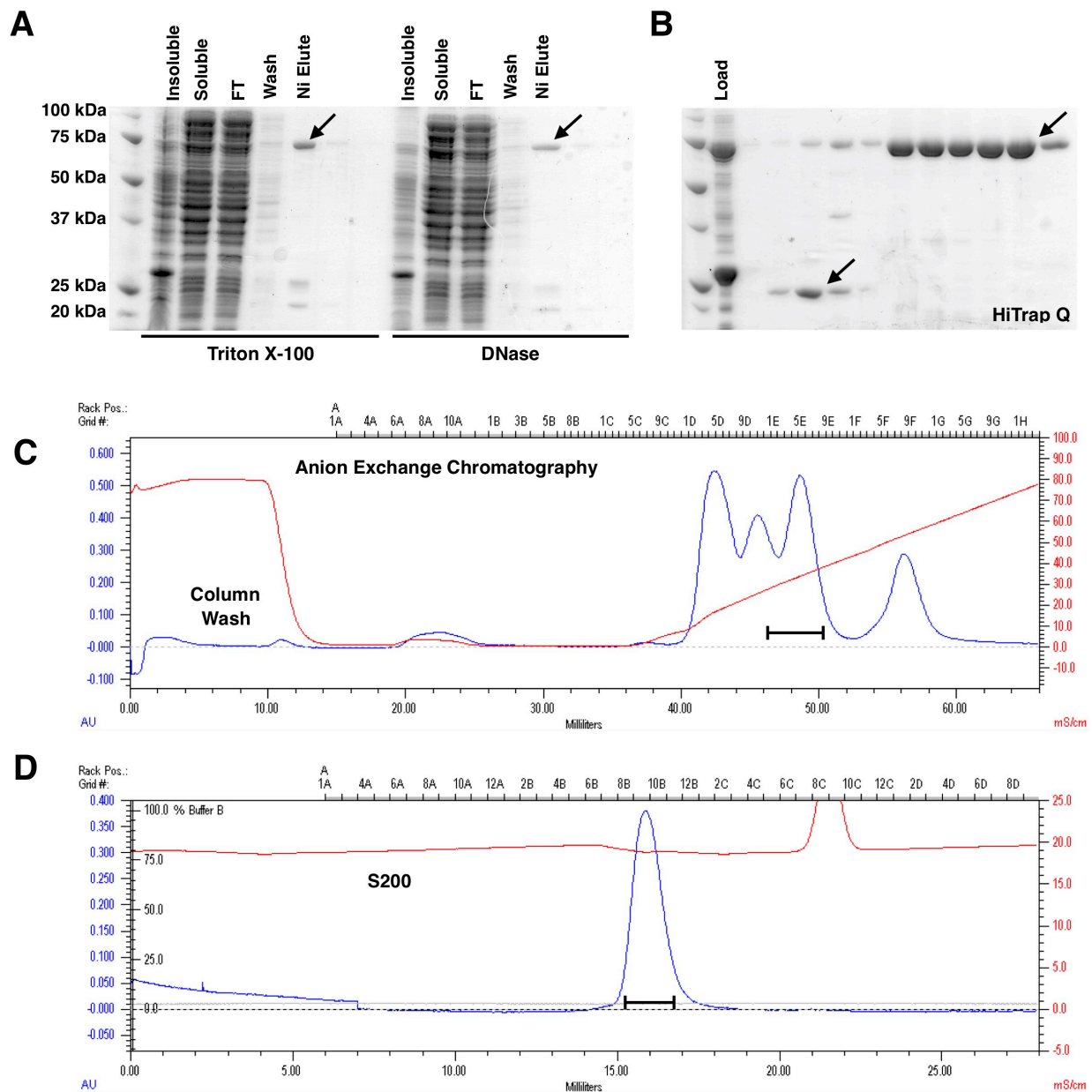
Figure 5.2: Purification of full-length, human GRK5 from *E. coli*. **A)** Comparison of small-scale expression tests with either Triton X-100 or DNase added to the lysis buffer. Flow-through (FT). GRK5 is indicated with an arrow. **B)** Further purification via anion exchange chromatography. Truncated kinase (left arrow) elutes prior to full-length GRK5 (right arrow). **C)** Representative anion exchange chromatogram from a HiTrap Q column. The blue trace is UV absorbance at 280 nm and the red trace is conductivity. The far right peak is composed of nucleic acid (by absorbance at 260 nm), **D)** Representative SEC chromatogram from an analytical S200 column. Eluted GRK5 is indicated by a bar under the peak.

(**Figure 5.2**). Because soluble protein was obtained through the addition of DNase, it is likely that GRK5 associates with genomic DNA and pellets during ultracentrifugation, as GRK5 contains a DNA-binding element in the large lobe of its kinase domain (residues 388-395) (Johnson *et al.*, 2004). Furthermore, purification via anion exchange chromatography (**Figure 5.2 C**) results in a large elution peak composed of nucleic acid, presumably short, digested genomic DNA associated with GRK5.

Western blotting with an antibody for the N-terminus of GRK4/5/6 revealed the presence of significant truncated kinase, especially in the C-terminus as the majority of the bands are nearly full-length (**Figure 5.3 A,B**). However, since the hexahistidine affinity tag is C-terminal, any prematurely truncated kinase will not bind Ni affinity resin and is easily separated from full-length GRK5. Analysis of the codon abundance in *E. coli* suggests the smaller N-terminal fragments of GRK5 are the result of premature termination of protein translation, as a groups of rare codons are located in the human GRK5 gene that would yield truncation products of the approximate sizes observed (**Figure 5.3 C**). Expression was attempted in Rosetta *E. coli* containing the pRARE plasmid which encodes rare tRNAs without a reduction in truncated kinase. Furthermore, neither reduction of the expression temperature or IPTG concentration reduced the quantity of truncated GRK5. Codon optimization of the GRK5 gene also did not improve overall yields or reduce the prevalence of truncated product.

5.3.2. Thermal stability of bacterially expressed GRK5. To ensure GRK5 purified from *E. coli* was properly folded, DSF was performed to measure the thermal melting point (T_m) of the protein (**Figure 5.4**). No statistically significant difference is observed between GRK5 purified from insect cells and from bacteria. Bacterially expressed GRK5 is thermally stabilized
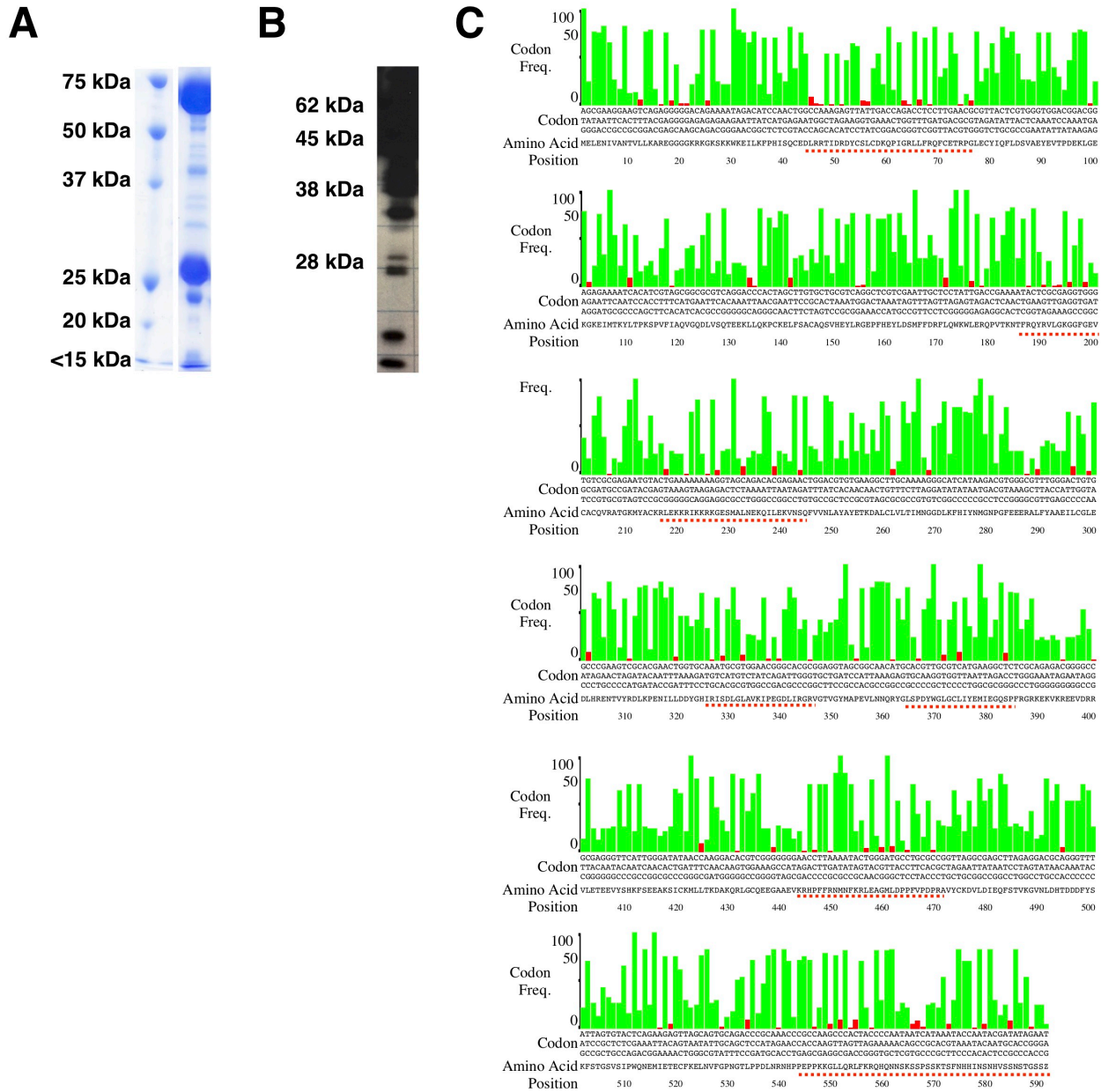
Figure 5.3: Codon usage and premature termination of GRK5. **A)** SDS-PAGE analysis of GRK5 expressed in *E. coli*. The gel was stained with coomassie stain. **B)** Western blotting with an antibody recognizing the N-terminus of GRK4/5/6 reveals that most bands observed by coomassie staining are N-terminal fragments of GRK5. **C)** Codon usage analysis reveals several patches of low-abundance codons (underlined in red) that likely produce the bands observed in panels A and B.
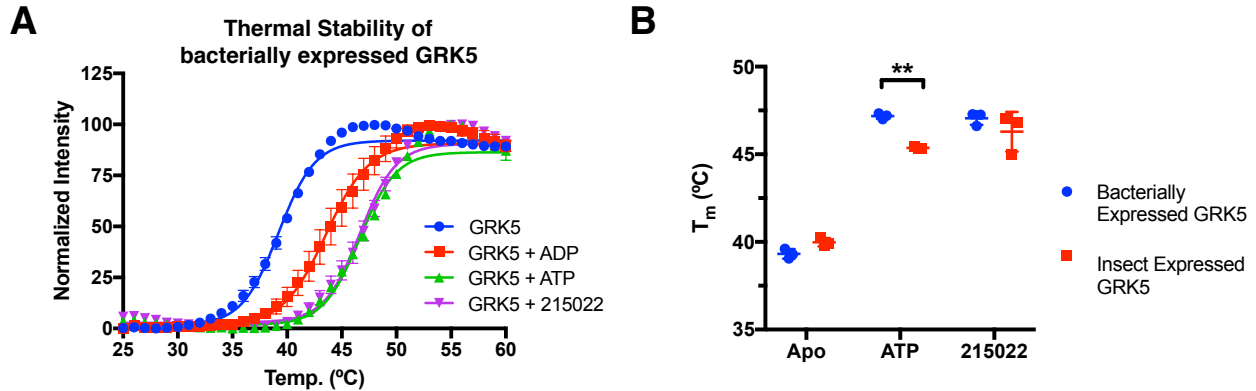
Figure 5.4: Thermal stability of GRK5 assessed by DSF. **A)** Melt curves for GRK5 expressed and purified from *E. coli*. Data points represent mean ± SD (n=3). **B)** Melting temperature (T_m) for human GRK5 expressed and purified in insect or *E. coli* cells in the presence or absence of ligand. ΔT_m relative to the corresponding apo T_m. Data reported as mean ± SD (n=3). Statistical significance determined via two-way ANOVA with Bonferroni correction for multiple comparisons between bacterially and insect expressed GRK5 (**$p<0.01$).

	T_m (°C)	ΔT_m (°C)
Insect GRK5	40.0 ± 0.2	
Insect+ATP	45.4 ± 0.1	+5.4
Insect+ CCG-215022	46.3 ± 1.0	+6.3
Bacterial GRK5	39.2 ± 0.1	
Bacterial+ADP	43.5 ± 0.1	+4.3
Bacterial+ATP	46.6 ± 0.2	+7.4
Bacterial+CCG-215022	46.7	+7.5

by 5-7 °C upon the addition of $Mg^{2+}\cdot$ATP or CCG-215022 similarly to GRK5 purified from

insect cells. A slight but significant increase in melting temperature is observed for bacterially

expressed GRK5 in the presence of ATP suggesting an increased affinity for the ligand.

5.3.3. Identification of unusual phosphorylation sites in GRK5. While confirming the

identity of the purified GRK5 by western blotting, it was observed that bacterially expressed

GRK5 is a slightly higher molecular weight than insect expressed GRK5 (**Figure 5.5 A**).

Suspecting autophosphorylation, GRK5e was treated with λ phosphatase and a decrease in

molecular weight was observed (data not shown), suggesting that the kinase was indeed

phosphorylated. To confirm phosphorylation, bacterially expressed GRK5 was analyzed via

intact protein mass spectrometry using QTOF-MS/MS (**Figure 5.5 A**). MS analysis revealed all

protein to be phosphorylated between two and eight times with the most common being three to

five phosphates.

To identify which sites on GRK5 are phosphorylated, phosphosite analysis was performed. The data show extensive phosphorylation, primarily in the disordered C-terminus (**Figure 5.5 B-F, Table 5.1**). The two highest scoring phosphorylated peptides contain the canonical AGC kinase autophosphorylation sites Ser484 and Thr485 in the AST loop. Other frequently modified sites included Thr10 in the αN helix and Thr404 in the large lobe of the kinase domain. Despite very low abundance, simultaneous phosphorylation was identified at Thr73, Ser86, and Thr93 in the RH domain and Thr494 and Ser500 in the AST/kinase domain. A series of phosphorylation sites were identified in the C-terminus following the αC helix (residues 565-590). Between one and eleven phosphorylation sites were identified in this region with the most prominent being four. Interestingly, several unusual types of phosphorylation were observed including phosphorylated histidine, cysteine, and aspartate residues. While histidine phosphorylation is uncommon, but well documented, in both prokaryotes and eukaryotes, phosphorylation of cysteine and aspartate residues is rare and only usually observed in prokaryotes. Taken together, our data suggest that GRK5 purified from *E. coli* is phosphorylated at the canonical sites Ser484 and Thr485 are with additional modification(s) primarily in the disordered, serine-rich C-terminus.

5.3.4. Kinetic analysis of bacterially expressed GRK5. To demonstrate that GRK5 purified from *E. coli* was catalytically active and to determine the effect of hyperphosphorylation on the activity of GRK5, phosphorylation kinetics were determined through radiometric assays using purified rhodopsin in native membranes or soluble tubulin monomers as the substrate. Bacterially expressed and purified GRK5 has a significantly lower V_{max} and apparent $K_{m, ATP}$ compared to insect expressed GRK5 in rhodopsin phosphorylation assays (**Figure 5.6 A,B**).

Figure 5.5: Representative mass spectrometry peptide fragment ions. **A)** Western blotting for the C-terminal hexahistidine tag showing a size difference between kinase from two expression systems (inset) and intact protein MS revealing multiple phosphorylated species for GRK5 purified from *E. coli*. Exact mass of unphosphorylated GRK5 is 68,823.65 Da. **B)** Phosphorylated peptides spanning GRK5 residues 1-14, **C)** 140-154, **D-E)** 476-487, and **F)** 571-590+hexahistidine tag.

Table 5.1: Phosphosite Mapping of GRK5 purified from *E. coli*

Peptide (# hits with PTM)	GRK5 Residue Range	Type of Phosphorylation	Phosphorylation Site Score[a]
MELENIVAN<u>T</u>VLLK (1)	1-14	Thr	66
TIDRDY<u>C</u>SL<u>C</u>DKQPIGR (1)	48-64	Cys	35
QFCE<u>T</u>RPGLECYIQFLD<u>S</u>VAEYEV <u>T</u>PDEKLGEK (1)	69-101	2x Thr, 1x Ser	3
ELFSA<u>C</u>AQSVHEYLR (1)	140-154	Cys	45
VLE<u>T</u>EEVYSHK (1)	401-411	Thr	14
LG<u>C</u>QEEGAAEVK (1)	432-443	Cys	47
LG<u>C</u>QEEGAAEVKR (1)	432-444	Cys	79
DVLDIEQFS<u>T</u>VK (1)	476-487	Thr	74
DVLDIEQF<u>S</u><u>T</u>VK (1)	476-487	Ser, Thr	51
DVLDIEQF<u>S</u>TVKGVNLDH<u>T</u>DDDF Y<u>S</u>K (2)	476-501	Ser, Thr	89
DVLDIEQF<u>S</u>TVKGVNLDHTDDDF Y<u>S</u>K (2)	476-501	Ser	77
DVLDIEQFS<u>T</u>VKGVNLDH<u>T</u>DDDF YSK (2)	476-501	Thr	47
DVLDIEQFSTVKGVNLD<u>H</u>TDDDF YSK (1)	476-501	His	11
<u>SS</u>PS<u>S</u>K<u>T</u>SFNHHIN<u>S</u>NHV<u>SS</u>N<u>S</u>TG <u>SS</u>VDHHHHHH (1)	565-590+hexahistidine	Ser, Thr	25
<u>SS</u>PS<u>S</u>K<u>T</u>SFNHHIN<u>S</u>NHV<u>SS</u>N<u>S</u>TG <u>SS</u>VDHHHHHH (1)	565-590+hexahistidine	11x Ser	6
T<u>S</u>FNHHIN<u>S</u>NHV<u>SS</u>N<u>S</u>TG<u>SS</u>VDH HHHHH (1)	571-590+hexahistidine	4x Ser	67
T<u>S</u>FNHHIN<u>S</u>NHV<u>SS</u>N<u>S</u>TGSSVDH HHHHH (5)	571-590+hexahistidine	Ser	33
T<u>S</u>FNHHINSNHV<u>SS</u>N<u>S</u>TG<u>SS</u>VDH HHHHH (3)	571-590+hexahistidine	2x Ser	32
TSFNHHINSNHVSSNSTGSSV<u>D</u>H HHHHH (1)	571-590+hexahistidine	Asp	23
TSFN<u>H</u>HINSN<u>H</u>VSSNSTGSSV<u>D</u>H <u>H</u>HHHH (1)	571-590+hexahistidine	Asp, His	21

[a]Phosphorylation Site Score indicates both relative abundance and confidence in PTM assignment. The largest score for the group of peptides is shown. Phosphorylatable residues of the type identified are underlined. Scores ≥40 indicate definitive assignment of the indicated PTM to the corresponding peptide. Multiple hits for the same PTM on a peptide suggests a heterogeneous population (i.e., phosphorylation of different residues when multiple of the same type of site exist on a peptide).
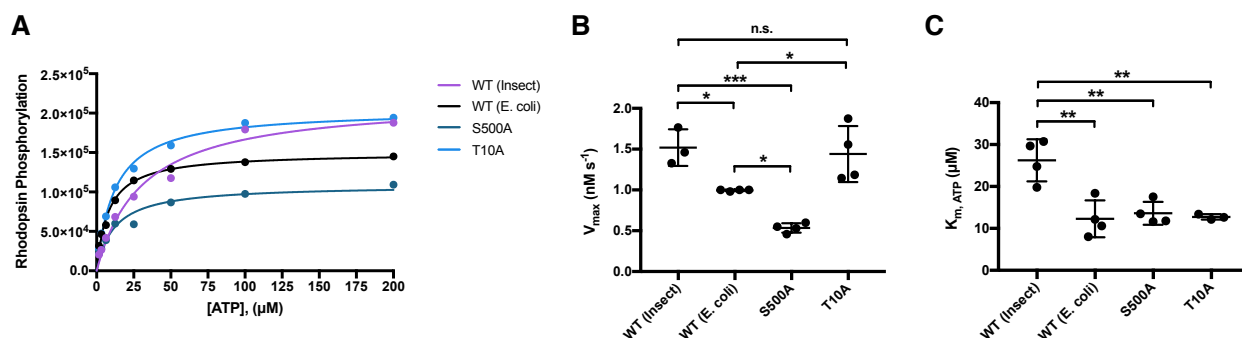
Figure 5.6: Steady-state kinetic analysis of GRK5 variants. **A)** Representative Michaelis-Menten kinetic curves from one experiment with rhodopsin in native membranes in substrates. **B)** V_{max} and **C)** K_m (for ATP) values for GRK5 protein variants purified from insect or *E. coli* cells (n=3-4). Assays performed with the assistance of Qiuyan Chen (Purdue University and University of Michigan). Statistical significance determined via one-way ANOVA with Tukey's correction for multiple comparisons (*$p<0.05$, **$p<0.01$, ***$p<0.001$, n.s.=not significant $p>0.05$).

Table 5.2: Crystallographic data collection statistics

GRK5·ATP	
Wavelength (Å)	1.03315
Resolution range	65.42 - 8.22
	(8.51 - 8.22)*
Space group	$C\,2\,2\,2_1$
Unit cell constants (Å, °)	375.7 456.3 351.2
	90 90 90
Total reflections	393667 (38492)
Unique reflections	29590 (2871)
Multiplicity	13.3 (13.4)
Completeness (%)	99.7 (98.7)
Mean I/σ(I)	8.6 (2.3)
R_{meas}	0.274 (1.26)
$CC_{1/2}$	0.992 (0.832)

*Statistics for the highest-resolution shell are shown in parentheses

However, no significant difference in either kinetic parameter is observed for tubulin phosphorylation (Yao *et al.*, 2017). Analysis of the phosphorylation sites led to the identification of p-Thr10 and p-Ser500 as possible causes for the observed decrease in activity. Thr10 and Ser500 are among the most common phosphorylation sites beyond the canonical Ser484 and Thr485. Thr10 is located in the αN helix that has been proposed to interact with activated receptors and may explain the kinetic differences only toward receptor substrates (Noble *et al.*, 2003; Huang and Tesmer, 2011). Ser500 is located in a region of the AST loop near the membrane interface for GRKs and thus, phosphorylation may repel acidic phospholipid headgroups. Phospho-null GRK5 S500A further decreased V_{max} toward rhodopsin and had no effect on K_m (**Figure 5.6 C**). GRK5 T10A significantly increased V_{max} to that of insect expressed GRK5 without affecting K_m.

5.3.5. Crystallization of hyperphosphorylated GRK5. To determine if non-canonical phosphorylation has an effect on the structure of GRK5, bacterially expressed GRK5 with hyperphosphorylation was crystallized. A variety of ligands including ADP, AMP-PNP, ATP, sangivamycin, and CCG-215022 were tested with only $Mg^{2+} \cdot ATP$ yielding crystals. Four different sets of conditions yielded crystals, two of which were reproducible with GRK5 from different purifications (**Figure 5.7 A,B**). The diffraction of all crystals was poor with the best yielding weak and highly anisotropic diffraction that processes to 7.7-8.5 Å in XDS in space group $C222$ or $C222_1$ (**Figure 5.7 C, Table 5.2**). The extremely large volume (375.6, 456.3, 351.2 Å; a, b, c) of the unit cell and weak diffraction suggests a high solvent content and/or many protein copies (**Figure 5.7 D**). Furthermore, the unit cell volume yields a broad Matthew's coefficient distribution which makes determination of the probable number of protein copies in
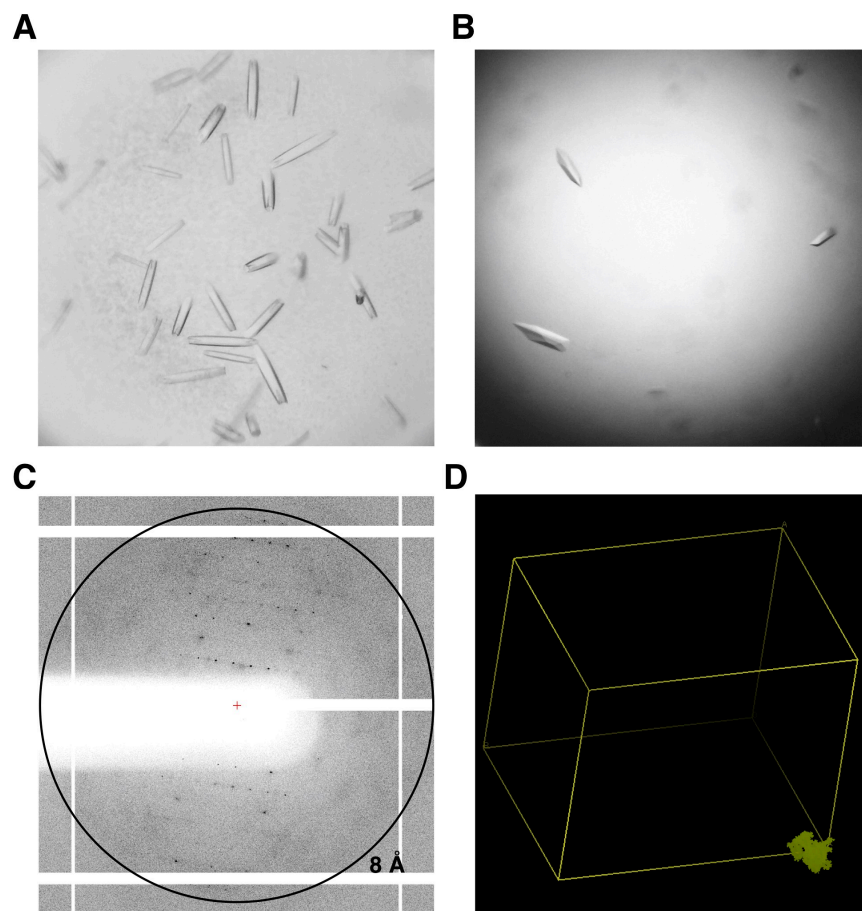
Figure 5.7: Crystallization and diffraction of bacterially expressed GRK5 with hyperphosphorylation. **A)** Crystals grown of GRK5 with 5 mM Mg^{2+} and 2 mM ATP in 0.2 M KCl, 0.05 M HEPES pH 7.5, 35% pentaerythritol propoxylate (5/4 PO/OH) at 4 ºC or **B)** 0.1 M Bis-Tris pH 5.5 and 35% tacsimate. **C)** Diffraction image of GRK5 crystals shown in panel A. Diffraction extends to ~8 Å spacings and is highly anisotropic. **D)** Unit cell and single GRK5 (~70 kDa, bottom right) placed via MR. The space group is likely *C*222 with unit cell dimensions of 375.6, 456.3, 351.2 Å (a, b, c).

the unit cell difficult but is likely >20 protomers.

Molecular replacement (MR) with the highest resolution data set was attempted with Molrep, Phaser, MoRDa, Balbes, and MrBUMP (Vagin *et al.*, 1997; McCoy *et al.*, 2007; Long *et al.*, 2008; Winn *et al.*, 2011; Keegan *et al.*, 2018). Phaser easily generated solutions with 1-4 copies of GRK5 per asymmetric unit (ASU) (**Figure 5.7 D**). While these solutions were statistically definitive (translation function Z score >8), much of the unit cell remained unoccupied and searching for more than a few copies or trying to identify non-crystallographic symmetry (NCS) operators were extremely time consuming with routine computing resources. MoRDa, Balbes, and MrBUMP were run through the ccp4 online servers which have additional computational resources for use on complex MR jobs. Only MoRDa yielded possible MR solutions containing 28-36 copies of either GRK1 or GRK6 per ASU. Additionally, refinement of such a large solution was similarly computationally intensive. Thus, the online PDB Redo server utilizing a modified Refmac protocol was used for refinement. Unfortunately, identifying an MR solution that appropriately refines (decrease in R factors and improvement in map quality) has not been possible.

5.4. Discussion

Bacterial expression and purification represents a faster and more cost effective route to obtain GRK5. While prior attempts to purify GRK5 from *E. coli* led to insoluble protein, we show that the simple addition of detergent or DNase is sufficient to obtain quality protein, the latter of which suggests the protein associates with genomic DNA. Indeed, GRK5 contains both a NLS and DNA binding element as a small fraction of endogenous GRK5 is nuclear and

involved in the regulation of gene expression (Johnson *et al.*, 2004). When purified from insect cells, nuclei are not often disrupted and thus GRK5 does not pellet with nucleic acids. Interestingly, the presence of the C-terminal Val-Asp-hexahistidine tag was required for purification. Placing the affinity purification tag on the N-terminus yielded soluble protein without activity toward receptors, but for an unknown reason, omission of the Val-Asp spacer on the C-terminal tag yielded insoluble protein. Attempts to purify soluble GRK2 as previously reported (Gan *et al.*, 2000) or GRK1 in *E. coli* have been unsuccessful. Perhaps, GRK5 is uniquely suited for bacterial expression, however expression and purification other GRKs in *E. coli* need to be attempted before such a conclusion can be made.

Interestingly, the resulting GRK5 displays an unusual pattern of phosphorylation that has a significant effect on catalytic activity towards receptor but not soluble substrates. As bacteria lack canonical Ser/Thr kinases, most phosphorylation events are likely the result of GRK5 autophosphorylation. Autophosphorylation at some sites may occur during expression in insect and mammalian cells but are removed by phosphatases which bacteria lack. The presence of uncommon and rare phosphorylation events on histidine, cysteine, and aspartate highlights the differences in cell physiology between prokaryotes and eukaryotes. Histidine and aspartate phosphorylation are often coupled, as phosphates are typically attached to histidine residues during the intermediate steps of aspartate phosphorylation which is common in two-component signaling in bacteria (Swanson *et al.*, 1994; West and Stock, 2001). Cysteine phosphorylation is remarkably common in prokaryotes and is essential for the phosphotransferase system used to phosphorylate glucose during transport (Guan and Dixon, 1991; Stuckey *et al.*, 1994; Pannifer *et*

al., 1998; Sun *et al.*, 2012). However, phosphorylation of histidine, cysteine, and aspartate residues outside of the aforementioned biological processes is rare and not well understood.

The majority of observed phosphorylation sites are located in the C-terminus and might be expected to repel the membrane binding αC helix from membranes thereby reducing the efficiency of receptor phosphorylation. The decrease in activity towards receptors is less dramatic than expected from hyperphosphorylation, possibly due to the phosphorylation sites being in the extreme C-terminus rather than adjacent to the membrane binding αC helix. Indeed, analysis of the C-terminus of GRK6 revealed that residues immediately following the αC helix (561-567) enhance membrane association and receptor phosphorylation while residues in the extreme C-terminus act in an autoinhibitory fashion (Vatter *et al.*, 2005). Since the residues responsible for enhancing membrane association include serine residues that were phosphorylated in our analyses, these residues warrant further investigation via mutagenesis and kinetic analysis.

Mutation of selected phosphorylation sites elsewhere in GRK5 identified Thr10 in the αN helix as a key contributor to the decreased activity towards receptors, as the presumably hyperphosphorylated T10A variant exhibited the same activity as GRK5 purified from insect cells which lacks phosphorylation at this site. Restoration of catalytic activity upon mutation of Thr10 is in line with what is hypothesized about GRK-GPCR docking interactions (Huang and Tesmer, 2011). Phosphorylation of Thr10 would introduce a bulky charged group in a region of the kinase that is proposed to dock into or near the hydrophobic core of activated GPCRs. Interestingly, bacterially expressed, hyperphosphorylated GRK5 displays a significantly decreased apparent K_m for ATP indicating a higher affinity for ATP than minimally

phosphorylated GRK5 from insect cells potentially explaining the significant enhancement in thermal stability in the presence of ATP. The prevalence of canonical AST loop autophosphorylation in GRK5 purified from bacteria, which activates AGC family kinases (Kunapuli *et al.*, 1994), may explain the increase in apparent K_m and thermal stability since GRK5 purified from insect cells generally lacks AST loop phosphorylation unless stimulated by phospholipids.

The described construct and purification scheme will facilitate diverse future studies of GRK5. Bacterial expression and purification enables the incorporation of unnatural amino acids via amber stop codons into GRK5 (Chin *et al.*, 2002). The incorporation of photocrosslinking unnatural amino acids may enable the capture and study of novel GRK5 binding partners or substrates in cells (Dumas *et al.*, 2015). Furthermore, selective crosslinking may aid in the trapping and determination of a GRK5-GPCR structure by capturing the transient interaction with a greater amount of homogeneity than obtained with other crosslinking strategies. NMR studies involving GRKs have been limited due to the difficulty of producing isotopically labeled kinase in insect cells and their large size (65-80 kDa). As isotope labeling methods are well established in bacterial systems, obtaining GRK5 suitable for NMR studies will be more easily attainable, facilitating the study of GRK5 dynamics and protein-protein interactions. Beyond the aforementioned technical advantages, bacterial expression of GRK5 is simply faster and cheaper which is advantageous when studying GRK5 with limited resources.

Chapter 6: Conclusions and Future Directions

6.1. Development of inhibitors targeting IKKε and TBK1. The identification of the non-canonical inflammatory kinases IKKε and TBK1 as key regulators of obesity and the development of type 2 diabetes has lead to interest in the pharmacologically targeting of both kinases. Preliminary work identified IKKε and TBK1 as targets of the unrelated FDA-approved drug amlexanox. Treatment with amlexanox improved insulin sensitivity, among other beneficial effects, in clinical trials with obese and diabetic patients. My aim was to use structural biology to characterize the binding of amlexanox to its target kinases to facilitate the design of analogs with improved potency, selectivity, and efficacy.

To this end, I solved the TBK1·amlexanox structure which revealed type I, ATP-competitive binding along the kinase hinge. The structure revealed an important interaction between the carboxylate on amlexanox and Thr156 in the kinase. SAR established that this interaction was essential for potent inhibition of only TBK1, alluding to a mechanism for the development of IKKε selective inhibitors. Furthermore, modification of solvent exposed regions of the kinase improved potency, through unusual interactions with the neighboring dimerization domain, and also efficacy in cellular and animal models of obesity.

Of more than 100 analogs, we identified several with potencies as low as 200 nM and enhanced efficacy, though these two properties appear to be mutually exclusive. While not uncommon in therapeutic development, questions still remain as to the disconnect between *in vitro* kinase inhibition and cellular response. Generally, inhibitor solubility correlated well with

potency but not efficacy, suggesting undesirable pharmacokinetic properties. As adipocytes contain large fat deposits, lipophilic inhibitors may accumulate in the cells to produce a greater response. Indeed, the most efficacious compounds bear lipophilic groups such as cyclohexyl and *iso*-pentyl. Exploration of variants of the amlexanox pharmacophore, such as the two ring inhibitor series described here, may yield inhibitors with improved efficacy in animals. Future studies and inhibitor development should include permeability assays, such as PAMPA or Caco-2 cells, to screen compounds prior to extensive *in vivo* studies. Despite significant improvements in potency *in vitro*, no analogs display superior efficacy to amlexanox in animals. As inhibitors targeting TBK1 and IKKε affect both the obese and diabetic phenotypes, a combination of readouts, such as IL-6 secretion and p-p38, for efficacy are considered when examining efficacy. Some amlexanox analogs produced greater efficacy in select readouts in cultured adipocytes but failed to elicit a greater response in obese mice. Such an observation is not uncommon, as inhibitor distribution and metabolism is more complex *in vivo* than in cell culture. Perhaps, the response achieved with amlexanox or select analogs represents the ceiling for efficacy for engagement of the targets TBK1 and IKKε which would necessitate the identification and targeting of novel members of thermogenic and insulin signaling cascades.

Emerging evidence suggests that IKKε and TBK1 play different roles in metabolic disease (Chiang *et al.*, 2009; Zhao *et al.*, 2018). Despite characterizing more than 100 analogs, none with exquisite selectivity were identified. Given that IKKε and TBK1 are >70% in sequence in their kinase domains, improving upon inhibitor selectivity will likely require the elucidation of an IKKε crystal structure of which none have been reported despite extensive efforts on my own part. Such structure could enable the identification of subtle structural

123

differences from TBK1 which may be exploited in future inhibitor analogs. Attempts to crystallize IKKε were complicated by the tendency of IKKε to aggregate during purification. Because extensive screening of buffer conditions and constructs including the isolate kinase domain, kinase-ubiquitin-like domains, and C-terminally truncations analogous to the crystallized TBK1 construct have already been performed without success, alternative approaches such as the identification of new constructs by proteolytic digestion or the introduction of binding partners may aid in stabilizing the protein. However, many interacting partners require polyubiquitination of IKKε for binding (Chau *et al.*, 2008; Tu *et al.*, 2013; Zhou *et al.*, 2013; Rajsbaum *et al.*, 2014), adding another layer of complexity for crystallographic studies. Because IKKε functions as a 160 kDa homodimer (Huynh *et al.*, 2002; Chau *et al.*, 2008), atomic-resolution structure determination should now be feasible by cryo-EM which does not require highly concentrated protein samples.

6.2. Characterization and targeting of the Ca^{2+}·CaM–GRK5 complex. Recent identification of the role of Ca^{2+}·CaM-mediated nuclear GRK5 translocation in the progression of cardiac hypertrophy has renewed interest in a this protein-protein interaction that was first described more than two decades ago. Here, I described the architecture of the complex and use a variety of peptide and natural product probes to interrogate the interactions between the proteins and their effects on kinase regulation. Ca^{2+}·CaM interacts with GRK5 along the membrane binding surface of the kinase and RH domains, most likely through simultaneous interactions with the N- and C-terminal helices and the PIP$_2$ binding patch, with the net effect of dissociating GRK5 from membranes and permitting its nuclear translocation.

Our current understanding of the precise molecular interactions between GRKs and Ca^{2+}·CaM is limited by the low resolution of SAXS and negative stain EM, necessitating the elucidation of higher resolution structures. Co-crystallization of the complex has been unsuccessful possibly due to the dynamic nature of Ca^{2+}·CaM and the interacting regions of GRK5. Indeed, the αN helix, basic phospholipid binding patch, and C-terminus where Ca^{2+}·CaM binds are not resolved in most GRK crystal structures or are trapped in crystal contacts (Tesmer *et al.*, 2005; Lodowski, Tesmer, Benovic, *et al.*, 2006; Komolov *et al.*, 2015; Homan, Waldschmidt, *et al.*, 2015; Allen *et al.*, 2015). Furthermore, the 90 kDa size of the Ca^{2+}·CaM–GRK5 complex poses challenges for structural analysis by EM, however recent advances in data processing software and physical technology, such as the implementation of phase plates and energy filters, will alleviate these size restrictions in the near future.

Future studies of the Ca^{2+}·CaM–GRK5 complex should focus on connecting biochemical and biophysical characterization of the interaction to cellular physiology and *in vivo* pathologies. We have shown that the binding of Ca^{2+}·CaM generally activates GRK5 toward soluble substrates and thus, whole-cell phosphoproteomic analysis may reveal new cytosolic targets of Ca^{2+}·CaM-activated GRK5. Furthermore, the identification of the natural product malbrancheamide, which is likely cell permeable, as a partial inhibitor of the bitopic Ca^{2+}·CaM–GRK5 interaction will enable selective probing of the protein-protein interaction in cells. The bitopic nature of the interaction and the selective disruption of one half of the interaction sheds light on a possible route for therapeutic intervention. Our data suggest that disruption of the Ca^{2+}·CaM C-lobe interaction with GRK5 may maintain membrane localization and attenuate the cardiac hypertrophic response. The effect of the common Ca^{2+}·CaM inhibitor calmidazolium,

which completely blocks $Ca^{2+} \cdot CaM$ binding, on the hypertrophy in cells revealed therapeutic potential for targeting this interaction but may lead to adverse side effects as calmidazolium also inhibits a plethora of ion channels (Gold *et al.*, 2013). Future efforts should examine the effects of other natural product $Ca^{2+} \cdot CaM$ inhibitors related to malbrancheamide as potential therapeutic leads for cardiac hypertrophy because such compounds will expand efforts to target $Ca^{2+} \cdot CaM$ into new chemical space.

References

Adams PD, Afonine PV, Bunkóczi G, Chen VB, Davis IW, Echols N, Headd JJ, Hung L-W, Kapral GJ, Grosse-Kunstleve RW, McCoy AJ, Moriarty NW, Oeffner R, Read RJ, Richardson DC, Richardson JS, Terwilliger TC, and Zwart PH (2010) PHENIX: a comprehensive Python-based system for macromolecular structure solution. *Acta Crystallogr D Biol Crystallogr* **66**:213–221.

Alessi DR, Cuenda A, Cohen P, Dudley DT, and Saltiel AR (1995) PD 098059 is a specific inhibitor of the activation of mitogen-activated protein kinase kinase in vitro and *in vivo*. *J Biol Chem* **270**:27489–27494.

Allen SJ, Parthasarathy G, Darke PL, Diehl RE, Ford RE, Hall DL, Johnson SA, Reid JC, Rickert KW, Shipman JM, Soisson SM, Zuck P, Munshi SK, and Lumb KJ (2015) Structure and Function of the Hypertension Variant A486V of G Protein-coupled Receptor Kinase 4. *J Biol Chem* **290**:20360–20373.

Arbuzova A, Murray D, and McLaughlin S (1998) MARCKS, membranes, and calmodulin: kinetics of their interaction. *Biochim Biophys Acta* **1376**:369–379.

Arencibia JM, Pastor-Flores D, Bauer AF, Schulze JO, and Biondi RM (2013) AGC protein kinases: from structural mechanism of regulation to allosteric drug development for the treatment of human diseases. *Biochim Biophys Acta* **1834**:1302–1321.

Barancík M, Bohácová V, Kvackajová J, Hudecová S, Krizanová O, and Breier A (2001) SB203580, a specific inhibitor of p38-MAPK pathway, is a new reversal agent of P-glycoprotein-mediated multidrug resistance. *Eur J Pharm Sci* **14**:29–36.

Bell J (2005) Amlexanox for the Treatment of Recurrent Aphthous Ulcers. *Clin Drug Investig* **25**:555–566.

Beyett TS, Bandekar SJ, and Tesmer JJG (2016) Molecular Basis for Targeting, Inhibition, and Receptor Phosphorylation in the G Protein-Coupled Receptor Kinase 4 Subfamily. In: Gurevich V., Gurevich E., Tesmer JJG. (eds) G Protein-Coupled Receptor Kinases. Methods in Pharmacology and Toxicology. Humana Press, New York, NY.

Bhattacharya S, Bunick CG, and Chazin WJ (2004) Target selectivity in EF-hand calcium binding proteins. *Biochim Biophys Acta* **1742**:69–79.

Boguth CA, Singh P, Huang C-C, and Tesmer JJG (2010) Molecular basis for activation of G protein-coupled receptor kinases. *The EMBO Journal* **29**:3249–3259.

Bouley R, Waldschmidt HV, Cato MC, Cannavo A, Song J, Cheung JY, Yao X-Q, Koch WJ, Larsen SD, and Tesmer JJG (2017) Structural Determinants Influencing the Potency and Selectivity of Indazole-Paroxetine Hybrid G Protein-Coupled Receptor Kinase 2 Inhibitors. *Mol Pharmacol* **92**:707–717.

Cameron KO, and Kurumbail RG (2016) Recent progress in the identification of adenosine monophosphate-activated protein kinase (AMPK) activators. *Bioorg Med Chem Lett* **26**:5139–5148.

Cannon B, and Nedergaard J (2004) Brown adipose tissue: function and physiological significance. *Physiol Rev* **84**:277–359.

Casey LM, Pistner AR, Belmonte SL, Migdalovich D, Stolpnik O, Nwakanma FE, Vorobiof G, Dunaevsky O, Matavel A, Lopes CMB, Smrcka AV, and Blaxall BC (2010) Small molecule disruption of G beta gamma signaling inhibits the progression of heart failure. *Circ Res* **107**:532–539.

Chaikuad A, Koch P, Laufer SA, and Knapp S (2018) The Cysteinome of Protein Kinases as a Target in Drug Development. *Angew Chem Int Ed* **57**:4372–4385.

Chau TL, Gioia R, Gatot JS, and Patrascu F (2008) Are the IKKs and IKK-related kinases TBK1 and IKK-ε similarly activated? *Trends in Biochem Sci* **33**:171-180.

Chen VB, Arendall WB, Headd JJ, Keedy DA, Immormino RM, Kapral GJ, Murray LW, Richardson JS, and Richardson DC (2010) MolProbity: all-atom structure validation for macromolecular crystallography. *Acta Crystallogr D Biol Crystallogr* **66**:12–21.

Chiang S-H, Bazuine M, Lumeng CN, Geletka LM, Mowers J, White NM, Ma J-T, Zhou J, Qi N, Westcott D, Delproposto JB, Blackwell TS, Yull FE, and Saltiel AR (2009) The protein kinase IKKepsilon regulates energy balance in obese mice. *Cell* **138**:961–975.

Chin JW, Martin AB, King DS, Wang L, and Schultz PG (2002) Addition of a photocrosslinking amino acid to the genetic code of *Escherichia coli*. *Proc Nat Acad Sci* **99**:11020–11024.

Chuang TT, Paolucci L, and De Blasi A (1996) Inhibition of G protein-coupled receptor kinase subtypes by Ca^{2+}/calmodulin. *J Biol Chem* **271**:28691–28696.

Clark K, Peggie M, Plater L, Sorcek RJ, Young ERR, Madwed JB, Hough J, McIver EG, and Cohen P (2011) Novel cross-talk within the IKK family controls innate immunity. *Biochem J* **434**:93–104.

Clark K, Plater L, Peggie M, and Cohen P (2009) Use of the Pharmacological Inhibitor BX795 to Study the Regulation and Physiological Roles of TBK1 and IκB Kinase ε. *J Biol Chem* **284**:14136–14146.

Cook WJ, Walter LJ, Walter MR (1994) Drug binding by calmodulin: crystal structure of a calmodulin-trifluoperazine complex. *Biochem 33*:15259–15265.

Winter G, 2010 (2010) xia2: an expert system for macromolecular crystallography data reduction. *J Appl Cryst* **43**:186-190

Dallakyan S, and Olson AJ. (2015) Small-Molecule Library Screening by Docking with PyRx. *Meth Mol Biol* **263**:243-50.

Dar AC, and Shokat KM (2011) The evolution of protein kinase inhibitors from antagonists to agonists of cellular signaling. *Annu Rev Biochem* **80**:769–795.

Ding B, Glukhova A, Sobczyk-Kojiro K, Mosberg HI, Tesmer JJG, and Chen Z (2014) Unveiling the Membrane-Binding Properties of N-Terminal and C-Terminal Regions of G Protein-Coupled Receptor Kinase 5 by Combined Optical Spectroscopies. *Langmuir* **30**:823–831.

Dudley DT, Pang L, Decker SJ, Bridges AJ, and Saltiel AR (1995) A synthetic inhibitor of the mitogen-activated protein kinase cascade. *Proc Nat Acad Sci* **92**:7686–7689.

Dumas A, Lercher L, Spicer CD, and Davis BG (2015) Designing logical codon reassignment – Expanding the chemistry in biology. *Chem Sci* **6**:50–69.

Emsley P, Lohkamp B, Scott WG, and Cowtan K (2010) Features and development of Coot. *Acta Crystallogr D Biol Crystallogr* **66**:486–501.

Feldkamp MD, Gakhar L, Pandey N, and Shea MA (2015) Opposing orientations of the anti-psychotic drug trifluoperazine selected by alternate conformations of M144 in calmodulin. *Proteins* **83**:989–996.

Ferguson FM, and Gray NS (2018) Kinase inhibitors: the road ahead. *Nat Rev Drug Discov* **17**:353–377.

Figueroa M, González-Andrade M, Sosa-Peinado A, Madariaga-Mazón A, Del Río-Portilla F, González MDC, and Mata R (2011) Fluorescence, circular dichroism, NMR, and docking studies of the interaction of the alkaloid malbrancheamide with calmodulin. *J Enzyme Inhib Med Chem* **26**:378–385.

Fraley AE, Garcia-Borràs M, Tripathi A, Khare D, Mercado-Marin EV, Tran H, Dan Q, Webb GP, Watts KR, Crews P, Sarpong R, Williams RM, Smith JL, Houk KN, and Sherman DH (2017) Function and Structure of MalA/MalA', Iterative Halogenases for Late-Stage C-H Functionalization of Indole Alkaloids. *J Am Chem Soc* **139**:12060–12068.

Franke D, and Svergun DI (2009) DAMMIF, a program for rapid *ab initio* shape determination in small-angle scattering. *J Appl Crystallogr* **42**:342–346.

Franke D, Petoukhov MV, Konarev PV, Panjkovich A, Tuukkanen A, Mertens HDT, Kikhney AG, Hajizadeh NR, Franklin JM, Jeffries CM, and Svergun DI (2017) ATSAS 2.8: a comprehensive data analysis suite for small-angle scattering from macromolecular solutions. *J Appl Crystallogr* **50**:1212–1225.

Fredriksson R, Lagerström MC, Lundin L-G, and Schiöth HB (2003) The G-protein-coupled receptors in the human genome form five main families. Phylogenetic analysis, paralogon groups, and fingerprints. *Mol Pharmacol* **63**:1256–1272, American Society for Pharmacology and Experimental Therapeutics.

Frey N, and Olson EN (2003) Cardiac hypertrophy: the good, the bad, and the ugly. *Annu Rev Physiol* **65**:45–79.

Gan XQ, Wang JY, Yang QH, Li Z, Liu F, Pei G, and Li L (2000) Interaction between the conserved region in the C-terminal domain of GRK2 and rhodopsin is necessary for GRK2 to catalyze receptor phosphorylation. *J Biol Chem* **275**:8469–8474.

Gold JI, Martini JS, Hullmann J, Gao E, Chuprun JK, Lee L, Tilley DG, Rabinowitz JE, Bossuyt J, Bers DM, and Koch WJ (2013) Nuclear translocation of cardiac G protein-Coupled Receptor kinase 5 downstream of select Gq-activating hypertrophic ligands is a calmodulin-dependent process. *PLoS ONE* **8**:e57324.

González-Andrade M, Rodríguez-Sotres R, Madariaga-Mazón A, Rivera-Chávez J, Mata R, Sosa-Peinado A, del Pozo-Yauner L, and Arias-Olguín II (2016) Insights into molecular interactions between CaM and its inhibitors from molecular dynamics simulations and experimental data. *J Biomol Struct Dyn* **34**:78–91.

Guan KL, and Dixon JE (1991) Evidence for protein-tyrosine-phosphatase catalysis proceeding via a cysteine-phosphate intermediate. *J Biol Chem* **266**:17026–17030.

Gurevich EV, Tesmer JJG, Mushegian A, and Gurevich VV (2012) G protein-coupled receptor kinases: more than just kinases and not only for GPCRs. *Pharmacol Ther* **133**:40–69.

Gurevich VV, and Gurevich EV (2006) The structural basis of arrestin-mediated regulation of G-protein-coupled receptors. *Pharmacol Ther* **110**:465–502.

Hanyaloglu AC, and von Zastrow M (2008) Regulation of GPCRs by Endocytic Membrane Trafficking and Its Potential Implications. *Annu Rev Pharmacol Toxicol* **48**:537–568.

Hardie DG, Ross FA, and Hawley SA (2012) AMP-activated protein kinase: a target for drugs both ancient and modern. *Chemistry & Biology* **19**:1222–1236.

Hardie DG, Schaffer BE, and Brunet A (2016) AMPK: An Energy-Sensing Pathway with Multiple Inputs and Outputs. *Trends in Cell Biology* **26**:190–201.

Hari SB, Merritt EA, and Maly DJ (2013) Sequence determinants of a specific inactive protein kinase conformation. *Chemistry & Biology* **20**:806–815.

Hayden MS, and Ghosh S (2012) NF- B, the first quarter-century: remarkable progress and outstanding questions. *Genes & Development* **26**:203–234.

Hepler JR, and Gilman AG (1992) G proteins. *Trends Biochem Sci* **17**:383–387.

Homan K, Wu E, Cannavo A, Koch W, and Tesmer JJG (2014) Identification and Characterization of Amlexanox as a G Protein-Coupled Receptor Kinase 5 Inhibitor. *Molecules* **19**:16937–16949.

Homan KT, and Tesmer JJG (2014a) Molecular Basis for Small Molecule Inhibition of G Protein-Coupled Receptor Kinases *ACS Chem Biol* **10**:246–256.

Homan KT, and Tesmer JJG (2014b) Structural insights into G protein-coupled receptor kinase function. *Curr Opin Cell Biol* **27**:25–31.

Homan KT, Glukhova A, and Tesmer JJG (2013) Regulation of G protein-coupled receptor kinases by phospholipids. *Curr Med Chem* **20**:39–46.

Homan KT, Larimore KM, Elkins JM, Szklarz M, Knapp S, and Tesmer JJG (2015) Identification and structure-function analysis of subfamily selective g protein-coupled receptor kinase inhibitors. *ACS Chem Biol* **10**:310–319.

Homan KT, Waldschmidt HV, Glukhova A, Cannavo A, Song J, Cheung JY, Koch WJ, Larsen SD, and Tesmer JJG (2015) Crystal Structure of G Protein-coupled Receptor Kinase 5 in Complex with a Rationally Designed Inhibitor. *J Biol Chem* **290**:20649–20659.

Homan KT, Wu E, Wilson MW, Singh P, Larsen SD, and Tesmer JJG (2013) Structural and Functional Analysis of G Protein-coupled Receptor Kinase Inhibition by Paroxetine and a Rationally Designed Analog. *Mol Pharmacol* mol.113.089631.

Huang C-C, and Tesmer JJG (2011) Recognition in the face of diversity: interactions of heterotrimeric G proteins and G protein-coupled receptor (GPCR) kinases with activated GPCRs. *J Biol Chem* **286**:7715–7721.

Huang C-C, Orban T, Jastrzebska B, Palczewski K, and Tesmer JJG (2011) Activation of G protein-coupled receptor kinase 1 involves interactions between its N-terminal region and its kinase domain. *Biochem* **50**:1940–1949.

Huang C-C, Yoshino-Koh K, and Tesmer JJG (2009) A Surface of the Kinase Domain Critical for the Allosteric Activation of G Protein-coupled Receptor Kinases. *J Biol Chem* **284**:17206–17215.

Hullmann JE, Grisanti LA, Makarewich CA, Gao E, Gold JI, Chuprun JK, Tilley DG, Houser SR, and Koch WJ (2014) GRK5-mediated exacerbation of pathological cardiac hypertrophy involves facilitation of nuclear NFAT activity. *Circ Res* **115**:976–985.

Huse M, and Kuriyan J (2002) The conformational plasticity of protein kinases. *Cell* **109**:275–282.

Huynh QK, Kishore N, Mathialagan S, Donnelly AM, and Tripp CS (2002) Kinetic mechanisms of IkappaB-related kinases (IKK) inducible IKK and TBK-1 differ from IKK-1/IKK-2 heterodimer. *J Biol Chem* **277**:12550–12558.

Iacovelli L, Sallese M, Mariggiò S, and De Blasi A (1999) Regulation of G-protein-coupled receptor kinase subtypes by calcium sensor proteins. *FASEB J* **13**:1–8.

Inglese J, Glickman JF, Lorenz W, Caron MG, and Lefkowitz RJ (1992) Isoprenylation of a protein kinase. Requirement of farnesylation/alpha-carboxyl methylation for full enzymatic activity of rhodopsin kinase. *J Biol Chem* **267**:1422–1425.

Irannejad R, and von Zastrow M (2014) GPCR signaling along the endocytic pathway. *Curr Opin Cell Biol* **27**:109–116.

Jiang X, Benovic JL, and Wedegaertner PB (2007) Plasma membrane and nuclear localization of G protein coupled receptor kinase 6A. *Mol Biol Cell* **18**:2960–2969.

Jin J, Mullen TD, Hou Q, Bielawski J, Bielawska A, Zhang X, Obeid LM, Hannun YA, and Hsu Y-T (2009) AMPK inhibitor Compound C stimulates ceramide production and promotes Bax redistribution and apoptosis in MCF7 breast carcinoma cells. *J Lipid Res* **50**:2389–2397.

Johnson LR, Scott MGH, and Pitcher JA (2004) G protein-coupled receptor kinase 5 contains a DNA-binding nuclear localization sequence. *Mol Cell Biol* **24**:10169–10179.

Kabsch W (2010) XDS. *Acta Crystallogr D Biol Crystallogr* **66**:125–132.

Kamal FA, Mickelsen DM, Wegman KM, Travers JG, Moalem J, Hammes SR, Smrcka AV, and Blaxall BC (2014) Simultaneous adrenal and cardiac g-protein-coupled receptor-gβγ inhibition halts heart failure progression. *J Am Coll Cardiol* **63**:2549–2557.

Kang Y, Zhou XE, Gao X, He Y, Liu W, Ishchenko A, Barty A, White TA, Yefanov O, Han GW, Xu Q, de Waal PW, Ke J, Tan MHE, Zhang C, Moeller A, West GM, Pascal BD, Van Eps N, Caro LN, Vishnivetskiy SA, Lee RJ, Suino-Powell KM, Gu X, Pal K, Ma J, Zhi X, Boutet S, Williams GJ, Messerschmidt M, Gati C, Zatsepin NA, Wang D, James D, Basu S, Roy-Chowdhury S, Conrad CE, Coe J, Liu H, Lisova S, Kupitz C, Grotjohann I, Fromme R, Jiang Y, Tan M, Yang H, Li J, Wang M, Zheng Z, Li D, Howe N, Zhao Y, Standfuss J, Diederichs K, Dong Y, Potter CS, Carragher B, Caffrey M, Jiang H, Chapman HN, Spence JCH, Fromme P, Weierstall U, Ernst OP, Katritch V, Gurevich VV, Griffin PR, Hubbell WL, Stevens RC, Cherezov V, Melcher K, and Xu HE (2015) Crystal structure of rhodopsin bound to arrestin by femtosecond X-ray laser. *Nature* **523**:561–567.

Kawamura S, Hisatomi O, Kayada S, Tokunaga F, and Kuo CH (1993) Recoverin has S-modulin activity in frog rods. *J Biol Chem* **268**:14579–14582.

Keegan RM, McNicholas SJ, Thomas JMH, Simpkin AJ, Simkovic F, Uski V, Ballard CC, Winn MD, Wilson KS, and Rigden DJ (2018) Recent developments in MrBUMP: better search-model preparation, graphical interaction with search models, and solution improvement and assessment. *Acta Crystallogr D Struct Biol* **74**:167–182.

Koch WJ, Rockman HA, Samama P, Hamilton RA, Bond RA, Milano CA, and Lefkowitz RJ (1995) Cardiac function in mice overexpressing the beta-adrenergic receptor kinase or a beta ARK inhibitor. *Science* **268**:1350–1353.

Kohout TA, and Lefkowitz RJ (2003) Regulation of G protein-coupled receptor kinases and arrestins during receptor desensitization. *Mol Pharmacol* **63**:9–18.

Komolov KE, and Benovic JL (2018) G protein-coupled receptor kinases: Past, present and future. *Cell Signal* **41**:17–24.

Komolov KE, Bhardwaj A, and Benovic JL (2015) Atomic Structure of GRK5 Reveals Distinct Structural Features Novel for G Protein-coupled Receptor Kinases. *J Biol Chem* **290**:20629–20647.

Komolov KE, Senin II, Kovaleva NA, Christoph MP, Churumova VA, Grigoriev II, Akhtar M, Philippov PP, and Koch K-W (2009) Mechanism of rhodopsin kinase regulation by recoverin. *J Neurochem* **110**:72–79.

Krissinel E, and Henrick K (2007) Inference of macromolecular assemblies from crystalline state. *J Mol Biol* **372**:774–797.

Kunapuli P, Onorato JJ, Hosey MM, and Benovic JL (1994) Expression, purification, and characterization of the G protein-coupled receptor kinase GRK5. *J Biol Chem* **269**:1099–1105.

Kumar V, Chichili, VPR, Tang X, and Sivaraman J (2013) A novel trans conformation of ligand-free calmodulin. *PLoS One* **8**:e54834.

Kursula P (2014) The many structural faces of calmodulin: a multitasking molecular jackknife. *Amino Acids* **46**:2295–2304.

Larabi A, Devos JM, Ng S-L, Nanao MH, Round A, Maniatis T, and Panne D (2013) Crystal structure and mechanism of activation of TANK-binding kinase 1. *Cell Rep* **3**:734–746.

Lassalas P, Gay B, Lasfargeas C, James MJ, Tran V, Vijayendran KG, Brunden KR, Kozlowski MC, Thomas CJ, Smith AB, Huryn DM, and Ballatore C (2016) Structure Property Relationships of Carboxylic Acid Isosteres. *J Med Chem* **59**:3183–3203.

Lefkowitz RJ, and Shenoy SK (2005) Transduction of receptor signals by beta-arrestins. *Science* **308**:512–517.

Levay K, Satpaev DK, Pronin AN, Benovic JL, and Slepak VZ (1998) Localization of the sites for Ca2+-binding proteins on G protein-coupled receptor kinases. *Biochem* **37**:13650–13659.

Lin S-C, and Hardie DG (2018) AMPK: Sensing Glucose as well as Cellular Energy Status. *Cell Metab* **27**:299–313.

Liu X, Chhipa RR, Nakano I, and Dasgupta B (2014) The AMPK inhibitor compound C is a potent AMPK-independent antiglioma agent. *Mol Cancer Ther* **13**:596–605.

Liu Y, and Gray NS (2006) Rational design of inhibitors that bind to inactive kinase conformations. *Nat Chem Biol* **2**:358–364.

Llona-Minguez S, and Baiget J (2013) Small-molecule inhibitors of IκB kinase (IKK) and IKK-related kinases. *Pharm Pat Analysis doi.org/10.4155/ppa.13.31*

Lodowski DT, Pitcher JA, Capel WD, Lefkowitz RJ, and Tesmer JJG (2003) Keeping G proteins at bay: a complex between G protein-coupled receptor kinase 2 and Gbetagamma. *Science* **300**:1256–1262.

Lodowski DT, Tesmer VM, Benovic JL, and Tesmer JJG (2006) The structure of G protein-coupled receptor kinase (GRK)-6 defines a second lineage of GRKs. *J Biol Chem* **281**:16785–16793.

Long F, Vagin AA, Young P, and Murshudov GN (2008) BALBES: a molecular-replacement pipeline. *Acta Crystallogr D Biol Crystallogr* **64**:125–132.

Loudon RP, and Benovic JL (1997) Altered activity of palmitoylation-deficient and isoprenylated forms of the G protein-coupled receptor kinase GRK6. *Journal of Biological Chemistry* **272**:27422–27427.

Ma X, Helgason E, Phung QT, Quan CL, Iyer RS, Lee MW, Bowman KK, Starovasnik MA, and Dueber EC (2012) Molecular basis of Tank-binding kinase 1 activation by transautophosphorylation. *Proc Natl Acad Sci* **109**:9378–9383.

Madhusudan, Akamine P, Xuong N-H, and Taylor SS (2002) Crystal structure of a transition state mimic of the catalytic subunit of cAMP-dependent protein kinase. *Nat Struct Biol* **9**:273–277.

Makino H, Saijo T, Ashida Y, Kuriki H, and Maki Y (1987) Mechanism of action of an antiallergic agent, amlexanox (AA-673), in inhibiting histamine release from mast cells. Acceleration of cAMP generation and inhibition of phosphodiesterase. *Int Arch Allergy Appl Immunol* **82**:66–71.

Manning G, Whyte DB, Martinez R, Hunter T, and Sudarsanam S (2002) The protein kinase complement of the human genome. *Science* **298**:1912–1934.

Martini JS, Raake P, Vinge LE, DeGeorge BR, DeGeorge B, Chuprun JK, Harris DM, Gao E, Eckhart AD, Pitcher JA, and Koch WJ (2008) Uncovering G protein-coupled receptor kinase-5 as a histone deacetylase kinase in the nucleus of cardiomyocytes. *Proc Natl Acad Sci* **105**:12457–12462.

McCoy AJ, Grosse-Kunstleve RW, Adams PD, Winn MD, Storoni LC, and Read RJ (2007) Phaser crystallographic software. *J Appl Crystallogr* **40**:658–674.

Métayé T, Gibelin H, Perdrisot R, and Kraimps J-L (2005) Pathophysiological roles of G-protein-coupled receptor kinases. *Cell Signal* **17**:917–928.

Moepps B, Vatter P, Frodl R, Waechter F, Dixkens C, Hameister H, and Gierschik P (1999) Alternative splicing produces transcripts encoding four variants of mouse G-protein-coupled receptor kinase 6. *Genomics* **60**:199–209.

Moriarty NW, Grosse-Kunstleve RW, and Adams PD (2009) electronic Ligand Builder and Optimization Workbench (eLBOW): a tool for ligand coordinate and restraint generation. *Acta Crystallogr D Biol Crystallogr* **65**:1074–1080.

Morin A, Eisenbraun B, Key J, Sanschagrin PC, Timony MA, Ottaviano M, and Sliz P (2013) Collaboration gets the most out of software. *Elife* **2**:e01456.

Mowers J, Uhm M, Reilly SM, Simon J, Leto D, Chiang S-H, Chang L, and Saltiel AR (2013) Inflammation produces catecholamine resistance in obesity via activation of PDE3B by the protein kinases IKK{varepsilon} and TBK1. *Elife* **2**:e01119.

Noble B, Kallal LA, Pausch MH, and Benovic JL (2003) Development of a yeast bioassay to characterize G protein-coupled receptor kinases. Identification of an NH2-terminal region essential for receptor phosphorylation. *J Biol Chem* **278**:47466–47476.

Oakhill JS, Scott JW, and Kemp BE (2009) Structure and function of AMP-activated protein kinase. *Acta Physiologica* **196**:3–14.

Obaji, E., Haikarainen, T. & Lehtiö, L. (2016). Characterization of the DNA dependent activation of human ARTD2/PARP2. *Sci Rep*, **6**(1), p.34487.

Oral EA, Reilly SM, Gomez AV, Meral R, Butz L, Ajluni N, Chenevert TL, Korytnaya E, Neidert AH, Hench R, Rus D, Horowitz JF, Poirier B, Zhao P, Lehmann K, Jain M, Yu R, Liddle C, Ahmadian M, Downes M, Evans RM, and Saltiel AR (2017) Inhibition of IKKε and TBK1 Improves Glucose Control in a Subset of Patients with Type 2 Diabetes. *Cell Metab* **26**:157–170.e7.

Palczewski K, Buczyłko J, Lebioda L, Crabb JW, and Polans AS (1993) Identification of the N-terminal region in rhodopsin kinase involved in its interaction with rhodopsin. *J Biol Chem* **268**:6004–6013.

Panjkovich A, and Svergun DI (2016) SASpy: a PyMOL plugin for manipulation and refinement of hybrid models against small angle X-ray scattering data. *Bioinformatics* **32**:2062–2064.

Pannifer AD, Flint AJ, Tonks NK, and Barford D (1998) Visualization of the cysteinyl-phosphate intermediate of a protein-tyrosine phosphatase by x-ray crystallography. *J Biol Chem* **273**:10454–10462.

Pao CS, Barker BL, and Benovic JL (2009) Role of the amino terminus of G protein-coupled receptor kinase 2 in receptor phosphorylation. *Biochem* **48**:7325–7333.

Peisley A, and Skiniotis G (2015) 2D Projection Analysis of GPCR Complexes by Negative Stain Electron Microscopy. *Methods Mol Biol* **1335**:29–38.

Penn RB, Pronin AN, and Benovic JL (2000) Regulation of G protein-coupled receptor kinases. *Trends Cardiovasc Med* **10**:81–89.

Pettersen EF, Goddard TD, Huang CC, Couch GS, Greenblatt DM, Meng EC, and Ferrin TE (2004) UCSF Chimera--a visualization system for exploratory research and analysis. *J Comp Chem* **25**:1605–1612.

Pierce KL, Premont RT, and Lefkowitz RJ (2002) Seven-transmembrane receptors. *Nat Rev Mol Cell Biol* **3**:639–650.

Pitcher JA, Fredericks ZL, Stone WC, Premont RT, Stoffel RH, Koch WJ, and Lefkowitz RJ (1996) Phosphatidylinositol 4,5-bisphosphate (PIP2)-enhanced G protein-coupled receptor kinase (GRK) activity. Location, structure, and regulation of the PIP2 binding site distinguishes the GRK subfamilies. *J Biol Chem* **271**:24907–24913.

Premont RT, and Gainetdinov RR (2007) Physiological roles of G protein-coupled receptor kinases and arrestins. *Annu Rev Physiol* **69**:511–534.

Premont RT, Macrae AD, Stoffel RH, Chung N, Pitcher JA, Ambrose C, Inglese J, MacDonald ME, and Lefkowitz RJ (1996) Characterization of the G protein-coupled receptor kinase GRK4. Identification of four splice variants. *J Biol Chem* **271**:6403–6410.

Pronin AN, and Benovic JL (1997) Regulation of the G protein-coupled receptor kinase GRK5 by protein kinase C. *J Biol Chem* **272**:3806–3812.

Pronin AN, Morris AJ, Surguchov A, and Benovic JL (2000) Synucleins are a novel class of substrates for G protein-coupled receptor kinases. *J Biol Chem* **275**:26515–26522.

Pronin AN, Satpaev DK, Slepak VZ, and Benovic JL (1997) Regulation of G protein-coupled receptor kinases by calmodulin and localization of the calmodulin binding domain. *J Biol Chem* **272**:18273–18280.

Rajsbaum R, Versteeg GA, Schmid S, Maestre AM, Belicha-Villanueva A, Martínez-Romero C, Patel JR, Morrison J, Pisanelli G, Miorin L, Laurent-Rolle M, Moulton HM, Stein DA, Fernandez-Sesma A, Tenoever BR, and García-Sastre A (2014) Unanchored K48-linked polyubiquitin synthesized by the E3-ubiquitin ligase TRIM6 stimulates the interferon-IKKε kinase-mediated antiviral response. *Immunity* **40**:880–895.

Reilly SM, Ahmadian M, Zamarron BF, Chang L, Uhm M, Poirier B, Peng X, Krause DM, Korytnaya E, Neidert A, Liddle C, Yu RT, Lumeng CN, Oral EA, Downes M, Evans RM, and Saltiel AR (2015) A subcutaneous adipose tissue-liver signalling axis controls hepatic gluconeogenesis. *Nat Commun* **6**:6047.

Reilly SM, and Saltiel AR (2017) Adapting to obesity with adipose tissue inflammation. *Nat Rev Endo* **13**:633–643.

Reilly SM, Chiang S-H, Decker SJ, Chang L, Uhm M, Larsen MJ, Rubin JR, Mowers J, White NM, Hochberg I, Downes M, Yu RT, Liddle C, Evans RM, Oh D, Li P, Olefsky JM, and Saltiel AR (2013) An inhibitor of the protein kinases TBK1 and IKK-ε improves obesity-related metabolic dysfunctions in mice. *Nat Med* **19**:313–321.

Reiter E, and Lefkowitz RJ (2006) GRKs and β-arrestins: roles in receptor silencing, trafficking and signaling. *Trends in Endo Met* **17**:159–165.

Rockman HA, Chien KR, Choi DJ, Iaccarino G, Hunter JJ, Ross J, Lefkowitz RJ, and Koch WJ (1998) Expression of a beta-adrenergic receptor kinase 1 inhibitor prevents the development of myocardial failure in gene-targeted mice. *Proc Nat Acad Sci* **95**:7000–7005.

Rockman HA, Koch WJ, and Lefkowitz RJ (2002) Seven-transmembrane-spanning receptors and heart function. *Nature* **415**:206–212.

Roskoski R (2015) A historical overview of protein kinases and their targeted small molecule inhibitors. *Pharmacol Res* **100**:1–23.

Roskoski R (2016) Classification of small molecule protein kinase inhibitors based upon the structures of their drug-enzyme complexes. *Pharmacol Res* **103**:26–48.

Sakaguchi K, Green M, Stock N, Reger TS, Zunic J, and King C (2004) Glucuronidation of carboxylic acid containing compounds by UDP-glucuronosyltransferase isoforms. *Archives of Biochem and Biophys* **424**:219–225.

Salazar NC, Chen J, and Rockman HA (2007) Cardiac GPCRs: GPCR signaling in healthy and failing hearts. *Biochim Biophys Acta* **1768**:1006–1018.

Sallese M, Mariggiò S, Collodel G, Moretti E, Piomboni P, Baccetti B, and De Blasi A (1997) G protein-coupled receptor kinase GRK4. Molecular analysis of the four isoforms and ultrastructural localization in spermatozoa and germinal cells. *Journal of Biological Chemistry* **272**:10188–10195.

Saltiel AR (2012) Insulin resistance in the defense against obesity. *Cell Metab* **15**:798–804.

Saltiel AR (2016) New therapeutic approaches for the treatment of obesity. *Sci Transl Med* **8**:323rv2.

Santos R, Ursu O, Gaulton A, Bento AP, Donadi RS, Bologa CG, Karlsson A, Al-Lazikani B, Hersey A, Oprea TI, and Overington JP (2017) A comprehensive map of molecular drug targets. *Nat Rev Drug Disc* **16**:19–34.

Saraste M, Sibbald PR, and Wittinghofer A (1990) The P-loop – a common motif in ATP- and GTP-binding proteins. *Trends Biochem Sci* **15**:430–434.

Sato PY, Chuprun JK, Schwartz M, and Koch WJ (2015) The evolving impact of g protein-coupled receptor kinases in cardiac health and disease. *Physiol Rev* **95**:377–404.

Schumacher SM, Gao E, Zhu W, Chen X, Chuprun JK, Feldman AM, Tesmer JJG, and Koch WJ (2015) Paroxetine-mediated GRK2 inhibition reverses cardiac dysfunction and remodeling after myocardial infarction. *Sci Transl Med* **7**:277ra31–277.

Shimada T, Kawai T, Takeda K, Matsumoto M, Inoue J, Tatsumi Y, Kanamaru A, and Akira S (1999) IKK-i, a novel lipopolysaccharide-inducible kinase that is related to IkappaB kinases. *Int Immunol* **11**:1357–1362.

Shrestha A, Hamilton G, O'Neill E, Knapp S, and Elkins JM (2012) Analysis of conditions affecting auto-phosphorylation of human kinases during expression in bacteria. *Protein Expr Purif* **81**:136–143.

Shu C, Sankaran B, Chaton CT, Herr AB, Mishra A, Peng J, and Li P (2013) Structural insights into the functions of TBK1 in innate antimicrobial immunity. *Structure* **21**:1137–1148.

Stoffel RH, Inglese J, Macrae AD, Lefkowitz RJ, and Premont RT (1998) Palmitoylation increases the kinase activity of the G protein-coupled receptor kinase, GRK6. *Biochem* **37**:16053–16059.

Stoffel RH, Randall RR, Premont RT, Lefkowitz RJ, and Inglese J (1994) Palmitoylation of G protein-coupled receptor kinase, GRK6. Lipid modification diversity in the GRK family. *J Biol Chem* **269**:27791–27794.

Strulovich R, Tobelaim WS, Attali B, and Hirsch JA (2016) Structural Insights into the M-Channel Proximal C-Terminus/Calmodulin Complex. *Biochem* **55**:5353–5365.

Stuckey JA, Schubert HL, Fauman EB, Zhang ZY, Dixon JE, and Saper MA (1994) Crystal structure of Yersinia protein tyrosine phosphatase at 2.5 A and the complex with tungstate. *Nature* **370**:571–575.

Sun F, Ding Y, Ji Q, Liang Z, Deng X, Wong CCL, Yi C, Zhang L, Xie S, Alvarez S, Hicks LM, Luo C, Jiang H, Lan L, He C (2012) Protein cysteine phosphorylation of SarA/MgrA family transcriptional regulators mediates bacterial virulence and antibiotic resistance. *Proc Nat Acad of Sci* **109**:15461-15466.

Sun Jingchun, Wei Q, Zhou Y, Wang J, Liu Q, and Xu H (2017) A systematic analysis of FDA-approved anticancer drugs. *BMC Syst Biol* **11**:87.

Sun Jiyuan, and Lin X (2008) Beta-arrestin 2 is required for lysophosphatidic acid-induced NF-kappaB activation. *Proc Natl Acad Sci USA* **105**:17085–17090.

Svergun D, Barberato C, Koch MH (1995) CRYSOL–a program to evaluate X-ray solution scattering of biological macromolecules from atomic coordinates (1995). *J Appl Cryst* **28**:768-773.

Svergun DI (1999) Restoring low resolution structure of biological macromolecules from solution scattering using simulated annealing. *Biophys J* **76**:2879–2886.

Svergun DI (1992) Determination of the regularization parameter in indirect-transform methods using perceptual criteria. *J Appl Crystallogr* **25**:495–503.

Svergun DI, Petoukhov MV, and Koch MH (2001) Determination of domain structure of proteins from X-ray solution scattering. *Biophys J* **80**:2946–2953.

Swanson RV, Alex LA, and Simon MI (1994) Histidine and aspartate phosphorylation: two-component systems and the limits of homology. *Trends Biochem Sci* **19**:485–490.

Swinburn BA, Sacks G, Hall KD, McPherson K, Finegood DT, Moodie ML, and Gortmaker SL (2011) The global obesity pandemic: shaped by global drivers and local environments. *Lancet* **378**:804–814.

Tang G, Peng L, Baldwin PR, Mann DS, Jiang W, Rees I, and Ludtke SJ (2007) EMAN2: an extensible image processing suite for electron microscopy. *J Struct Biol* **157**:38–46.

Taylor SS, and Kornev AP (2011) Protein kinases: evolution of dynamic regulatory proteins. *Trends Biochem Sci* **36**:65–77.

Tenoever BR, Ng S-L, Chua MA, McWhirter SM, García-Sastre A, and Maniatis T (2007) Multiple functions of the IKK-related kinase IKKepsilon in interferon-mediated antiviral immunity. *Science* **315**:1274–1278.

Tesmer JJG (2016) Hitchhiking on the heptahelical highway: structure and function of 7TM receptor complexes. *Nat Rev Mol Cell Biol* **17**:439–450.

Tesmer JJG, Tesmer VM, Lodowski DT, Steinhagen H, and Huber J (2010) Structure of Human G Protein-Coupled Receptor Kinase 2 in Complex with the Kinase Inhibitor Balanol. *J Med Chem* **53**:1867–1870.

Tesmer VM, Kawano T, Shankaranarayanan A, Kozasa T, and Tesmer JJG (2005) Snapshot of activated G proteins at the membrane: the G-GRK2-Gbetagamma complex. *Science* **310**:1686–1690.

Thal DM, Homan KT, Chen J, Wu EK, Hinkle PM, Huang ZM, Chuprun JK, Song J, Gao E, Cheung JY, Sklar LA, Koch WJ, and Tesmer JJG (2012) Paroxetine Is a Direct Inhibitor of G Protein-Coupled Receptor Kinase 2 and Increases Myocardial Contractility. *ACS Chem Biol* **7**:1830–1839.

Thal DM, Yeow RY, Schoenau C, Huber J, and Tesmer JJG (2011) Molecular mechanism of selectivity among G protein-coupled receptor kinase 2 inhibitors. *Mol Pharmacol* **80**:294–303.

Thiyagarajan MM, Stracquatanio RP, Pronin AN, Evanko DS, Benovic JL, and Wedegaertner PB (2004) A predicted amphipathic helix mediates plasma membrane localization of GRK5. *J Biol Chem* **279**:17989–17995.

Tidow H, and Nissen P (2013) Structural diversity of calmodulin binding to its target sites. *FEBS J* **280**:5551–5565.

Torisawa A, Arinobu D, Tachibanaki S, and Kawamura S (2008) Amino acid residues in GRK1/GRK7 responsible for interaction with S-modulin/recoverin. *Photochem Photobiol* **84**:823–830.

Treiber DK, and Shah NP (2013) Ins and outs of kinase DFG motifs. *Chemistry & Biology* **20**:745–746.

Trott O, and Olson AJ (2010) AutoDock Vina: improving the speed and accuracy of docking with a new scoring function, efficient optimization and multithreading. *J Comp Chem* **31**:455-461

Tsvetanova NG, Irannejad R, and von Zastrow M (2015) G protein-coupled receptor (GPCR) signaling via heterotrimeric G proteins from endosomes. *J Biol Chem* **290**:6689–6696.

Tu D, Zhu Z, Zhou AY, Yun C-H, Lee K-E, Toms AV, Li Y, Dunn GP, Chan E, Thai T, Yang S, Ficarro SB, Marto JA, Jeon H, Hahn WC, Barbie DA, and Eck MJ (2013) Structure and ubiquitination-dependent activation of TANK-binding kinase 1. *Cell Rep* **3**:747–758.

Vagin A, Teplyakov A, IUCr (1997) MOLREP: an Automated Program for Molecular Replacement. *J Appl Crystallogr* **30**:1022–1025.

Vandonselaar M, Hickie RA, Quail W, and Delbaere LTJ (1994) Trifluoperazine-induced conformational change in Ca2+-calmodulin. *Nat Struct Mol Biol* **1**:795–801.

Vatter P, Stresser C, Samle I, Gierschik P, and Moepps B (2005) The variable C-terminal extension of G-protein-coupled receptor kinase 6 constitutes an accessorial auto regulatory domain. *FEBS J* **272**:6039-6051.

Vitaku E, Smith DT, and Njardarson JT (2014) Analysis of the structural diversity, substitution patterns, and frequency of nitrogen heterocycles among U.S. FDA approved pharmaceuticals. *J Med Chem* **57**:10257–10274.

Volkov VV, Svergun DI (2003) Uniqueness of *ab initio* shape determination in small-angle scattering. *J Appl Cryst* **36**:860-864

Waldschmidt HV, Homan KT, Cato MC, Cruz-Rodríguez O, Cannavo A, Wilson MW, Song J, Cheung JY, Koch WJ, Tesmer JJG, and Larsen SD (2017) Structure-Based Design of Highly Selective and Potent G Protein-Coupled Receptor Kinase 2 Inhibitors Based on Paroxetine. *J Med Chem* **60**:3052–3069.

Waldschmidt HV, Homan KT, Cruz-Rodríguez O, Cato MC, Waninger-Saroni J, Larimore KM, Cannavo A, Song J, Cheung JY, Kirchhoff PD, Koch WJ, Tesmer JJG, and Larsen SD (2016) Structure-Based Design, Synthesis, and Biological Evaluation of Highly Selective and Potent G Protein-Coupled Receptor Kinase 2 Inhibitors. *J Med Chem* **59**:3793–3807.

Walker JE, Saraste M, Brunswick MJ, Gay NJ (1982) Distantly related sequences in the alpha- and beta-subunits of ATP synthase, myosin, kinases and other ATP-requiring enzymes and a common nucleotide binding fold. *EMBO J* **1**:945-951.

Wang T, Block MA, Cowen S, Davies AM, Devereaux E, Gingipalli L, Johannes J, Larsen NA, Su Q, Tucker JA, Whitston D, Wu J, Zhang H-J, Zinda M, and Chuaqui C (2012) Discovery of azabenzimidazole derivatives as potent, selective inhibitors of TBK1/IKKε kinases. *Bioorg Med Chem Lett* **22**:2063–2069.

West AH, and Stock AM (2001) Histidine kinases and response regulator proteins in two-component signaling systems. *Trends Biochem Sci* **26**:369–376.

Winn MD, Ballard CC, Cowtan KD, Dodson EJ, Emsley P, Evans PR, Keegan RM, Krissinel EB, Leslie AGW, McCoy A, McNicholas SJ, Murshudov GN, Pannu NS, Potterton EA, Powell HR, Read RJ, Vagin A, and Wilson KS (2011) Overview of the CCP4 suite and current developments. *Acta Crystallogr D Biol Crystallogr* **67**:235–242.

Winter G, Waterman DG, Parkhurst JM, Brewster AS, Gildea RJ, Gerstel M, Fuentes-Montero L, Vollmar M, Michels-Clark T, Young ID, Sauter NK, and Evans G (2018) DIALS: implementation and evaluation of a new integration package. *Acta Crystallogr D Struct Biol* **74**:85–97.

Wu P, Nielsen TE, and Clausen MH (2015) FDA-approved small-molecule kinase inhibitors. *Trends Pharmacol Sci* **36**:422–439.

Yamauchi E, Nakatsu T, Matsubara M, Kato H, and Taniguchi H (2003) Crystal structure of a MARCKS peptide containing the calmodulin-binding domain in complex with Ca^{2+}-calmodulin. *Nat Struct Biol* **10**:226–231.

Yang P, Glukhova A, Tesmer JJG, and Chen Z (2013) Membrane Orientation and Binding Determinants of G Protein-Coupled Receptor Kinase 5 as Assessed by Combined Vibrational Spectroscopic Studies. *PLoS ONE* **8**:e82072–11.

Yang Z, Fang J, Chittuluru J, Asturias FJ, and Penczek PA (2012) Iterative stable alignment and clustering of 2D transmission electron microscope images. *Structure* **20**:237–247.

Yao X-Q, Cato MC, Labudde E, Beyett TS, Tesmer JJG, and Grant BJ (2017) Navigating the conformational landscape of G protein-coupled receptor kinases during allosteric activation. *J Biol Chem* **292**:16032–16043.

Yong H-Y, Koh M-S, and Moon A (2009) The p38 MAPK inhibitors for the treatment of inflammatory diseases and cancer. *Expert Opin Investig Drugs* **18**:1893–1905.

Zeqiraj E, and van Aalten DM (2010) Pseudokinases: remnants of evolution or key allosteric regulators? *Curr. Opin. Struct. Biol.* **20**:772–781.

Zhang BB, Zhou G, and Li C (2009) AMPK: an emerging drug target for diabetes and the metabolic syndrome. *Cell Metab* **9**:407–416.

Zhang J, Adrián FJ, Jahnke W, Cowan-Jacob SW, Li AG, Iacob RE, Sim T, Powers J, Dierks C, Sun F, Guo G-R, Ding Q, Okram B, Choi Y, Wojciechowski A, Deng X, Liu G, Fendrich G, Strauss A, Vajpai N, Grzesiek S, Tuntland T, Liu Y, Bursulaya B, Azam M, Manley PW, Engen JR, Daley GQ, Warmuth M, and Gray NS (2010) Targeting Bcr-Abl by combining allosteric with ATP-binding-site inhibitors. *Nature* **463**:501–506.

Zhang J, Yang PL, and Gray NS (2009) Targeting cancer with small molecule kinase inhibitors. *Nat Rev Cancer* **9**:28–39.

Zhang Y, Matkovich SJ, Duan X, and Gold JI (2011) Nuclear Effects of G-Protein Receptor Kinase 5 on Histone Deacetylase 5–Regulated Gene Transcription in Heart Failure. *Circ Heart Fail* **4**:659–668.

Zhao P, Wong KI, Sun X, Reilly SM, Uhm M, Liao Z, Skorobogatko Y, and Saltiel AR (2018) TBK1 at the Crossroads of Inflammation and Energy Homeostasis in Adipose Tissue. *Cell* **172**:731–743.e12.

Zhou AY, Shen RR, Kim E, Lock YJ, Xu M, Chen ZJ, and Hahn WC (2013) IKKε-mediated tumorigenesis requires K63-linked polyubiquitination by a cIAP1/cIAP2/TRAF2 E3 ubiquitin ligase complex. *Cell Rep* **3**:724–733.